T2R2 東京科学大学 リサーチリポジトリ
Science Tokyo Research Repository

論文 / 著書情報
Article / Book Information

題目(和文)	DNSによる水素混焼メタン空気旋回乱流予混合火炎に関する研究
Title(English)	A DNS study of hydrogen-enriched methane/air turbulent swirling premixed flames
著者(和文)	朴埈輝
Author(English)	Joonhwi Park
出典(和文)	学位:博士(工学), 学位授与機関:東京工業大学, 報告番号:甲第11501号, 授与年月日:2020年3月26日, 学位の種別:課程博士, 審査員:店橋 護,末包 哲也,野﨑 智洋,長﨑 孝夫,志村 祐康
Citation(English)	Degree:Doctor (Engineering), Conferring organization: Tokyo Institute of Technology, Report number:甲第11501号, Conferred date:2020/3/26, Degree Type:Course doctor, Examiner:,,,,
学位種別(和文)	博士論文
Type(English)	Doctoral Thesis

Powered by T2R2 (Science Tokyo Research Repository)

令和元年度　学位論文

DNSによる水素混焼メタン空気旋回乱流予混合火炎に関する研究

指導教員　店橋 護　　教　授
志村 祐康　准教授

東京工業大学　工学院
機械系
エネルギーコース
16D18144　Park JoonHwi

Doctoral Dissertation

A DNS Study of Hydrogen-Enriched Methane/Air Turbulent Swirling Premixed Flames

Supervisors

Professor : Mamoru Tanahashi

Associate Professor : Masayasu Shimura

Department of Mechanical Engineering
Tokyo Institute of Technology

16D18144

Joonhwi Park

Contents

1 Introduction **3**

1.1 Combustion technology and environmental issues 3

1.2 Numerical study of combustion 5

1.3 Objectives of this study 8

1.4 Outline of this thesis 10

2 Direct numerical simulation of hydrogen–enriched methane/air turbulent swirling premixed flames **13**

2.1 Preface 13

2.2 Governing equations 15

2.2.1 Governing equations of reactive flows 15

2.2.2 Chemical reaction 19

2.2.3 Thermodynamic properties 22

2.2.4 Transport coefficients 24

2.3 Computational methods 24

2.3.1 Spatial discretization 24

2.3.2 Spatial filter 25

2.3.3 Boundary conditions 26

2.3.4 Time integration 31

2.3.5 Swirling velocity profiles 33

2.3.6 Computational conditions 36

2.4 Effects of mixture conditions on combustion characteristics 38

2.5 Turbulent combustion conditions 39
2.6 Conclusions of this chapter 42

3 Effects of hydrogen-enrichment on global flame features 49
3.1 Preface 49
3.2 Effects of hydrogen ratios on the global flame features 51
3.3 Effects of hydrogen ratios and local tangential strain rate on the reaction zone characteristics 55
3.4 Effects of hydrogen ratios on balance between convection, diffusion and chemical reaction 58
3.5 Conclusions of this chapter 61

4 Local flame structures and extinction mechanism 76
4.1 Preface 76
4.2 Statistical characteristics of local flame structures 77
4.3 Contributions of elemental reactions 79
4.3.1 Distributions of elemental reaction rates 79
4.3.2 Effects of tangential strain rate on elemental reaction rates 81
4.4 Investigation of extinction mechanism 82
4.4.1 Extinction strain rate in laminar flames 82
4.4.2 Extinction mechanism in shear layers 83
4.5 Effects of turbulent motions on the chemical time scales 85
4.6 Conclusions of this chapter 87

5 Conclusions 110

References 113

A Chemical mechanism 126

Acknowledgements 133

Chapter 1

Introduction

1.1 Combustion technology and environmental issues

Our lives strongly depend on thermal energy produced by combustion of fossil fuels, oil, natural gas and coal. Figure 1.1 shows consumption trends of primary energy sources form the year of 2010 and prediction in the future [1]. In 2019, the energy consumption by primary energy sources accounts for 80% of total energy consumption, which indicates that large portion of thermal energy is produced by combustion of fossil fuels. In 2050, it is predicted that energy consumption by fossil fuels would account for 68% of total energy consumption. Since the total energy consumption is expected to increase steadily, consumption of fossil fuels would increase further, though consumption by renewable energy source is expected to increase significantly up to 28% of total energy consumption. Thermal energy produced by combustion of fossil fuels are used in vehicles, aircraft, watercraft, power generation and so on. Figure 1.2 shows consumption of fuels for electric power sector. In recent years, most of electricity is generated by combustion of coal and natural gas [1]. In 2050, although it is expected that generation by renewable sources would increase significantly, it is still predicted that approximately 40% of electricity would be generated by combustion of fossil fuels. Figure 1.3 shows energy consumption by sources for transport sector [1]. As

the figure clearly shows, most of energy consumption is occupied by combustion of fossil fuels in the transport sector. However, emissions of CO_2, which is one of the green house effects gases, increases with the increased amount of fossil fuels consumption, because CO_2 is discharged through the combustion of fossil fuels. Since environmental pollutants, such as NO_x and SO_x are also discharged in the combustion processes, regulations for emissions of such pollutants are predicted to be stricter in the future.

From the reasons above, the demands for combustion devices to be more efficient and environmentally friendly have been increasing in recent years. Internal combustion engines are widely used for vehicles, aircraft, watercraft and gas turbine for electricity generation and considered to be one of the combustion devices result in increased emissions of pollutants. Combustion technologies for high efficiency and low emissions have been developed based on the characteristics of flow filed, fuel types and structures of the devices. For the realizations of higher thermal efficiency, reduction in thermal loss by cooling and reduced emissions of NO_x in gasoline engines, studies of turbulent combustion have been conducted under higher compression ratios, ultra lean and high exhausted gas recirculation (EGR) ratio conditions [2, 3]. Recently, combustion technologies, such as homogeneous charge compression ignition (HCCI), have been developed and widely studied for implementation for practical devices [4, 5]. For gas turbine engines, increased turbine inlet temperature and lean premixed combustion have been implemented for for higher thermal efficiency and reduction of NO_x emissions. Recently, implementation of EGR is attempted to gas turbine engines for further reduction of NO_x emissions [6]. In addition to the recent combustion technologies, utilization of alternative fuels such as hydrogen and hydrogen-enriched natural gas has been attempted for reduced emission of combustion devices. Hydrogen has attracted our attentions as one of the alternative fuels, because CO_2 is not discharged during its combustion processes. In recent years, hydrogen enriched [7, 8] and pure hydrogen [9] gas turbine combustor are studied for development of gas turbine engines using hydrogen as a fuel.

Therefore, development of efficient and environmental friendly combustion devices is expected to be realized with the recent combustion technologies and alternative fuels addressed above. However, there are still technical difficulties to be overcome, such as lower burning velocities and difficulties in ignition during the combustion process under high pressure, ultra lean and high EGR ratio. For gas turbine engines, implementation of lean premixed combustion may cause combustion oscillation and limit phenomena such as blow out and extinction. Moreover, using hydrogen as a fuel for gas turbine engines has a high risk of flash back for lean premixed combustion. Because of its high burning velocity and extremely high burnt gas temperature of hydrogen combustion, thermal durability of mechanical components and materials are concerned. Thus, it is anticipated that using hydrogen as a fuel for lean combustion mode would face more technical difficulties. Therefore, it can be said that the main object of studies for combustion is resolving technical difficulties and developing of combustion devices which are highly efficient and environmental friendly.

1.2 Numerical study of combustion

Understanding physical and chemical phenomena in the combustor is essential for designing of high efficiency and environmental friendly combustor. To understand the combustion phenomena accurately, thermochemical conditions, such as pressure, temperature and species concentration in the flame are required. Due to the existence of interactions between flow and flame, information of velocity field is also required for practical combustion devices. Since distributions of the variables vary in time and space, information of spatial and temporal distributions and fluctuations are also required. To acquire insights into the combustion phenomena, asymptotic analysis, experimental measurement and numerical simulations can be applied. In the asymptotic analysis, temporal and spatial distributions, or analytical solutions are obtained by solving the governing equations which describe temporal and spatial changes of physical quantities. However, as the governing equations of

reactive flows are expressed as a systems of complicated partial differential equations, it is impossible to obtain analytical solutions in general, except for simplified combustion problems. In the experimental measurements, physical quantities of interest in the combustion field can be obtained by applying various measurement techniques. Velocity measurement by hot wired and temperature measurement by thermocouple are considered as examples of experiment measurements. However, a possibility that the flow field may be affected by the measurement instrument itself is the drawback of experimental measurements. In recent year, owing to remarkable development of laser diagnostic technologies, various physical quantities can be measured without affecting the flows field. For example, velocity field can be measured by using particle image velocimetry (PIV) [10–12] and distributions of species (CH, OH, CH_2O) and heat release rates can be obtained by using planar laser-induced fluorescence (PLIF) measurement [13–15]. However, there are still difficulties in three dimensional measurements with high accuracy and configurations of combustion fields in which the laser diagnostics can be applied are limited to relatively simplified ones. From the reasons above, the insights into combustion phenomena can be obtained by asymptotic analysis and experimental measurements are limited.

On the other hand, by implementing numerical simulation techniques, temporal and spatial distributions of various physical quantities, or numerical solutions are obtained by solving the governing equations of combustion field. Owing to remarkable computational technologies in recent years, numerical simulations can be applied to not only fundamental combustion studies but also designing of practical combustion devices. Numerical simulation approaches are categorized into Reynolds averaged Navier-Stokes simulation (RANS), large eddy simulation (LES) and direct numerical simulation (DNS) and explained as follows.

Reynolds averages Navier-Stokes simulation (RANS) is a method of simulation which obtains numerical solutions from Reynolds or Favre averaged governing equations. All of the terms for fluctuating quantities in the governing equations are modeled. RANS is widely used for designing of practical combustion devices,

because of its short computational time and the least memory requirement among the numerical approaches. However, it is difficult to understand the phenomena of turbulent combustion accompanying extremely strong unsteadiness only by the ensemble averaged numerical solutions obtained by RANS.

Large eddy simulation (LES) is a numerical approach which obtains numerical solutions by solving spatially filtered governing equations. In LES, phenomena of which length scales are of the grid size (grid scale:GS) are solved analytically, while the phenomena affecting the phenomena within GS, occur with scales smaller than the grid size (subgrid scale:SGS) are modeled. Although its computational cost is more expensive than that of RANS, it is applicable for predicting unsteady phenomena. Thanks to development of computational technologies, LES of combustion is utilized for development and designing of practical combustion devices. Implementation of RANS and LES to the combustion field enables obtaining three dimensional distributions of physical quantities, however, the accuracy of results obtained by these approaches are strongly dependent on the accuracy of models employed in the simulations.

Direct numerical simulation (DNS) is the first principle approach which solves the governing equations by using high accuracy discretization schemes without modeling any term in the governing equations. It requires huge numerical resources, because the grid size and time stepping should be set small enough to resolve the smallest scales of turbulence and chemical reactions. Thus, combustion problems in which DNS can be applied are limited to relatively simpler configurations compared to RANS and LES. However, as flow field and distributions of temperature and species in the combustion field can be obtained with high accuracy by DNS, it can be utilized for investigation of various combustion phenomena and development of RANS and LES models. In addition, owing to development of computational technologies and efficient numerical methods [16–19], the applicable range of DNS has been extended significantly. Recently, three dimensional DNS with detailed or reduced chemical mechanism have been conducted for various turbulent combustion problems [20–25]. Therefore, DNS of combustion is

expected to enable us to obtain insights into complicated unsteady phenomena in realistic turbulent combustion fields.

1.3 Objectives of this study

Using hydrogen as a fuel is one of the promising ways to achieve more efficient and environmentally friendly combustion devices, because hydrogen has great energy density than natural gas and does not discharge CO_2 during its combustion processes. However, there are still difficulties due to the characteristics of H_2 combustion, such as extremely high burnt gas temperature, higher burning velocity than hydrocarbon fuels [26]. Furthermore, the risk of flash back in upstream of combustor increases significantly when lean premixed combustion of pure hydrogen is considered.

As an alternative method, addition of H_2 to natural gas (mainly consists of CH_4) has brought to our attention recently. Advantages of using such a fuel in lean premixed combustion are improved flame stability with reduced emissions of pollutants, such as CO [27], NO [28] and NO_x [29], lower lean blowout limit [30–32], extended flashback limit [33–35] and resistance to strain rate induced extinction [27, 36, 37]. Therefore, combustion of H_2 added natural gas is considered to be one of the promising ways to achieve both higher thermal efficiency and reduced emissions of pollutants [38].

Gas turbine engines are considered as one of the devices where utilization of H_2-enriched natural gas is effective [39, 40]. In such devices, turbulent swirling flows are widely used for enhancement of turbulent mixing and flame stabilization. Swirling flows are characterize by the inner and outer recirculation zones and flame stabilization by conveying burnt gases to fresh reactants. Furthermore, relatively strong three-dimensionality and extremely high strain rates of the flow field affect the flame structures and dynamics substantially. The high strain rates decrease heat release rates and may cause local extinction [21]. Therefore, it is important to clarify the characteristics of CH_4/H_2/air turbulent swirling flames for the realization

of practical H_2-enriched gas turbines engines.

For fundamental insight into CH_4/H_2 combustion, Wang et al. [41] have reported changes in the role of H_2 in one-dimensional CH_4/H_2/air laminar premixed flames under various mixture conditions. According to the results, the role of H_2 in the flames shifts from an intermediate species to a reactant species when the volume ratio of H_2 in the premixed mixture is increased from 20% to 30%. The reactions in C_1 chemical pathway are promoted due to relatively higher concentrations of H, O and OH radical pools with the increased amount of H_2. Similar conclusions to Wang et al. are obtained under the conditions of higher preheat temperature of 700 K and 0.1 MPa as shown in Fig. 1.4. Day et al. [42] have conducted 2-dimensional simulations of lean CH_4/H_2/air turbulent premixed flames, which are categorized into the laminar flamelet regime. Similarly, the role of H_2 changes when the volume ratio of H_2 in the mixture is higher than 25%. These results indicate reaction pathway alternation with the increase of H_2 volume ratios in the mixture in both laminar and relatively low level turbulent flames. However, the effects of mixture conditions on the combustion characteristics and structures of CH_4/H_2/air premixed flames which are affected by strong three dimensionality of the flows and associated intense turbulent mixing, such as that in the turbulent swirling flows have not been clarified yet.

There are experimental studies of H_2/CH_4 swirling flames mainly focusing on the flame shapes and emission characteristics under various conditions, such as H_2 volume fractions and pressure [43], fuel composition and swirl strength [44, 45]. Flame-shape transition [34, 37, 46] and blow-off events [7, 30, 47] are also studied experimentally under various mixture conditions. Large eddy simulation (LES) studies also have provided findings of flame structure and flow-flame interactions in weakly or moderately turbulent premixed swirling flames of CH_4/air [48, 49], CH_4/H_2/air [50] and $CH_4/O_2/CO_2$ [51]. However, effects of mixture conditions on reaction zone structures and species transport characteristics in the turbulent swirling flames affected by intense turbulence, which are necessary for turbulent combustion modeling and designing H_2-enriched gas turbine engines, have not

been fully understood yet.

Therefore, in this study, DNS of CH_4/H_2/air turbulent swirling premixed flames in a cuboid combustor have been performed to clarify the effects of H_2 enrichment on the flame structures in a swirl flow configuration by using a reduced chemistry consisting of 25 reactive species and 111 elemental reactions and considering temperature dependency of transport and thermal properties.

1.4 Outline of this thesis

In chapter 2, numerical methods and conditions for DNS of hydrogen-enriched CH_4/air turbulent swirling premixed flames in a cuboid combustor are addressed. Combustion characteristics between the cases are investigated by comparing total heat release rate in the combustor and distributions of reaction progress variable defined by species mass fraction. Turbulent combustion conditions of the present DNS are investigated based on Peters' regime diagram [52].

In chapter 3, effects of hydrogen ratios on global flame features are investigated. First, the global flame features, distributions of temperature, heat release rate, species mass fraction and reaction rate are shown. Next, comparison of DNS results with unstrained and strained laminar flames are shown to clarify the reaction zone characteristics of turbulent swirling premixed flames. Lastly, balance between convection, diffusion and chemical reaction terms of an instantaneous species conservation equation is considered.

In chapter 4, effects of turbulent motions on the local flame structure and extinction mechanism in the shear layers are investigated. Statistical characteristics of local flames structure and dominant elemental reaction rates of the fuels are shown. Extinction and flame stabilization mechanism in the shear layers are considered in the aspects of thermochemical conditions and flow strain rates of the flow field. Finally, effects of turbulent motions on the characteristic time scales of reactive species are investigated.

In chapter 5, the main conclusions of each chapter are summarized.

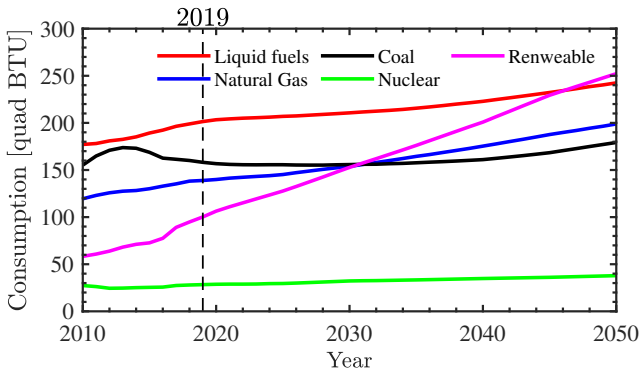


Figure 1.1: World total energy consumption by sources [1].

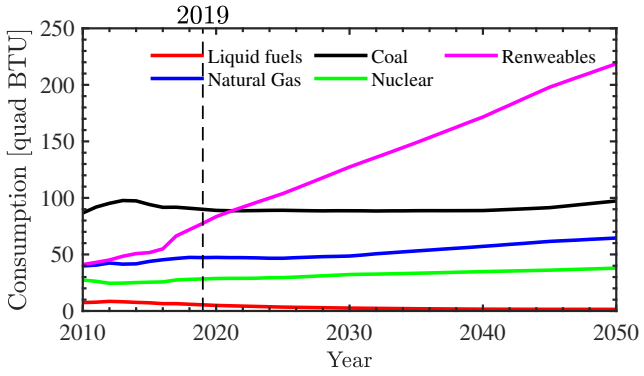


Figure 1.2: World total energy consumption by sources for electric power sector [1].

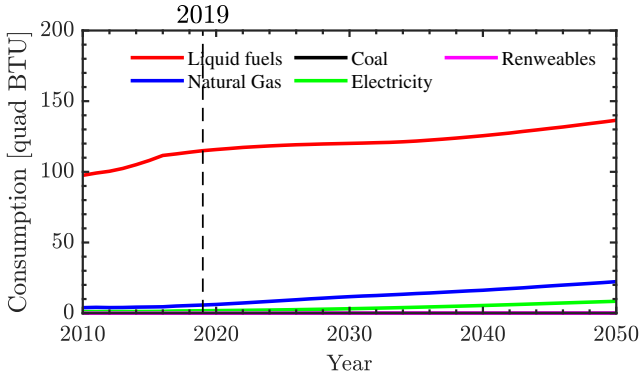


Figure 1.3: World total energy consumption by sources for transportation sector [1].

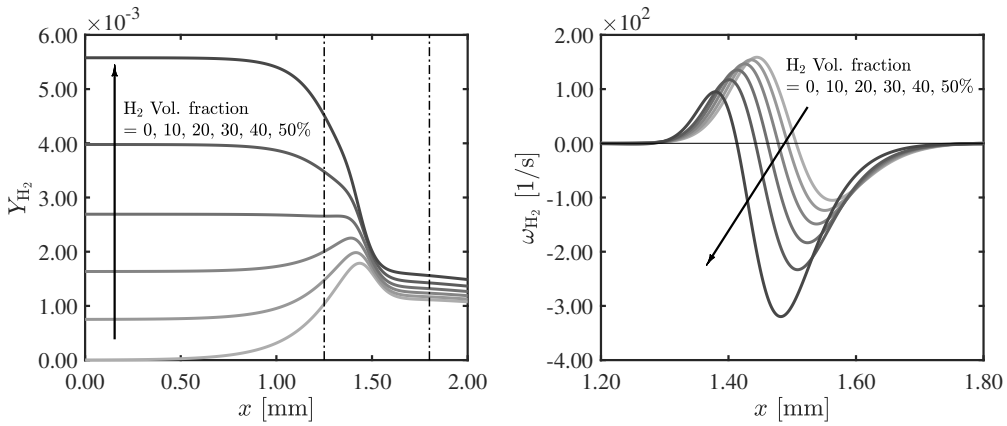


Figure 1.4: Variations H_2 mass fraction Y_{H_2} (left) and reaction rate ω_{H_2} (right) with increase of H_2 volume fractions in one dimensional laminar premixed flame (ϕ = 1.0, T_{ini} = 700 K and p = 0.1 MPa).

Chapter 2

Direct numerical simulation of hydrogen–enriched methane/air turbulent swirling premixed flames

2.1 Preface

Although DNS of turbulent combustion requires huge computational resources, information of flow field and chemical reactions can be acquired highly accurately. Thanks to remarkable development of computational technologies and numerical methods, the scopes of DNS studies for turbulent combustion where complex elemental reactions and multi-dimensional phenomena occur are extended significantly. Turbulent combustion studies by conducting three dimension DNS with detailed or reduced chemistry are carried out for various fuels, not only hydrogen [20, 21] but also hydrocarbon fuels, such as methane [53, 54], propane [55], *n*-heptane [56] and *n*-dodecane[57] and so on. The focus of these studies is investigating how combustion characteristics are affected by interactions between turbulence and chemical reactions in the reaction zones of the flame. From the reason above, DNS studies of turbulent combustion are mainly conducted for freely propagating flames in homogeneous isotropic turbulence. [20, 21, 53–57].

As for practical combustion devices, however, combustion characteristics may be different from those of turbulent flames in homogeneous isotropic turbulence

due to the existence of mean shear flow and three dimensionality of the flows. The effects of those features on the flame have been studied for turbulent premixed V-flames [22], turbulent jet flames [23, 58] and constant volume vessels [25] and turbulent swirling flames [24, 59–61].

In the turbulent swirling premixed flames, which are widely used for gas turbine combustor, the combustion characteristics may be affected by not only the mean shear flow but also the existence of inner and outer recirculation zones, flame-wall interaction and flame-acoustic interaction. Tanaka et al. [24] have conducted DNS of H_2/air turbulent swirling premixed flame in a cuboid combustor and investigated the characteristics of flow filed and effects of swirl number on total heat release rate and heat loss in the combustor. Aoki et al. [59] have identified the most dominant acoustic mode for pressure fields and heat release rate field, interactions with large-scale vortical motions in the combustor by applying dynamic mode decomposition (DMD) on the pressure and heat release rate fields. In their later study [61], contributions to disturbance energy source term based on exact energy disturbance budget. Minamoto et al. [60], have analyzed the DNS data [24, 59] and clarified the influences of scalar and turbulence velocity gradients on the chemical reactions through fine-scale mixing.

In this study, DNS of H_2-enriched CH_4/air turbulent swirling premixed flames in a cuboid combutor are conducted with same manners to previously reported studies for H_2/air [24, 59–61]. The governing equations considered in the present study are of fully compressible flow without low-mach number approximation.

In this chapter, numerical methods adopted in the present DNS are addressed and flow and combustion characteristics of from the results are investigated. Furthermore, the turbulent combustion conditions constructed by the turbulent statistics are clarified based on the Peters' turbulent combustion diagram [52].

2.2 Governing equations

2.2.1 Governing equations of reactive flows

The governing equations for fully compressible reactive flows with N_s species are the conservation of mass, momentum, energy and species mass fraction and can be written as follows,

· Mass

$$\frac{\partial \rho}{\partial t} + \nabla \cdot (\rho \boldsymbol{u}) = 0, \tag{2.1}$$

· Momentum

$$\frac{\partial (\rho \boldsymbol{u})}{\partial t} + \nabla \cdot (\rho \boldsymbol{u}\boldsymbol{u}) = -\nabla \cdot \boldsymbol{P} + \rho \sum_{i=1}^{N_s} Y_i \boldsymbol{f}_i, \tag{2.2}$$

· Energy

$$\rho \frac{\partial e_t}{\partial t} + \rho \boldsymbol{u} \cdot (\nabla e_t) = -\nabla \cdot \boldsymbol{q} - \boldsymbol{P} : (\nabla \boldsymbol{u}) + \rho \sum_{i=1}^{N_s} Y_i \boldsymbol{f}_i \cdot \boldsymbol{V}_i, \tag{2.3}$$

· Species mass fraction

$$\frac{\partial (\rho Y_i)}{\partial t} + \nabla \cdot (\rho \boldsymbol{u} Y_i) = -\nabla \cdot (\rho Y_i \boldsymbol{V}_i) + \omega_i. \tag{2.4}$$

Here, ρ, $\boldsymbol{u}$, e_t and Y_i denote density, velocity vector, internal energy and species mass fraction of the i-th species respectively. In addition, $\boldsymbol{f}_i$, $\boldsymbol{V}_i$, ω_i, W_i are external force, diffusion velocity, reaction rate and molecular weight of the i-th species. Species mass fraction, diffusion velocity and reaction rate satisfy following relations.

$$\sum_{i}^{N_s} Y_i = 1, \quad \sum_{i}^{N_s} Y_i \boldsymbol{V}_i = 0, \quad \sum_{i}^{N_s} \omega_i W_i = 0 \tag{2.5}$$

From the equations above, the number of equations to be solved becomes $N_s - 1$. Since the Newtonian fluid is considered in this study, the stress tensor $\boldsymbol{P}$ is given by

$$\boldsymbol{P} = \left[p + \left(\frac{2}{3}\mu - \kappa \right) (\nabla \cdot \boldsymbol{u}) \right] \boldsymbol{U} - \mu \left[(\nabla \boldsymbol{u}) + (\nabla \boldsymbol{u})^T \right], \tag{2.6}$$

where p, μ and κ denote pressure, dynamic and bulk viscosity. $\boldsymbol{U}$ is the unit tensor and the super script T means a transpose matrix. The heat flux $\boldsymbol{q}$ can be written as follows:

$$\boldsymbol{q} = -\lambda \nabla T + \rho \sum_{i=1}^{N_s} h_i Y_i \boldsymbol{V}_i + R^0 T \sum_{i=1}^{N_s} \sum_{j=1}^{N_s} \left(\frac{X_j D_{T,i}}{W_i D_{ij}} \right) \left(\boldsymbol{V}_i - \boldsymbol{V}_j \right) + \boldsymbol{q}_R. \tag{2.7}$$

In the Eq. (2.7), λ, R^0, and T denote the thermal conductivity, the universal gas constant and temperature respectively. $D_{T,i}$ is thermal diffusion coefficient and D_{ij} is the binary diffusion coefficient. h_i, X_i and W_i denote the enthalpy, the mole fraction and the molecular weight of the i-th species.

The diffusion velocity of the i-th species $\boldsymbol{V}_i$ is given as follows:

$$\begin{aligned} \nabla X_i &= \sum_{j=1}^{N_s} \left(\frac{X_i X_j}{D_{ij}} \right) \left(\boldsymbol{V}_j - \boldsymbol{V}_i \right) \\ &+ (Y_i - X_i) \frac{\nabla p}{p} + \frac{\rho}{p} \sum_{j=1}^{N_s} Y_i Y_j \left(\boldsymbol{f}_i - \boldsymbol{f}_j \right) \\ &+ \sum_{j=1}^{N_s} \left[\left(\frac{X_i X_j}{\rho D_{ij}} \right) \left(\frac{D_{T,j}}{Y_j} - \frac{D_{T,i}}{Y_i} \right) \right] \frac{\nabla T}{T}. \end{aligned} \tag{2.8}$$

To solve the equations, temperature T should be given as a known variable. However, since the temperature T is not given explicitly, T is determined by following relations.

$$e_t = \sum_{i=1}^{N_s} h_i Y_i - \frac{p}{\rho}, \tag{2.9}$$

$$h_i = \Delta h_i^0 + \int_{T_0}^{T} c_{p,\,i}\, dT. \tag{2.10}$$

In the Eq. (2.10), Δh_i^0 denotes the standard enthalpy of formation for the i-th species. Since the specific heat capacities of the i-th species at a constant pressure $c_{p,i}$ are also a function of temperature T, it is not realistic to determine temperature T accurately from Eqs. (2.9) and (2.10) which requires larger number of iterative calculations. Therefore, the energy conservation equation Eq. (2.3) is transformed into a conservation equation for (ρT) to determine temperature explicitly [62].

In the present DNS, following assumptions are made on the governing equations:

· No external force

$$\boldsymbol{f}_i = 0. \tag{2.11}$$

· Negligible Soret effect

$$\sum_{j=1}^{N_s} \left[\left(\frac{X_i X_j}{\rho D_{ij}} \right) \left(\frac{D_{T,j}}{Y_j} - \frac{D_{T,i}}{Y_i} \right) \right] \frac{\nabla T}{T} = 0. \tag{2.12}$$

· Negligible Dufour effect

$$R^0 T \sum_{i=1}^{N_s} \sum_{j=1}^{N_s} \left(\frac{X_j D_{T,i}}{W_i D_{ij}} \right) \left(\boldsymbol{V}_i - \boldsymbol{V}_j \right) = 0. \tag{2.13}$$

· Negligible pressure gradient diffusion

$$\left(Y_i - X_i \right) \frac{\nabla p}{p} = 0. \tag{2.14}$$

· Negligible bulk viscosity

$$\kappa = 0. \tag{2.15}$$

· Negligible radiative heat transfer

$$\boldsymbol{q}_R = 0. \tag{2.16}$$

With the assumptions above, the governing equations can be written as follows.

· Mass conservation

$$\frac{\partial \rho}{\partial t} + \nabla \cdot (\rho \boldsymbol{u}) = 0, \tag{2.17}$$

· Momentum conservation

$$\frac{\partial (\rho \boldsymbol{u})}{\partial t} + \nabla \cdot (\rho \boldsymbol{u}\boldsymbol{u}) = -\nabla \cdot \boldsymbol{P}, \tag{2.18}$$

· Energy conservation

$$\begin{aligned}\frac{\partial(\rho T)}{\partial t} + \nabla\cdot(\rho \boldsymbol{u} T) &= \frac{1}{\overline{c}_v}\nabla\cdot(\lambda\nabla T) - \frac{1}{\overline{c}_v}\sum_{i=1}^{N_s}\left(\rho Y_i \boldsymbol{V}_i c_{p,\,i}\cdot\nabla T\right) \\ &\quad -\frac{T}{\overline{c}_v}\sum_{i=1}^{N_s}\left[R_i\nabla\cdot(\rho Y_i \boldsymbol{V}_i)\right] - \frac{1}{\overline{c}_v}\boldsymbol{P}:(\nabla\boldsymbol{u}) \\ &\quad -\frac{1}{\overline{c}_v}\sum_{i=1}^{N_s}(h_i\omega_i) + \frac{T}{\overline{c}_v}\sum_{i=1}^{N_s}(R_i\omega_i), \end{aligned} \tag{2.19}$$

· Species mass conservation

$$\frac{\partial(\rho Y_i)}{\partial t} + \nabla\cdot(\rho \boldsymbol{u} Y_i) = -\nabla\cdot(\rho Y_i \boldsymbol{V}_i) + \omega_i. \tag{2.20}$$

In Eq. (2.19), $\overline{c}_v$ and R_i denote the mixture averaged specific heat capacity at a constant volume and characteristics gas constant of the i-th species. Here, $c_{v,i}$ denotes specific heat capacities at a constant volume of the i-th species.

$$\overline{c}_v = \sum_{i}^{N_s} c_{v,i} Y_i, \quad R_i = \frac{R^0}{W_i}. \tag{2.21}$$

As an auxiliary equation, the equation of state for ideal gas for multi component is used.

$$p = \rho R^0 T \sum_{i=1}^{N_s}\left(\frac{Y_i}{W_i}\right). \tag{2.22}$$

The stress tensor $\boldsymbol{P}$ is given by

$$\boldsymbol{P} = \left[p + \frac{2}{3}\mu(\nabla\cdot\boldsymbol{u})\right]\boldsymbol{U} - \mu\left[(\nabla\boldsymbol{u}) + (\nabla\boldsymbol{u})^T\right]. \tag{2.23}$$

On the right hand side of Eq. (2.19), ":" denotes the double dot product of two matrices and is calculated as follows.

$$\boldsymbol{P}:(\nabla\boldsymbol{u}) = (\boldsymbol{P}\cdot\nabla)\cdot\boldsymbol{u} = \sum_i\sum_j p_{ij}\frac{\partial u_i}{\partial x_j}. \tag{2.24}$$

The diffusion velocity $\boldsymbol{V}_i$ is given by

$$\boldsymbol{V}_i = -\frac{1}{X_i}D_{im}\nabla X_i, \tag{2.25}$$

where D_{im} is the mixture diffusion coefficient for the i-th species. The mixture diffusion coefficient is obtained by using binary diffusion coefficients D_{ij} as follows.

$$D_{im} = -\frac{1 - Y_i}{\sum_{i \neq j}^{N_s} X_i / D_{ij}}. \tag{2.26}$$

2.2.2 Chemical reaction

The forward and backward reactions of a general k set of reactions can be written as follows:

$$\sum_{i=1}^{N_s} \nu'_{i,k} X_i \rightleftharpoons \sum_{i=1}^{N_s} \nu''_{i,k} X_i. \tag{2.27}$$

Here, $\nu'_{i,k}$ and $\nu''_{i,k}$ are the stoichiometric coefficient for the i-th species in the k-th elemental reaction. N_s is the number of species and N_r is the number of elemental reactions. The reaction rate of the i-th species ω_i is expressed

$$\omega_i = \sum_{k=1}^{N_r} (\nu''_{i,k} - \nu'_{i,k}) q_k, \tag{2.28}$$

the rate of progress variable q_k can be written as:

$$q_k = k_{f_k} \prod_{i=1}^{N_s} [X_i]^{\nu'_{i,k}} - k_{r_k} \prod_{i=1}^{N_s} [X_i]^{\nu''_{i,k}}. \tag{2.29}$$

In Eq. (2.29), k_{f_k} and k_{r_k} denote the forward and backward rate constants. k_{fk} is assumed to follow Arrhenius temperature dependence form.

$$k_{f_k} = A_k T^{\beta_k} \exp\left(\frac{-E_k}{R_c T}\right). \tag{2.30}$$

Here, A_k, β_k and E_k are the pre-exponential factor, the temperature exponent and the activation energy for each elemental reactions. R_c is the universal gas constant of which dimension is [cal/(K mol)]. Supposing that the molar concentration of i-th species $[X_i]$ is $[\mathrm{mol/cm^3}]$, the dimension of A_k in unimolecular, bimolecular and trimolecular reaction becomes $[1/(\mathrm{s \cdot K^{\beta_k}})]$, $[\mathrm{cm^3/(mol \cdot s \cdot K^{\beta_k})}]$, $[\mathrm{cm^6/(mol^2 \cdot}$

$\mathrm{s} \cdot \mathrm{K}^{\beta_k})]$ respectively. The backward reaction rate coefficient k_{r_k} is obtained by using the equilibrium constant of the k-th elemental reaction K_{c_k}.

$$k_{r_k} = \left(\frac{k_{f_k}}{K_{c_k}}\right). \tag{2.31}$$

The equilibrium constant K_{c_k} is given by

$$K_{c_k} = K_{p_k}\left(\frac{P_{atm}}{R^0 T}\right)^{\sum_{i=1}^{N_s}(\nu''_{i,k}-\nu'_{i,k})}, \tag{2.32}$$

where the equilibrium constant K_{P_k} is obtained by using the entropy and enthalpy of the k-th elemental reaction.

$$K_{p_k} = \exp\left(\frac{\Delta S_k}{R^0} - \frac{\Delta H_k}{R^0 T}\right). \tag{2.33}$$

In Eq. (2.33), ΔS_k and ΔH_k can be calculated as follows.

$$\frac{\Delta S_k}{R^0} = \sum_{i=1}^{N_s}(\nu''_{i,k} - \nu'_{i,k})\frac{S_i}{R^0}, \tag{2.34}$$

$$\frac{\Delta H_k}{R^0 T} = \sum_{i=1}^{N_s}(\nu''_{i,k} - \nu'_{i,k})\frac{H_i}{R^0 T}. \tag{2.35}$$

Three-body reactions

In some chemical reactions, a third body element may be required to advance the reaction as the following equation,

$$\mathrm{H} + \mathrm{O_2} + \mathrm{M} \rightleftharpoons \mathrm{HO_2} + \mathrm{M}$$

In such a case, the concentration of third body element is considered to be calculated by the forward reaction rate q_k and Eq. (2.29) becomes,

$$q_k = \left(\sum_{i=1}^{N_s}\alpha_{i,k}[X_i]\right)\left(k_{f_k}\prod_{i=1}^{N_s}[X_i]^{\nu'_{i,k}} - k_{r_k}\prod_{i=1}^{N_s}[X_i]^{\nu''_{i,k}}\right). \tag{2.36}$$

Here, $\alpha_{i,k}$ is the contribution as a third body element for the i-th species in the k-th elemental reaction. $\alpha_{i,k}$ becomes 1 when all of the species contribute to the

reaction equally as a third body, and the first term becomes,

$$[M] = \sum_{i=1}^{N_s} [X_i]. \tag{2.37}$$

However, in many cases, the contributions as a third body element are higher for some species than other species.

Fall-off Reaction

Under certain conditions, some reaction expressions depend on both temperature and pressure. The fall-off reaction is an example of pressure dependent reactions. Methyl recombination reaction is one of the fall-off reaction. In the high-pressure limit, the reaction is described as:

$$CH_3 + CH_3 \rightleftharpoons C_2H_6$$

On the other hand, in the low-pressure limit, energy supply by collision of a third-body element is needed to proceed the reaction. Therefore, the description of the reaction for the low-pressure limit is

$$CH_3 + CH_3 + M \rightleftharpoons C_2H_6 + M$$

The reaction rate constant is a function of temperature T, either the reaction is at the low-pressure limit of high-pressure limit. However, depending on the temperature and pressure, the reaction may be between the limits and the expression of the reaction rate becomes very complicated. Such a region is called as fall-off region and the dependence of reaction on the pressure is expressed by (+M).

$$CH_3 + CH_3(+M) \rightleftharpoons C_2H_6(+M)$$

In the fall-off region, the reaction rate constants in the Arrhenius form for the low pressure limit (k_0) and the high pressure limit (k_∞) can be written as follows respectively:

$$k_0 = A_0 T^{\beta_0} \exp\left(\frac{-E_0}{R_c T}\right), \tag{2.38}$$

$$k_\infty = A_\infty T^{\beta_\infty} \exp\left(\frac{-E_\infty}{R_c T}\right). \tag{2.39}$$

The reaction rate constant at any pressure is given by

$$k = k_\infty \left(\frac{P_r}{1 + P_r} \right) F, \tag{2.40}$$

where, the reduced press P_r is given as,

$$P_r = \frac{k_0[M]}{k_\infty}. \tag{2.41}$$

Here, $[M]$ is the molar concentration of the mixture and if $F = 1$, it becomes Lindemann form. In the present DNS, Troe form is adopted as a fall-off reaction in the chemical mechanism used and F is given by

$$\log F = \left\{ 1 + \left[\frac{\log P_r + c}{n - d(\log P_r + c)} \right]^2 \right\}^{-1} \log F_{\text{cent}}. \tag{2.42}$$

The constants in the Eq.(2.42) are

$$c = -0.4 - 0.67 \log F_{\text{cent}}, \tag{2.43}$$

$$n = 0.75 - 1.27 \log F_{\text{cent}}, \tag{2.44}$$

$$d = 0.14. \tag{2.45}$$

F_{cent} can be expressed a function of temperature:

$$F_{\text{cent}} = (1 - \alpha) \exp\left(\frac{-T}{T^{***}} \right) + \alpha \exp\left(\frac{-T}{T^{*}} \right) + \exp\left(\frac{-T^{**}}{T} \right). \tag{2.46}$$

The four parameters, α, T^{*}, T^{**}, T^{***} are included in the description of reactions.

2.2.3 Thermodynamic properties

The temperature dependence of the thermodynamic and transport properties (viscosity, thermal conductivity and diffusion coefficient) are considered by using CHEMKIN-II packages [63, 64] with vector and parallel computation modification. In this study, the thermodynamic and transport properties are only functions of temperature by assuming ideal gas. The molar heat capacities at a constant pressure are given by polynomial fits:

$$\frac{C_{p,i}}{R^0} = \sum_{n=1}^{N} a_{n,i} T^{(n-1)}. \tag{2.47}$$

The standard-state molar enthalpy is given by

$$H_i = \int_0^T C_{p,i} dT. \tag{2.48}$$

Substituting Eq. (2.48) into Eq. (2.47),

$$\frac{H_i}{R^0 T} = \sum_{i=1}^{N} \frac{a_{n,i} T^{(n-1)}}{n} + \frac{a_{N+1,i}}{T}. \tag{2.49}$$

In the Eq. (2.49), the integral constant $a_{N+1,i}$ is the standard enthalpy of formation at 0 K. However, since the representative of polynomial is not valid near 0 K, the integral constant is determined from the standard enthalpy of formation at 298 K. Therefore, the enthalpy of the i-th species can be written as:

$$H_i = \int_{298}^T C_{p,i} dT + H_i(298). \tag{2.50}$$

The entropy of the i-th species at atmospheric pressure can be obtained by integrating the specific heat.

$$S_i^0 = \int_0^T \frac{C_{p,i}}{T} dT. \tag{2.51}$$

Substituting Eq. (2.51) into Eq. (2.47) yields

$$\frac{S_i^0}{R^0} = a_{1,i} \ln T + \sum_{n=2}^{N} \frac{a_{n,i} T^{(n-1)}}{n-1} + a_{N+2,i}. \tag{2.52}$$

For the same reason of determining $a_{N+1,i}$, the integral constant $a_{N+2,i}$ is determined by the standard enthalpy of formation at 298 K. While the above polynomials are expressed by an arbitrary order, N is for until 5 and the coefficients of thermodynamic data in NASA chemical equilibrium code are used in the present DNS. $c_{p,i}$ and $\overline{c_v}$ in Eq. (2.19) are correlated to $C_{p,i}$ and given as follows.

$$c_{p,i} = C_{p,i}/W_i, \tag{2.53}$$

$$C_{v,i} = C_{p,i} - R^0, \tag{2.54}$$

$$c_{v,i} = C_{v,i}/W_i, \tag{2.55}$$

$$\overline{c_v} = \sum_{i=1}^{N_s} c_v Y_i. \tag{2.56}$$

2.2.4 Transport coefficients

The viscosity η_i, thermal conductivity λ_i and the binary diffusion coefficient D_{ij} for the i-th species are computed by applying fitting procedure as a function of temperature T.

$$\ln \eta_i = \sum_{n=1}^{N} a_{n,i} (\ln T)^{n-1}, \tag{2.57}$$

$$\ln \lambda_i = \sum_{n=1}^{N} b_{n,i} (\ln T)^{n-1}, \tag{2.58}$$

$$\ln D_{ij} = \sum_{n=1}^{N} c_{n,i} (\ln T)^{n-1}. \tag{2.59}$$

Here, the constants $a_{n,i}$, $b_{n,i}$ and $c_{n,i}$ are calculated for until $N = 4$ by using TRANSPORT of CHEMKIN PACKAGE [64] . By using the values of η_i, λ_i, D_{ij}, the viscosity μ, the thermal conductivity λ and the diffusivity of the i-th species D_{im} in the multi component system are calculated as,

$$\mu = \sum_{i=1}^{N_s} \frac{X_i \eta_i}{\sum_{j \neq i}^{I} X_j \Phi_{ij}}, \tag{2.60}$$

$$\lambda = \frac{1}{2} \left(\sum_{i=1}^{N_s} X_i \lambda_i + \frac{1}{\sum_{i=1}^{N_s} X_i / \lambda_i} \right), \tag{2.61}$$

$$D_{im} = \frac{\sum_{j \neq i}^{N_s} X_j W_j}{\overline{W} \sum_{j \neq i}^{I} X_j / D_{ij}}, \tag{2.62}$$

where, Φ_{ij} is calculated as follows

$$\Phi_{ij} = \frac{1}{\sqrt{8}} \left(1 + \frac{W_i}{W_j} \right)^{-\frac{1}{2}} \left\{ 1 + \left(\frac{\eta_i}{\eta_j} \right)^{\frac{1}{2}} \left(\frac{W_j}{W_i} \right)^{\frac{1}{4}} \right\}^2. \tag{2.63}$$

2.3 Computational methods

2.3.1 Spatial discretization

In the present DNS, the governing equations are discretized by using a fourth-order central finite difference scheme in all directions. The partial derivatives of a

function f_i with respect to x_k direction at a discretized point i can be written as:

$$\left(\frac{\partial f}{\partial x_k}\right)_i = \frac{-f_{i+2} + 8f_{i+1} - 8f_{i-1} + f_{i-2}}{12\Delta x_k} \tag{2.64}$$

For the domain boundaries, the derivatives are given by the following equations.

$$\left(\frac{\partial f}{\partial x_k}\right)_1 = \frac{-25f_1 + 48f_2 - 36f_3 + 16f_4 - 3f_5}{12\Delta x_k}, \tag{2.65}$$

$$\left(\frac{\partial f}{\partial x_k}\right)_2 = \frac{-3f_1 - 10f_2 + 18f_3 - 6f_4 + f_5}{12\Delta x_k}, \tag{2.66}$$

$$\left(\frac{\partial f}{\partial x_k}\right)_{N_{k-1}} = \frac{3f_{N_k} + 10f_{N_k-1} - 18f_{N_k-2} + 6f_{N_k-3} - f_{N_k-4}}{12\Delta x_k}, \tag{2.67}$$

$$\left(\frac{\partial f}{\partial x_k}\right)_{N_k} = \frac{25f_{N_k} - 48f_{N_k-1} + 36f_{N_k-2} - 16f_{N_k-3} + 3f_{N_k-4}}{12\Delta x_k}, \tag{2.68}$$

Here, N_k denotes the number of grid points in the x_k direction.

2.3.2 Spatial filter

In the case of difference scheme is used, unphysical oscillation with higher frequencies than the spatial resolution may occur. To eliminate the unphysical oscillation, explicit spatial filter based on compact finite difference schemes [65] is applied to density ρ, temperature (ρT), velocity components ($\rho \boldsymbol{u}$) and mass fraction Y_i,

$$\hat{f}_i = af_i + \frac{d}{2}(f_{i+3} + f_{i-3}) + \frac{c}{2}(f_{i+2} + f_{i-2}) + \frac{b}{2}(f_{i+1} + f_{i-1}). \tag{2.69}$$

In Eq. (2.69), $\hat{f}_i$ denotes the filtered values at node x_i. The coefficients, a, b, c and d are determined by matching the Taylor series expansion coefficients. In this study, assuming that the sixth order explicit spatial filter is used and the coefficients a, b, c and d are determined as

$$a = \frac{11}{16}, \quad b = \frac{15}{32}, \quad c = -\frac{3}{16}, \quad d = \frac{1}{32} \tag{2.70}$$

Since the periodic boundary condition is not imposed on the domain boundaries in this study, a fourth order explicit filter is applied near to the domain boundaries.

$$\hat{f}_1 = \frac{15}{16} f_1 + \frac{1}{16}(4f_2 - 6f_3 + 4f_4 - f_5) \tag{2.71}$$

$$\hat{f}_2 = \frac{3}{4} f_2 + \frac{1}{16}(f_1 + 6f_3 - 4f_4 + f_5) \tag{2.72}$$

$$\hat{f}_3 = \frac{5}{8} f_3 + \frac{1}{16}(-f_1 + 4f_2 + 4f_4 - f_5) \tag{2.73}$$

$$\hat{f}_{N_k-2} = \frac{5}{8} f_{N_k-2} + \frac{1}{16}(-f_{N_k} + 4f_{N_k-1} + 4f_{N_k-3} - f_{N_k-4}) \tag{2.74}$$

$$\hat{f}_{N_k-1} = \frac{3}{4} f_{N_k-1} + \frac{1}{16}(f_{N_k} + 6f_{N_k-2} - 4f_{N_k-3} + f_{N_k-4}) \tag{2.75}$$

$$\hat{f}_{N_k} = \frac{15}{16} f_{N_k} + \frac{1}{16}(4f_{N_k-1} - 6f_{N_k-2} + 4f_{N_k-3} - f_{N_k-4}) \tag{2.76}$$

2.3.3 Boundary conditions

In DNS of compressible flows, such as combustion, the pressure waves generated by the flame propagates in the direction normal to the flame front at the speed of sound. When periodic boundary conditions used for non-reactive homogeneous isotropic turbulence are applied, the pressure waves keep propagating through the computational domain and result in unphysical phenomena. Reflection of waves at the boundary occurs even for the case of imposing the outflow boundary conditions by setting the gradient of variables to be zero. These unphysical and numerical reflected waves propagate through the computational domain and affect the results of laminar or turbulent reactive flow simulations. The reflected acoustic waves are offset by the numerical viscosity of the schemes used in many cases. However, when a high order difference scheme is used for high resolution DNS, the numerical viscosity is very small and propagation of the reflected waves from the walls is problematic for the reliability of DNS results.

From the reasons above, Thompson [66] has applied non-reflecting conditions to the Euler equations by suppressing the amplitude of reflected waves with characteristics wave analysis. The boundary conditions are extended by to Navier-Stokes equations by Poinsot et al. [67, 68] and called as NSCBC (Navier-Stokes Charac-

teristic Boundary Condition). NSCBC is applied widely as boundary conditions for compressible viscous flows. In this study, since the computational domain consists of inflow, outflow and surrounding iso-thermal and no-slip walls a shown in Fig. 2.1 is considered, NSCBC is applied for all directions.

Governing equations of NSCBC

At the boundary of x-direction, the governing equations for NSCBC can be written as follows.

$$\frac{\partial \rho}{\partial t} + d_1 + \frac{\partial \rho v}{\partial y} + \frac{\partial \rho w}{\partial z} = 0, \tag{2.77}$$

$$\frac{\partial \rho u}{\partial t} + u d_1 + \rho d_3 + \frac{\partial \rho u v}{\partial y} + \frac{\partial \rho u w}{\partial z} = \frac{\partial \tau_{1j}}{\partial x_j}, \tag{2.78}$$

$$\frac{\partial \rho v}{\partial t} + v d_1 + \rho d_4 + \frac{\partial \rho v v}{\partial y} + \frac{\partial \rho v w}{\partial z} = \frac{\partial \tau_{2j}}{\partial x_j}, \tag{2.79}$$

$$\frac{\partial \rho w}{\partial t} + w d_1 + \rho d_5 + \frac{\partial \rho w v}{\partial y} + \frac{\partial \rho w w}{\partial z} = \frac{\partial \tau_{3j}}{\partial x_j}, \tag{2.80}$$

$$\frac{\partial \rho T}{\partial t} + d_2 + \frac{\partial \rho v T}{\partial y} + \frac{\partial \rho w T}{\partial z} + \frac{1}{\overline{c}_v} p \frac{\partial v}{\partial y} + \frac{1}{\overline{c}_v} p \frac{\partial w}{\partial z} = \frac{1}{\overline{c}_v} \frac{\partial}{\partial x_j} \left(\lambda \frac{\partial T}{\partial x_j} \right) + \cdots, \tag{2.81}$$

$$\frac{\partial Y_i}{\partial t} + d_{\mathrm{SP},i} + v \frac{\partial \rho Y_i}{\partial y} + w \frac{\partial \rho Y_i}{\partial z} = -\frac{1}{\rho} \frac{\partial \rho Y_i V_{i,j}}{\partial x_j}. \tag{2.82}$$

Here, τ_{ij} denotes viscous stress tensor and the subscripts 1, 2 and 3 denote x-, y- and z-direction respectively. Comparing the governing equations (2.17)-(2.20) and equations (2.77)-(2.82), the difference is derivative terms with respect to x are replaced by d_i except for viscous term. d_i can be written as follows.

$$d_1 = \frac{\partial \rho u}{\partial x} = \frac{1}{c^2}\left[\mathscr{L}_2 + \frac{1}{2}\left(\mathscr{L}_5 + \mathscr{L}_1\right)\right], \tag{2.83}$$

$$\begin{aligned} d_2 =& \frac{\partial \rho u T}{\partial x} + \frac{1}{\overline{c}_v} p \frac{\partial u}{\partial x} \\ =& \frac{1}{R^0 \sum \left(Y_i / W_i\right)}\left[\frac{u}{2}\left(\frac{\mathscr{L}_5}{u+c} + \frac{\mathscr{L}_1}{u-c}\right) + \rho R^0 T \sum_{i=1}^{N} \frac{\mathscr{L}_{\mathrm{SP},\,i}}{W_i}\right] \\ &+ \frac{T}{2c}\left(\frac{\mathscr{L}_5}{u+c} - \frac{\mathscr{L}_1}{u-c}\right) + \frac{1}{2c}\frac{R^0 \sum \left(Y_i / W_i\right) T}{\overline{c}_v}\left(\frac{\mathscr{L}_5}{u+c} - \frac{\mathscr{L}_1}{u-c}\right), \end{aligned} \tag{2.84}$$

$$d_3 = \frac{\partial u u}{\partial x} = \frac{1}{2\rho c}\left(\mathscr{L}_5 - \mathscr{L}_1\right), \tag{2.85}$$

$$d_4 = \frac{\partial u v}{\partial x} = \mathscr{L}_3, \tag{2.86}$$

$$d_5 = \frac{\partial u w}{\partial x} = \mathscr{L}_4, \tag{2.87}$$

$$d_{\mathrm{SP},i} = u \frac{\partial Y_i}{\partial x} = \mathscr{L}_{\mathrm{SP},i}. \tag{2.88}$$

where c is the speed of sound and computed as:

$$c = \sqrt{\frac{\gamma p}{\rho}} \tag{2.89}$$

$\mathscr{L}_i$ denotes the the amplitude variations of the characteristic waves crossing the boundary.

$$\mathscr{L}_1 = \lambda_1\left(\frac{\partial p}{\partial x} - \rho c \frac{\partial u}{\partial x}\right), \tag{2.90}$$

$$\mathscr{L}_2 = \lambda_2\left(c^2 \frac{\partial \rho}{\partial x} - \frac{\partial p}{\partial x}\right), \tag{2.91}$$

$$\mathscr{L}_3 = \lambda_3 \frac{\partial v}{\partial x}, \tag{2.92}$$

$$\mathscr{L}_4 = \lambda_4 \frac{\partial w}{\partial x}, \tag{2.93}$$

$$\mathscr{L}_5 = \lambda_5\left(\frac{\partial p}{\partial x} + \rho c \frac{\partial u}{\partial x}\right), \tag{2.94}$$

$$\mathscr{L}_{\mathrm{SP},\,i} = \lambda_{\mathrm{SP},\,i} \frac{\partial Y_i}{\partial x}. \tag{2.95}$$

The characteristic velocity of each characteristic wave can be written as

$$\lambda_1 = u - c, \tag{2.96}$$

$$\lambda_2 = \lambda_3 = \lambda_4 = \lambda_{\mathrm{SP},\,i} = u, \tag{2.97}$$

$$\lambda_5 = u + c. \tag{2.98}$$

Perfectly non-reflecting conditions

For the perfectly non-reflecting conditions, the amplitude variations of the waves entering into the computational domain $\mathscr{L}_i$ is set to be 0.

$$\mathscr{L}_i = 0. \tag{2.99}$$

The derivative terms appear in $\mathscr{L}_i$ is calculated from the interior points. With the equation above, following condition is needed.

$$\frac{\partial \tau_{11}}{\partial x} = 0. \tag{2.100}$$

Non-reflecting conditions

In the perfectly non-reflecting conditions, the information of pressure at infinity is not fed back to the computational domain. While for the non-reflecting conditions, $\mathscr{L}_2 \sim \mathscr{L}_{\mathrm{SP},i}$ are 0 same to the perfectly non-reflecting conditions,

$$\mathscr{L}_2 = \mathscr{L}_3 = \mathscr{L}_4 = \mathscr{L}_5 = \mathscr{L}_{\mathrm{SP},\,i} = 0. \tag{2.101}$$

$\mathscr{L}_{1,NF}$ denotes the constant pressure at infinity instead of $\mathscr{L}_1$ as:

$$\mathscr{L}_{1,\,NF} = K\left(p - p_\infty\right). \tag{2.102}$$

Here, p_∞ is the constant pressure at infinity and K is determined as:

$$K = \frac{\sigma\left(1 - M^2\right)c}{L_0}. \tag{2.103}$$

Here, σ is a constant, M is the maximum of Mach number in the flow and L_0 is the characteristic size of the domain. For the case of $\sigma = 0$, the magnitude of reflected

wave K becomes 0 and corresponds to the perfectly non-reflecting conditions. For the non-reflecting conditions, additional conditions should be satisfied as follows.

$$\frac{\partial \tau_{12}}{\partial x} = 0, \tag{2.104}$$

$$\frac{\partial}{\partial x}\left(\lambda \frac{\partial T}{\partial x}\right) = 0, \tag{2.105}$$

$$\frac{\partial}{\partial x}\left(\rho Y_i V_{i,x}\right) = 0. \tag{2.106}$$

Isothermal no-slip wall conditions

In this study, isothermal and no-slip wall boundary condition is imposed. Boundary conditions of density, velocity and temperature at the wall along the x-direction can be written as:

$$\frac{\partial \rho}{\partial t} + \frac{1}{c}\left(\frac{\partial p}{\partial x} + \rho c \frac{\partial u}{\partial x}\right) = 0, \tag{2.107}$$

$$u = v = 0, \tag{2.108}$$

$$T = \text{const.} \tag{2.109}$$

Equation (2.4) can be rewritten as follows imposing that the reactive species are inert and the flux is 0 at the wall

$$\frac{\partial(\rho Y_i)}{\partial t} = -\nabla \cdot (\rho Y_i \boldsymbol{V}_i)\,. \tag{2.110}$$

Since the species can not the flow through the wall by diffusion, the value at the boundary for each species is determined as:

$$\boldsymbol{V}_i \cdot \boldsymbol{n} = 0, \tag{2.111}$$

where $\boldsymbol{n}$ denotes the vector normal to the wall. In this study, to satisfy the equation above, mass fraction at the wall is set in which its gradient to be 0 in the spatial discretization.

2.3.4 Time integration

The governing equations are integrated in time by using a low storage third-order Runge-Kutta scheme [69]. In this scheme, a variable u at an instance of n (u^n) is advanced in time to $n+1$ (u^{n+1}) with time stepping Δt by three stages as follows:

$$\Delta u^n = \left(\frac{\partial u_k}{\partial t}\right)^n, \tag{2.112}$$

$$u^{n'} = u^n + \Delta u^n \times \frac{1}{3}\Delta t, \tag{2.113}$$

$$\Delta u^{n'} = \left\{-\frac{5}{9}\Delta u^n + \left(\frac{\partial u}{\partial t}\right)^n\right\}, \tag{2.114}$$

$$u^{n''} = u^{n'} + \Delta u^{n'} \times \frac{15}{16}\Delta t, \tag{2.115}$$

$$\Delta u^{n''} = \left\{-\frac{153}{128}\Delta n^{n'} + \left(\frac{\partial u}{\partial t}\right)^{n''}\right\}, \tag{2.116}$$

$$u^{n+1} = u^{n''} + \Delta u^{n''} \times \frac{8}{15}\Delta t. \tag{2.117}$$

Since this scheme is an explicit scheme, the time stepping Δt should be smaller than the smallest time scale of the flow field to ensure the numerical stability. In DNS of reactive flows, the time stepping Δt can be determined base on Courant number, diffusion number and chemical time scale and so on. In combustion DNS, restriction by CFL condition becomes intense due to increased speed of sound which increases in high temperature region and smaller grid size for spatial resolution. Depending on the situation, restriction may be more severe because of the smallest chemical time scale which is much smaller than the time stepping Δt which is determined by CFL condition. However, integrating such a small time stepping is not feasible. To mitigate the restriction of time stepping for the chemical reaction terms in energy conservation equation (Eq. 2.19) and species conservation equation (Eq. 2.20), multi-timescale (MTS) method [17] is implemented. In addition, correlated adaptive chemistry and transport (CO-DACT) [18, 19] is

adopted to reduce computational cost by reduction of reaction ordinary differential equation (ODE) system and computation of transport properties.

Multi-times scale (MTS) method

The terms except for the chemical reaction term in the governing equations are integrated in time by using a third-order Runge-Kutta scheme and intermediate time step of the temperature and reactive species, T^* and Y_i^* are calculated as:

$$\frac{\rho T^* - \rho T^n}{dt} = -\nabla \cdot (\rho \boldsymbol{u} T) + \frac{1}{\overline{c}_v}\nabla \cdot (\lambda \nabla T) - \frac{1}{\overline{c}_v}\sum_{i=1}^{N_s}\left(\rho Y_i \boldsymbol{V}_i c_{p,i} \cdot \nabla T\right) - \frac{T}{\overline{c}_v}\sum_{i=1}^{N_s}\left[R_i \nabla \cdot (\rho Y_i \boldsymbol{V}_i)\right] - \frac{1}{\overline{c}_v}\boldsymbol{P} : (\nabla \boldsymbol{u}), \tag{2.118}$$

$$\frac{\rho Y_i^* - \rho Y_i^n}{dt} = \nabla \cdot (\rho \boldsymbol{u} Y_i) - \nabla \cdot (\rho Y_i \boldsymbol{V}_i). \tag{2.119}$$

The chemical reaction terms are advanced in time by using multi-times scale (MTS) [17] method and T^{n+1}, Y_i^{n+1} are determined as:

$$\frac{\rho T^{n+1} - \rho T^*}{dt} = -\frac{1}{\overline{c}_v}\sum_{i=1}^{N}(h_i \omega_i) + \frac{T}{\overline{c}_v}\sum_{i=1}^{N}(R_i \omega_i), \tag{2.120}$$

$$\frac{\rho Y_i^{n+1} - \rho Y_i^*}{dt} = \omega_i. \tag{2.121}$$

MTS [17] is an algorithm for integrating ordinary differential equations (ODEs) associated with chemical reaction using a large Δt. In this method, each chemical species Y_i belongs to one integration group based on its chemical timescale (τ_i). The index (M) of an integration group in which Y_i belongs to is obtained as

$$M = \log_{10}(\Delta t / \tau_i) + 1. \tag{2.122}$$

Species in the M-th group are integrated using a time step Δt_M given as :

$$\Delta t_M = \Delta t / 10^{(M-1)}. \tag{2.123}$$

The integration procedure starts with the smallest Δt_M. After convergence of the M-th group, the species mass fractions in the M-th group are fixed and then the ODE system continues to be integrated using Δt_{M-1}. Thus, MTS enables integration of chemical reaction term with a large Δt, which is not limited by the smallest chemical timescale, as a global time stepping for DNS.

CO-DACT

In CODAC [18] method, a phase space consisting of a few key parameters is constructed. Temperature and mass fractions of fuel, oxidizer and important radicals are selected as the key parameters. Comparing the instantaneous phase parameters at a grid point with those at another reference point (different point in time/space), correlation between the two points in the phase space is examined. Threshold values used for examining the correlation are specified by a user. If the phase parameters at the two points are correlated, the reduced mechanism used at the reference point is reused at the correlated grid point. If the phase parameters at a grid point are not correlated with any other reference point, a new reduced mechanism needs to be generated by PFA (path flux analysis) [70].

Further reduction of computational cost is achieved by using CO-DACT (CO-DAC and transport) [19]. The same correlation procedure in CODAC is applied to reducing the computation of transport properties, such as viscosity, diffusivity and thermal conductivity. The phase parameters for reducing transport calculation are temperature and molar fractions of the first several abundant species. As with CODAC, transport properties at a grid point are not calculated if the phase parameters at the point are correlated with those at a different grid point.

2.3.5 Swirling velocity profiles

In this study, the inflow velocity profiles at the inlet $u_{i,\mathrm{in}}$ consist of mean velocity profiles $u_{i,\mathrm{base}}$ and velocity perturbations u_i'.

$$u_{i,\mathrm{in}} = u_{i,\mathrm{base}} + u_i' \tag{2.124}$$

The mean profiles of radial (u_r), azimuthal (u_θ) and axial (u_x) velocity components of an annular swirling flow at the inlet are analytically determined as a function of radial distance $r = \sqrt{y^2 + z^2}$. The profiles are obtained by solving steady Navier-Stokes equations in cylindrical coordinate system with no-slip wall boundary conditions.

$$u_{r,\text{base}} = 0, \tag{2.125}$$

$$u_{\theta,\text{base}} = f_\theta \left(\frac{r^2}{3} + c_1 r + \frac{c_2}{r} \right) = f_\theta U_\theta, \tag{2.126}$$

$$u_{x,\text{base}} = \left[\left(\frac{r}{R_\text{out}} \right)^2 - \frac{R^2 - 1}{\text{lnR}} \ln \left(\frac{r}{R_\text{out}} \right) - 1 \right] c_3 u_x^b. \tag{2.127}$$

Here, $R_\text{out} = D_\text{out}/2, R_\text{in} = D_\text{in}/2$ and $R = R_\text{in}/R_\text{out}$. f_θ denotes the coefficient of external force in θ-direction and u_x^b denotes the mean axial velocity at the inlet. The integral constants c_1, c_2 and c_3 are determined by imposing no-slip wall conditions at $r = R_\text{in}$ and R_out and the relation between u_x and u_x^b.

$$c_1 = -\frac{R_\text{out}(R^2 + R + 1)}{3(1 + R)}, \tag{2.128}$$

$$c_2 = \frac{R_\text{out}^3 R^2}{3(1 + R)}, \tag{2.129}$$

$$c_3 = -\frac{2\ln R}{R^2(\ln R - 1) + 1 + \ln R}. \tag{2.130}$$

The swirl number S defined in Eq. (2.131) is used to determine the azimuthal velocity U_θ.

$$S = \frac{\int_{R_\text{in}}^{R_\text{out}} u_{\theta,\text{base}} u_{x,\text{base}} r^2 dr}{(R_\text{out} - R_\text{in}) \int_{R_\text{in}}^{R_\text{out}} u_{x,\text{base}}^2 r dr}. \tag{2.131}$$

By substituting Eq. (2.126) into Eq. (2.131), the external force coefficient f_θ is determined and the mean velocity profiles at the inlet are obtained.

$$f_\theta = S\frac{(R_{\text{out}} - R_{\text{in}})\int_{R_{\text{in}}}^{R_{\text{out}}} u_{x,\text{base}}^2 r\,dr}{\int_{R_{\text{in}}}^{R_{\text{out}}} U_\theta u_{x,\text{base}} r^2 dr}. \tag{2.132}$$

From the equations above, the mean velocity profiles are determined by four parameters R_{in}, R_{out}, u_x^b and S. The mean velocity profiles for $S = 1.2$ are shown in Fig. 2.3.

The inflow velocity perturbations u' added to the mean velocity profile in Eq. (2.124) follows the same manners to Wang et al. [71] to promote transition from laminar to turbulent flow. The perturbations consist of simple white noise in which each frequency has a randomly-given lifetime for its phase as:

$$u_i'(r,\theta,t) = A\sum_{j=1}^{N_f} \phi(r)\sin\left\{2\pi f_j t + \Phi_{ij}(r,\theta,\tau_{ij})\right\}, \tag{2.133}$$

where Φ_{ij} and τ_{ij} denote phase and lifetime of the phase for each frequency and given by uniform random numbers independent of r, θ and f_i. A frequency component of f_j for a velocity perturbation in the i-direction at a fixed point at the inflow boundary inflows with phase of Φ_{ij} during its life time τ_{ij}. After its life time of τ_{ij}, the frequency component will inflow with a new phase and its new lifetime. In this manner, randomly given velocity perturbations which do not have specific periodicity are produced. In this study, frequencies are set to be 3.061 kHz $\leq f_j \leq$ 1224 kHz. The number of modes for the frequencies N_f is 120 and the sinusoidal waves with f_j are superimposed. $\phi(r)$ is turbulence intensity variation and given as follows in order to increase its intensity near the wall:

$$\phi(r) = 1 - \exp\left[-c_4\left(r - \frac{R_{\text{out}} + R_{\text{in}}}{2}\right)^2\right], \tag{2.134}$$

where, the coefficient c_4 is set to be $c_4 \approx 9.2\text{mm}^{-2}$ to promote laminar to turbulent flow transition. The amplitude A is determined by the maximum velocity

perturbation intensity $u'_{\max}$ and the number of modes N_f.

$$A = \frac{u'_{\max}}{\sqrt{N_f}}, \tag{2.135}$$

$$u'_{\max} = \sqrt{\frac{{u'_r}^2 + {u'_\theta}^2 + {u'_x}^2}{3}}. \tag{2.136}$$

While the amplitude A is given as a simple white noise with constant value for all of f_j in the present DNS, different values of A can be given for each f_j. In such a case, Eq. (2.133) can be expressed as:

$$u'_i(r,\theta,t) = \sum_{j=1}^{N_f} A_j \phi(r) \sin\left\{2\pi f_j t + \Phi_{ij}(r,\theta,\tau_{ij})\right\}. \tag{2.137}$$

As for the values of amplitude A_j, for example, it is shown in [72] that energy spectrum of inflow perturbations which are similar to the energy spectrum of the original homogeneous isotropic turbulence (HIT) can be obtained by using Eq. (2.137) imposing the banded noise having the amplitude spectra obtained from energy spectra of the original HIT.

2.3.6 Computational conditions

To investigate the effects of hydrogen addition on the structures of CH_4/air turbulent swirling flames in a cuboid combustor, direct numerical simulations are conducted with two stoichiometric CH_4/H_2/air mixture conditions for swirl number $S = 1.2$. The detailed UCSD kinetic mechanism developed by Petrova and Williams [73] consisting of 57 reactive species and 268 elementary reactions without nitrogen chemistry is reduced to 25 reactive species and 111 elementary reactions by using the path flux analysis (PFA) method [70] for H_2-enriched CH_4/air combustion. The reduced mechanism showed reasonable agreements to the detailed mechanism [73] in comparison of one-dimensional unstrained and strained laminar flame profiles obtained by PREMIX [74] and OPPDIF [75] and ignition delay time by SENKIN [76] for both mixture conditions. Therefore, the reduced mechanism is considered to be accurate enough to predict the reaction

zone profiles of this simulations. The description of the reduced mechanism and comparison with the detailed mechanism are summarized in Chemical mechanism.

Figure 2.1 shows the computational domain which is identical to previously reported H_2/air turbulent swirling flames [24, 59–61]. The dimensions of the combustor $L_x \times L_y \times L_z$ is 15 mm × 10 mm × 10 mm and the number of uniform mesh points in each direction $N_x \times N_y \times N_z$ is 1152 × 768 × 768. The size of uniform mesh point is $\Delta x = 13$ μm which ensures that at least 17 mesh grid points are used to resolve the thermal thickness of the flame (δ_{th}) based on the temperature gradient. The inlet geometry consists of a concentric annulus of which inner and outer diameter is $D_{\text{in}} = 0.6$ mm and $D_{\text{out}} = 2.5$ mm respectively as shown in Fig. 2.2. The combustor wall is inert, no-slip and isothermal at 700 K. The bulk mean axial velocity at the inlet u_x^b is set to be 190 m/s to provide nearly the same calorific input which is determined from the low heating value (LHV) of hydrogen and methane, ($E_{\text{in}} \approx 1.16$ kW) to the previous studies for stoichiometric H_2/air flames [24, 59]. The maximum velocity perturbation intensity u'_{max} is set to be $0.15u_x^b = 28.5$ m/s and corresponding root mean square velocity fluctuation u'_{rms} is 10.5 m/s ($\approx 5.5\%$ of u_x^b) at the inflow boundary.

Two mixture conditions of which volume ratio of CH_4:H_2 is 50:50 (H_2-50%) and 80:20 (H_2-20%) are simulated to clarify the effects of H_2-enrichment on the turbulent swirling flames. The premixed mixtures are preheated to $T_u = 700$ K at atmospheric pressure. The flame properties, laminar flame speed S_L, flame thermal thickness $\delta_{\text{th}} = (T_b - T_u)/|\nabla T|_{\text{max}}$, the maximum heat release rate $\omega_{T,\text{L}}$ and the Zel'dovich thickness $\delta_F = \nu_{\text{u}}/S_L$ for both mixture conditions are listed in Table 2.1. Here, T_b is burnt gas temperature in one-dimensional premixed lamianr flame and α_u, ρ_u, μ_u and ν_u is the thermal diffusivity, density, viscosity and kinematic viscosity of the premixed mixture.

2.4 Effects of mixture conditions on combustion characteristics

To investigate the effects of mixture conditions on the combustion characteristics, temporal evolution of total heat heat release rate in the combustor $\dot{q}$ within the sampled period (3.75 τ_L = 300 μs) for both cases are shown in Fig. 2.4. Here, the total heat release rate in the combustor $\dot{q}$ is calculated as :

$$\dot{q}(t) = \int_v \omega_T(\boldsymbol{x},t)dV \approx \sum_{x=1}^{N} \omega_T(x,y,z,t)\Delta V = \sum_{i}^{N_x}\sum_{j}^{N_y}\sum_{k}^{N_z} \omega_T(i,j,k)\Delta x\Delta y\Delta z. \tag{2.138}$$

$\omega_T(\boldsymbol{x},t)$ denotes the volumetric heat release rate at each discretized point [W/m^3]. Δx, Δy and Δz is the size of uniform mesh grid point, thus, volume element $\Delta V = \Delta x\Delta y\Delta z$. The volumetric heat release rate ω_T is computes as:

$$\omega_T = -\sum_{i}^{N_s} h_i\omega_i. \tag{2.139}$$

In the figure, $\tau_L = L_x/u_x^b$ is defined as the flow through time τ_L and is approximately 80μsec. The sampling period is 3.75τ_L = 300μs and samples are taken at every 2μs. Hence, 150 samples are used for averaged statistics. The average and standard deviation of $\dot{q}$, $\overline{q}$ and σ_q are 1.074 kW and 0.022 kW for H_2-50%, and 0.930 kW and 0.023 kW for H_2-20% respectively. Thus, it can be said that the DNS results are in quasi steady state within the sampling period. It should be noted that the averaged total heat release in the combustor are lower than the calorific input E_{in} = 1.16 kW for both cases, which suggests that the fuels may not be completely consumed in the computational domain. Since $\overline{q}$ for H_2-20% is lower than the value for H_2-50%, it is anticipated that more fuels may remain in the combustor for H_2-20%.

To investigate the combustion characteristics, instantaneous and Favre (density weighted) averaged distributions of reaction progress variable $\widetilde{c_Y}$ in the representative $x-y$ plane ($y \leq 0$, $z = 0$) of the combustor are shown in Fig. 2.5. Here,

the reaction progress variable c_Y is defined by the sum of species mass fraction $Y_s \equiv Y_{H_2} + Y_{H_2O} + Y_{CO} + Y_{CO_2}$ in [77, 78].

$$c_Y \equiv \frac{Y_s - Y_s^u}{Y_s^b - Y_s^u}, \tag{2.140}$$

$$Y_s = Y_{H_2} + Y_{H_2O} + Y_{CO} + Y_{CO_2}. \tag{2.141}$$

In the Eq. (2.140), the superscripts "u" and "b" denote the value in the unburnt and burnt gas side of the corresponding laminar conditions respectively. The values of Y_s^u and Y_s^b for H_2-50% are $(Y_s^u, Y_s^b) = (5.58\times10^{-3}, 0.233)$ and $(Y_s^u, Y_s^b) = (1.63\times10^{-3}, 0.242)$ for H_2-20% respectively. c_Y increases form 0 (reactants side) to 1 (burnt gas side) with progress of reactions in the laminar flames.

As the figures show, the values of c_Y in the inner recirculation zones (IRZ) and outer recirculation zones (ORZ) are relatively similar for H_2-50%, whereas the values in the ORZ are lower than the values IRZ for H_2-20%. This suggests that progression of reaction in the ORZ is slower compared to the one in the IRZ for H_2-20% as anticipated. In the next chapter, differences between the cases are investigated in detail.

2.5 Turbulent combustion conditions

Turbulent combustion conditions from averaged statistics of the present DNS are discussed based on the regime diagram [52]. In the present study, following turbulent statistics and non-dimensional numbers are considered.

- Turbulent kinetic energy

$$\tilde{k} = \frac{1}{2}\widetilde{u_i'' u_i''}. \tag{2.142}$$

- Root mean square of velocity perturbation

$$u'_{\mathrm{rms}} = \left(\frac{2}{3}\tilde{k}\right)^{1/2}. \tag{2.143}$$

- Turbulent strain rate tensor

$$S_{ij} = \frac{1}{2}\left(\frac{\partial u_i^{''}}{\partial x_j} + \frac{\partial u_j^{''}}{\partial x_i}\right). \tag{2.144}$$

- Dissipation rate of turbulent kinetic energy

$$\tilde{\varepsilon} = \frac{\overline{2\nu\rho(S_{ij}S_{ij} - S_{kk}S_{kk}/3)}}{\overline{\rho}}. \tag{2.145}$$

- Integral length scale

$$l_E = \frac{(u'_{\mathrm{rms}})^3}{\tilde{\varepsilon}}. \tag{2.146}$$

- Taylor micro scale

$$\lambda = \frac{1}{3}\sum_{i=1}^{3}\sqrt{\widetilde{u_i^{''2}} \Big/ \left(\widetilde{\frac{\partial u_i^{''}}{\partial x_i}}\right)^2}. \tag{2.147}$$

- Kolmogorov length scale

$$\eta = \left(\frac{\tilde{\nu}^3}{\tilde{\varepsilon}}\right)^{1/4}. \tag{2.148}$$

- Reynolds number based on integral length scale l_E

$$Re_{l_E} = \frac{u'_{\mathrm{rms}} l_E}{\nu}. \tag{2.149}$$

- Reynolds number based on Taylor micro length scale λ

$$Re_{\lambda} = \frac{u'_{\mathrm{rms}} \lambda}{\nu}. \tag{2.150}$$

Here, $\overline{f}$ and $\tilde{f}$ denote the Reynolds average and Favred averaged value of a physical quantity f and computed as follows.

$$\overline{f} = \frac{1}{N_t}\sum_{i=1}^{N_t} f(x, y, z, t_i), \tag{2.151}$$

$$\tilde{f} = \frac{\overline{\rho f}}{\overline{\rho}}, \tag{2.152}$$

where, N_t denotes the number of samples in time and 150 samples are used for the averaged statistics of the flow field. The fluctuations around the mean are expressed as follows.

$$f' = f - \overline{f}, \tag{2.153}$$

$$f'' = f - \tilde{f}. \tag{2.154}$$

Figure 2.6 shows the regime diagram which is constructed base on volume averaged values in the unburnt gas sides of the flow field, where the Favre averaged reaction progress variable $\widetilde{c_Y}$ is $0.1 \leq \widetilde{c_Y} \leq 0.4$ in Figs. 2.5c and d. Several important turbulent statistics are summarized in Table 2.3. In the Table 2.3, the Karlovitz number Ka and Damköhler number Da based on the integral length scale l_E are defined as follows.

$$Ka = \left(\frac{u'}{S_L}\right)^{2/3} \Bigg/ \left(\frac{l_E}{\delta_F}\right)^{1/2}, \tag{2.155}$$

$$Da = \left(\frac{l_E}{\delta_F}\right) \Bigg/ \left(\frac{u'}{S_L}\right). \tag{2.156}$$

As Fig. 2.6 clearly shows, the turbulent combustion conditions of the present study are categorized into the thin reaction zones for both cases. The Karlovitz numbers Ka defined as Eq. (2.156) for the present study are higher than the previously reported studies for pure H_2/air turbulent swirling flames [24, 59–61] which are closer to the boundary of distributed reaction zones. This is due to lower S_L compared with H_2/air flames (10.4 m/s for ϕ = 1.0 and 7.28 m/s for ϕ = 0.6) at the same initial temperature and pressure (T_u = 700 K and p_{ini} = 0.1 MPa). Thus, it is expected that the turbulent motions can disturb the preheat zones of the flame, while the reaction zones may remain thin enough to be regarded as flamelets.

2.6 Conclusions of this chapter

In this chapter, direct numerical simulations of hydrogen-enriched methane/air turbulent swirling premixed flames are conducted with reduced chemical mechanism. Two stoichiometric mixture conditions, of which volume ratio of CH_4:H_2 = 50:50 and CH_4:H_2 = 80:20 are considered. The following conclusions are obtained:

1. For both cases, total heat release rates in the combustor are lower than the calorific input E_{in} = 1.16 kW. The total heat release rates for the H_2-20% is lower than the values of H_2-50% even with almost the identical calorific input is provided.

2. The values reaction progress variable in the inner and outer recirculation zones are relatively similar for H_2-50%, whereas for H_2-20%, the values in the outer recirculation zones are lower compared with the values in the inner recirculation zones.

Table 2.1: Numerical parameters of the present DNS

Case	H_2-50%	H_2-20%
L_x [mm]	15.0	
L_y [mm]	10.0	
L_z [mm]	10.0	
N_x	1152	
N_y	768	
N_z	768	
Δx [μm]	13.03	
Δy [μm]	13.03	
Δz [μm]	13.03	
ϕ	1.0	
T_{pre} [K]	700	
T_{Wall} [K]	700	
p_{ini} [MPa]	0.1	
δ_L [mm]	0.221	0.249
δ_F [mm]	2.66×10^{-2}	3.53×10^{-2}
S_L [m/s]	2.73	1.97
α_u [m^2/s]	1.17×10^{-4}	1.02×10^{-4}
ρ_u [kg/m^3]	0.452	0.472
μ_u [$Pa \cdot s$]	3.29×10^{-5}	3.29×10^{-5}
ν_u [m^2/s]	7.28×10^{-5}	6.96×10^{-5}
$\tau_F = \delta_L/S_L$ [s]	8.10×10^{-5}	12.64×10^{-5}

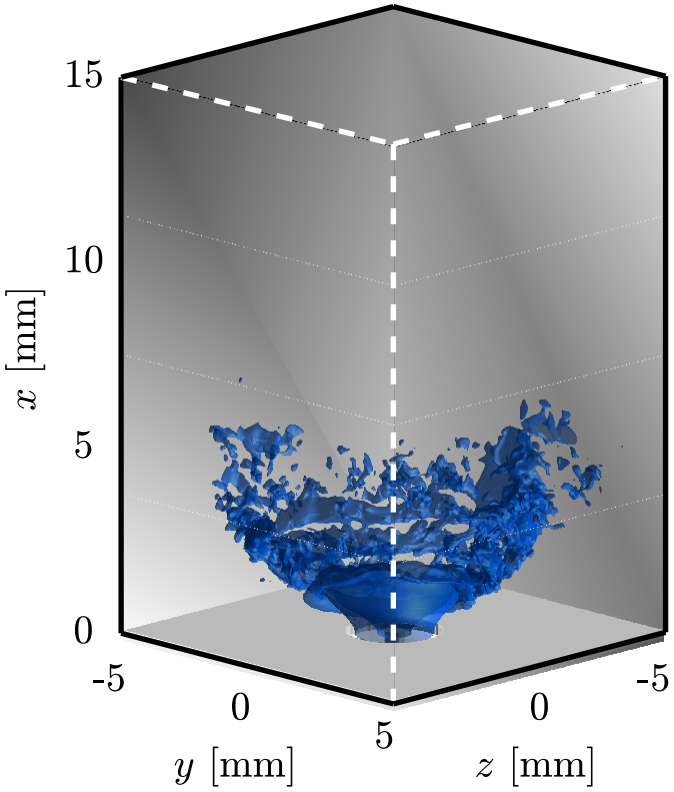


Figure 2.1: Schematic of the computational domain.

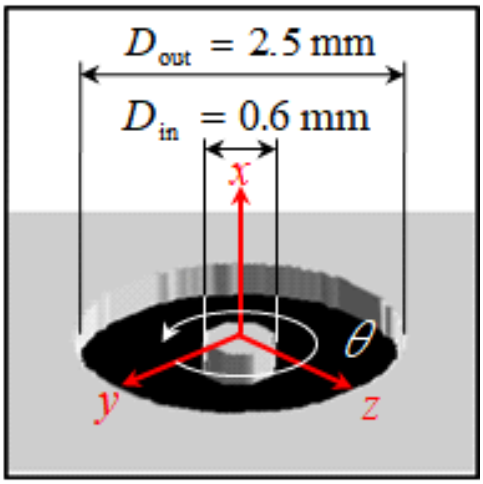


Figure 2.2: Geometry of the inlet boundary.

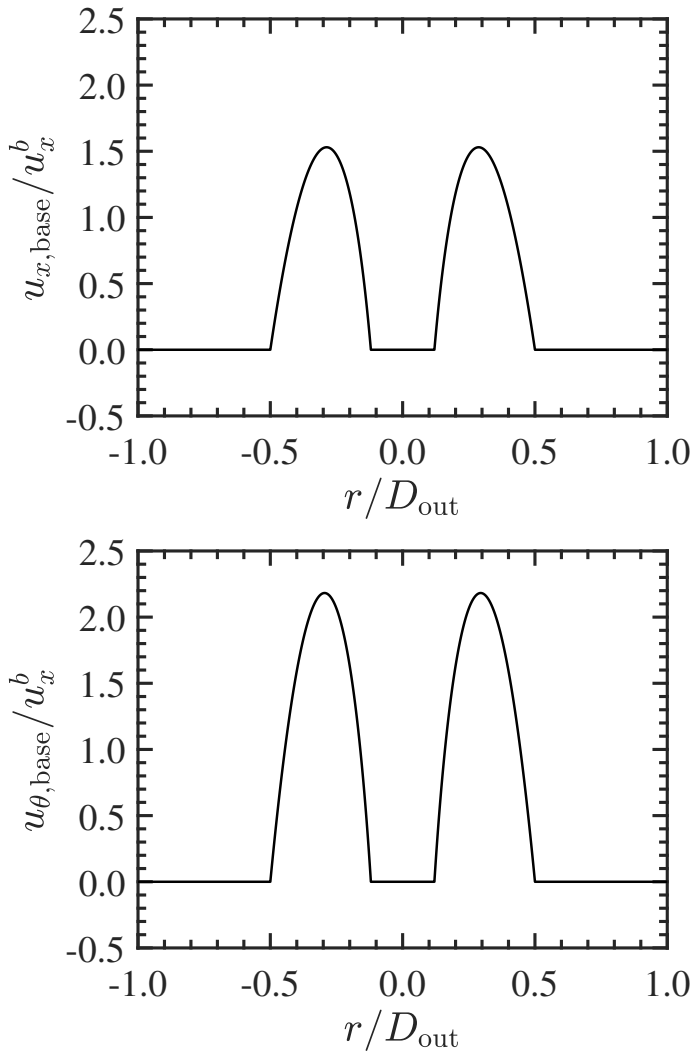


Figure 2.3: Mean velocity profiles of u_x and u_θ at the inlet for S=1.2.

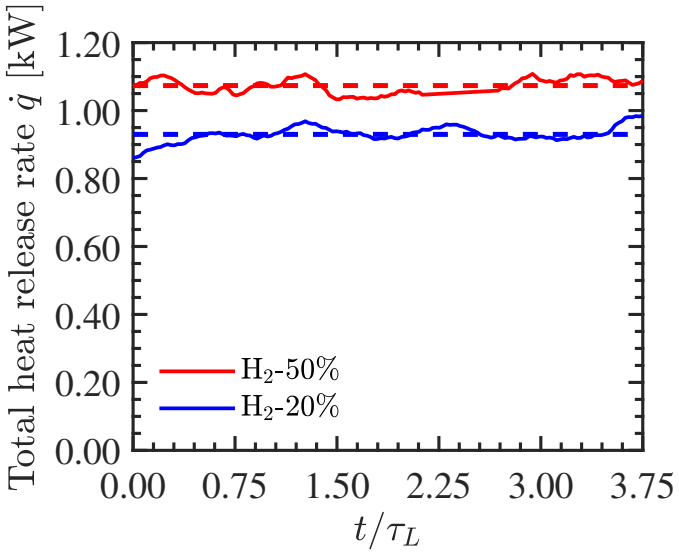


Figure 2.4: Temporal evolution of total heat release rate in the combustor $\dot{q}$ for H_2-50% (red line) and H_2-20% (blue line). The dashed line denotes the averaged value $\overline{q}$ during the sampling period.

Table 2.2: The average and standard deviation of total heat release rate in the combustor $\dot{q}$ within the sampling period, $\overline{q}$ and σ_q for each case.

Case	H_2-50%	H_2-20%
$\overline{q}$ [kW]	1.074	0.930
σ_q [kW]	0.022	0.023

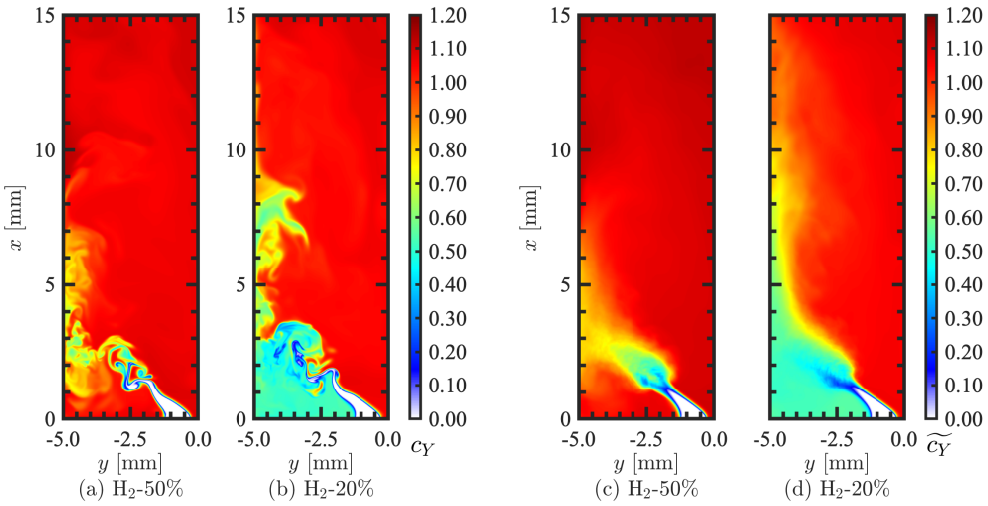


Figure 2.5: 2-dimensional distributions of instantaneous and Favre averaged reaction progress variable c_Y (a,b) and $\widetilde{c_Y}$ (c,d) on the representative $x - y$ plane ($y \leq 0$, $z = 0$).

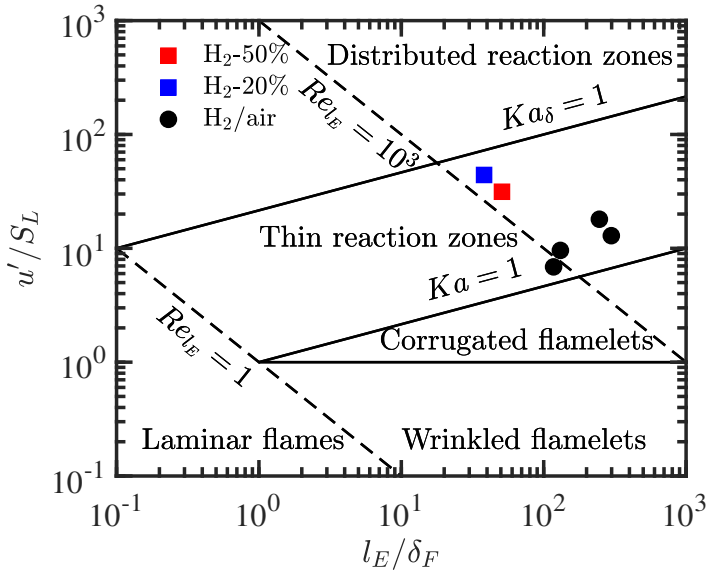


Figure 2.6: Turbulent combustion conditions of the present DNS (red and blue squares) and previously reported H_2-air cases (black circles).

Table 2.3: Numerical parameters of the present DNS based on the turbulent statistics. Re_{l_E}, Ka and Da denote the Reynolds number, Karlovitz number and Damkohler number based on integral length scale l_E.

Case	H_2-50%	H_2-20%
l_E [mm]	1.36	1.35
λ [mm]	0.183	0.166
η [μm]	9.06	8.46
u'_{rms} [m/s]	85.69	86.84
u'/S_L	31.4	44.1
l_E/δ_F	50.9	38.1
Re_{l_E}	1598	1680
Re_λ	215.9	207.5
Da	1.62	0.86
Ka	24.6	47.4

Chapter 3

Effects of hydrogen-enrichment on global flame features

3.1 Preface

In chapter 2, it is suggested that global flame features and reaction characteristics may be different between the cases form temporal variations of the total heat release rate in the combustor and distributions of reaction progress variables. Flame shapes and reaction zone characteristics affect flame stabilization thermal efficiency substantially. Therefore, clarifying global flame features and reaction zone characteristics are important in designing of gas turbine combustor.

Experimental studies of H_2/CH_4 swirling flames mainly focused on the flame shapes and emission characteristics under various conditions. Cheng et al. [43] have demonstrated influences of H_2 volume fraction and pressure on the flame shapes and flame attachment characteristics in a laboratory scale low-swirl burner. Kim et al. [44, 45] have investigated the effects of fuel composition and swirl strength on the flame shapes, CO and NO_x emission characteristics of premixed swirling flames. Shanbhogue et al. [37] have reported effects of H_2 enrichment and equivalence ratios on transition of flame shapes and flame stabilization mechanism. However, detailed reaction zone and species transport characteristics of the flames under intense turbulence, which are not able to be obtained by experimental studies are not clarified yet.

There are several numerical studies provided findings of flame structure and flow-flame interactions in weakly or moderately turbulent premixed swirling flames of CH_4/air [48, 49], CH_4/H_2/air [50] and $CH_4/O_2/CO_2$ [51] by conducting large eddy simulations (LES). Huang and Yang [48] reported that mixture temperature and equivalence ratio are two most important parameter affecting structure and stability of swirl-stabilized flames. Huang and Yang [49] investigated effect of swirl strength on flame length and occurrence of flame flash back. Mercier et al. [50] have studied flame shape transition between two H_2 enrichment levels in both experimental and numerically. The numerical result could capture the flame shape transition observed in their experiments when considering the non-adiabaticity of combustor walls. Chakroun et al. [51] also suggested that the impact of heat loss by the combustor walls on the flamelet structures in oxy-flames. However, effects of mixture conditions on reaction zone structures and species transport characteristics in the turbulent swirling flames affected by intense turbulence, which are necessary information for turbulent combustion modeling and designing practical H_2-enriched gas turbine engines, have not been fully clarified yet. Since all of the scales involved in the phenomena can not be fully resolved due to limitations of turbulence and combustion models.

In this chapter, the effects of hydrogen enrichment on global flame features and reaction zone characteristics are investigated. First, effects of hydrogen enrichment on the global flame features, distributions of temperature, heat release rate, species mass fraction and reaction rate are examined. Next, conditional means of DNS data are compared with unstrained and strained laminar flames to clarify the reaction characteristics of turbulent swirling premixed flames. For the last, balance between convection, diffusion and chemical reaction terms of an instantaneous species conservation equation are considered to find out which terms affect the flame structures.

3.2 Effects of hydrogen ratios on the global flame features

Figure 3.1 shows volume rendering of normalized heat release rate ω_T^+ and the second invariant of velocity gradient tensor Q^* at an instance. The heat release rate ω_T is calculated by Eq. (2.139). ω_T is normalized by the maximum heat release rate of the corresponding unstrained laminar flame $\omega_{T,\mathrm{L}}$, $\omega_T^+ = \omega_T/\omega_{T,\mathrm{L}}$. The second invariant of velocity gradient tensor Q is calculated as:

$$Q = \frac{1}{2}\left(-S_{ij}S_{ij} + W_{ij}W_{ij}\right), \tag{3.1}$$

$$S_{ij} = \frac{1}{2}\left(\frac{\partial u_i}{\partial x_j} + \frac{\partial u_j}{\partial x_i}\right), \tag{3.2}$$

$$W_{ij} = \frac{1}{2}\left(\frac{\partial u_i}{\partial x_j} - \frac{\partial u_j}{\partial x_i}\right). \tag{3.3}$$

Here, S_{ij} and W_{ij} denote symmetric and antisymmetric parts of the velocity graident tensor. The threshold of iso-sufrace Q^* is 1% of its maximum. For both cases, large-scale and an aggregation of fine-scale vortical structures are formed in the near field of inflow boundary due to the strong shear layer and rapid development of turbulence. However, the shapes of ω_T^+ fields seem to be different between the cases.

To figure out the difference in detail, instantaneous and Favre-averaged 2-dimensional distributions of temperature T and instantaneous and time-averaged heat release rate ω_T^+ on the representative plane ($y \leq 0$ and $z = 0$) are shown in Figs. 3.2 and 3.3. In this study, the region of $x \leq L_x/2 = 7.5$ mm is named as a “upstream region" and $x > L_x/2$ is named as a “downstream region" of the combustor. For both cases, the inner recirculation zones (IRZ), where heat and combustion products are recirculated by the swirling flows are formed in the central part of the plane ($y \geq -2.5$ mm). Due to the existence of combustor walls, the outer recirculation zones (ORZ) are observed at the corner of the plane ($y \leq -2.5$

and $x \leq 2.5$ mm). We refer the shear layer formed between the annular jets and IRZ as inner shear layer (ISL) and the shear layer between the annular jets and ORZ as outer shear layer (OSL).

Similar to the previous studies [24, 59–61], ω_T^+ is decreased compared to $\omega_{T,\mathrm{L}}$ for both cases. Temperature in the ORZ is lower compared to the value in the IRZ possibly due to heat loss by contacting with isothermal walls. For H_2-50%, relatively high ω_T^+ is observed in the near field of swirling jets and combustor walls in the upstream region, whereas for H_2-20%, the region of high ω_T^+ exists both in the upstream and downstream regions. These differences in flame length are due to increase of reactivity and diffusivity with the increase of H_2-ratios. Focusing on the near field of swirling jets, the magnitudes of ω_T^+ in the ISL and OSL are relatively similar for H_2-50%. For H_2-20%, however, higher ω_T^+ is observed in the ISL rather than OSL. In other words, the flame is stabilized in both shear layers for H_2-50%, whereas the flame extinction occurs in the OSL for H_2-20%. Thus, it is anticipated that the fresh reactants may flow through the OSL almost unreacted due to the flame extinction. As a result, the temperatures in the region from the OSL to the combustor walls become lower than H_2-50% due to entrainment of cold reactants into to OSL. These different flame shapes between the cases are qualitatively similar to experimental and numerical results of pure CH_4 and CH_4/H_2 swirling flames under the mixture conditions with lower H_2-ratios in previous studies [15, 30, 37, 43, 50, 79], which is attribute to reduced reactivity (or lower OH concentration) in the ORZ or extinction in the OSL. To investigate the reaction zone characteristics further, 2-dimensional distributions of fuel species mass fraction and reaction rates are examined next.

Figures 3.4 and 3.5 show instantaneous and time-avergaed 2-dimensional distributions of fuel species mass fraction Y_i^*. For fuel species and oxygen, the superscript "$*$" denotes the normalization by the value at the inflow boundary Y_i^u, thus $Y_i^* \equiv Y_i/Y_i^u$. For H_2-50%, CH_4 is almost consumed in the upstream region (Figs. 3.4a and 3.5a), while the values of $Y_{\mathrm{H_2}}^*$ are approximately 0.2 in the ORZ and downstream region (Figs. 3.4c and 3.5c) which indicates that leakage of H_2

into the burnt gas due to high temperature equilibrium in [80] is also observed for stoichiometric CH_4/H_2/air mixture conditions. For H_2-20%, however, CH_4 is not completely consumed in the region from the near field of OSL to the downstream (Figs. 3.4b and 3.5b). Especially, the value of $Y^*_{H_2}$ is as high as or higher than unity in the region aforementioned (Figs. 3.4d and 3.5d). Thus, these different mass fraction distributions seem to be related to extinction in the OSL and ORZ in Figs. 3.2d and 3.3d and/or production and consumption of H_2.

To clarify the behaviors of the fuels in detail, instantaneous and time averaged fuel species reaction rate contours are shown in Figs. 3.6 and 3.7. The reaction rates are normalized as $\omega^+_i = \omega_i/\omega_{i,\mathrm{L}}$, where $\omega_{i,\mathrm{L}}$ is the maximum of $|\omega_i|$ in the corresponding unstrained laminar condition. Production and consumption reaction rates are colored by red and blue, respectively. The magnitudes of the fuel species reaction rates are decreased compared to the $\omega_{i,\mathrm{L}}$, which is similar to the previous studies with same swirl number condition [24, 59–61]. For both cases, consumption of CH_4 is observed in the reaction rate contours (Figs. 3.6a, c and 3.7a, c). For H_2-20%, the magnitudes of $\omega^+_{CH_4}$ are noticeably reduced in the near field of OSL and in the ORZ.

As for $\omega^+_{H_2}$, both consumption and production reactions are observed, while the tendencies are distinctively different between the cases. For H_2-50%, consumption of H_2 is dominant in the upstream region and production reaction is observed in the reactants sides of the flame with relatively lower magnitude (Figs. 3.6b and 3.7b). For H_2-20%, consumption of H_2 (Figs. 3.6d and 3.7d) occurs in trailing edge of the flame with relatively high magnitude and production does in the unburnt side of the reaction zones with relatively similar magnitude of the consumption reaction. This suggests that the role of H_2 in each mixture condition, which is reported in [41, 42] remains unchanged even in strong turbulence. In the near field of OSL and ORZ, the magnitudes of $\omega^+_{H_2}$ are decreased substantially. Furthermore, as Fig. 3.8 shows, the values of $Y^*_{O_2}$ remain high in the OSL and ORZ ($Y^*_{O_2} \approx 0.6$) and the reaction rates are also decreased substantially in the region aforementioned.

Therefore, the high $Y^*_{H_2}$ values for H_2-20% in Figs. 3.4d and 3.5d even with

relatively high values of $Y^*_{O_2}$ in Fig. 3.8b may be due to production of H_2 in the unburnt side of the reaction zones and leakage of fuels to the ORZ resulted from the extinction in the OSL. In addition, comparably lower reaction rates of fuels and oxygen (Fig. 3.6 - Fig. 3.8) and temperature in the ORZ seem to be attributed to heat loss by cold reactants flow through the OSL as anticipated in Figs. 3.2d and 3.3d. As a result, normalized mass fraction and reaction rate of of product species H_2O (Fig. 3.9) and CO_2 (Fig. 3.10), which correspond to large amount of heat release rate, become lower as the reactions occur slower in the ORZ for H_2-20%.

Figures 3.11, 3.12 and 3.13 show 2-dimensional distributions of mass fraction and reaction rates of radical species, H, O and OH respectively. The superscript "$*$" denotes that species mass fraction is normalization by the maximum value in the corresponding laminar flame, $Y_{i,L}$, thus $Y^*_i \equiv Y_i/Y_{i,L}$. The superscript "+", again denotes the normalized reaction rate by $\omega_{i,L}$ the maximum of $|\omega_i|$ in the corresponding laminar flame.

Similar to the unstrained laminar flames, consumption of radical species occur in the leading edge of the flame and production of radicals occur in the tailing edge of the flame. While the normalized mass fraction and reaction rate of radical species are lower for both cases over all. This correlates to relatively lower heat release rates compared to the corresponding unstrained laminar flame, because elemental reactions involving radical species (chain-terminating reactions) occur in high temperature region and yield relatively higher heat release rate. Thus, temperature and heat release rate in the ISL and IRZ are relatively higher than the values in the OSL and ORZ. For H_2-50%, the values of normalized radical species mass fraction and reaction rate are small but non-negligible in the ORZ, because fuel species are consumed rapidly in the upstream. For H_2-20%, however, mass fraction and reaction rates in the ORZ are substantially decreased and the values are negligibly small. Since radical species are essential for chain initiation reactions, it is also considered to be related to extinction in the OSL and ORZ.

Figures 3.14 to 3.17 show mass fraction and reaction rates of intermediate species, CH_3, CH_2O, CHO and CO. These species belong to C_1 route which are

produced sequentially from decomposition of CH_4. As for CH_3 and CH_2O, the values in the OSL and ORZ for H_2-50% are relatively low, which is attributed to rapid consumption of CH_4 and the subsequent species reacting with radicals recirculated. For H_2-20%, however, CH_3 and CH_2O remain in the OSL and ORZ possibly due to lack of radical species as shown in previous figures. Furthermore, the values of $Y^*_{CH_2O}$ which correspond to preheat zones are higher in the ORZ due to active production in the ORZ (Fig. **??**d). In the near field of inflow boundary, reaction rates of CH_3 and CH_2O in the ISL and OSL are relatively similar for H_2-50%. Whereas the values in the OSL are negligibly low for H_2-20%, which indicates slow progress of reactions due to extinction in the OSL.

Hence, mass fraction and reaction rate of HCO and CO in the upstream are relatively high for H_2-50% with progress of subsequent elemental reactions. As a result, the heat release rate in the upstream region become relatively higher. While for H_2-20%, mass fraction and reaction rates of the species are negligibly small in the ORZ due to extinction, while the values in the down stream are relatively high reacting with recirculated burnt gases. Therefore, relatively high heat release rates are observed in the down stream.

Overall, the distributions of radical species indicate increase of radical pools with increase of H_2-ratios which is qualitatively similar to the studies in [41, 42]. In addition, the distributions of intermediate species also suggest enhancement of elemental reactions in C_1 route with increased amount of H_2 in the premixed mixture similar to the previous studies [41, 42].

3.3 Effects of hydrogen ratios and local tangential strain rate on the reaction zone characteristics

To evaluate the effects of H_2-ratios and local tangential strain rates on the reaction zone characteristics observed in Sec. 3.2, the conditional average of a variable q conditioned based upon c_Y, which is denoted as $\langle q|c_Y\rangle$ is compared with unstrained and strained laminar flames. Here, q is fuel species mass fraction

or reaction rate in this study. In the laminar flames, c_Y is 0 in the reactants side and 1 in the burnt gas side, while c_Y can be larger than unity in the turbulent flames possibly due to turbulent motions. In the process of conditional averaging, the DNS data within approximately δ_{th} from the wall are excluded due to cooling effect by the isothermal walls.

In the strained laminar flame simulations, a single flame configuration between fresh reactants and hot products as shown in Fig. 3.18 which was adopted as in [81–83] is considered to predict the reaction zone characteristics in strong shear layers generated by the turbulent swirling flows by using OPPDIF [75]. In the single flame configuration, flame can be sustained at a much higher strain rate than the extinction strain rate in twin flames configuration [37]. The thermochemical conditions at the fuel side are fresh reactants (Y_i^u, T_u) and the oxidizer side are burnt gases (Y_i^b, T_b) of the corresponding unstrained laminar flame. The jet velocity U_{j} at the fuel and oxidizer side is set to be same. The local tangential strain rate a_t is defined to be the first peak of velocity gradient $-du/dx$ in the reactants side. The values of a_t considered in this study are 1/50 to 2 times of the mean strain rate in the preheat zones of the present DNS results which is estimated as $u'_{\text{rms}}/\lambda \approx 5.0 \times 10^5$ s^{-1}. Here, u'_{rms} is the velocity fluctuation computed by Eq. (2.143) λ is the Taylor microscale computed by Eq. (2.147). The values are volume averaged within $0.1 \leq \widetilde{c_Y} \leq 0.4$ of the flow field. The value of λ is 0.183 mm for H_2-50% and 0.166 mm for H_2-20%.

Figures 3.20 and 3.21 show profiles of $Y^*_{\text{CH}_4}$ and $Y^*_{\text{H}_2}$ in phase space. As Fig. 3.20 shows, no significant difference between the mixture conditions is observed in the $Y^*_{\text{CH}_4}$ profiles. All of the $Y^*_{\text{CH}_4}$ profiles decrease to nearly 0 monotonically with the increase of c_Y. The responses of $Y^*_{\text{CH}_4}$ to the tangential strain rate a_t are similar for both mixture conditions. The strained laminar flame values increase gradually with the increase of a_t, which suggests decreased consumption of CH_4 and increased influences of relevant transport terms (convection and diffusion) which can modify the mixture composition in the reaction zones. The values of $\langle Y^*_{\text{CH}_4} | c_Y \rangle$ are relatively higher than the unstrained and strained laminar values in

the entire c_Y. This behavior is different from the profiles in high Karlovitz number turubulent planar CH_4/air flames [53, 84], where the CH_4 concentration profiles lie along the corresponding laminar profiles. This deviation is rather similar to the profiles in [51], where the flame is affected by heat loss through the combustor wall. Hence, the deviation of $\langle Y^*_{CH_4}|c_Y\rangle$ form the corresponding laminar profiles may be due to the decreased consumption of CH_4 as shown in Fig. 3.6 and/or increased influences of the relevant transport terms.

As for the $Y^*_{H_2}$ profiles, substantial differences are observed between Figs. 3.21a and b. Opposite to the responses of $Y^*_{CH_4}$ to the a_t, $Y^*_{H_2}$ profiles decrease gradually with the increase of a_t for both mixture conditions. The strained laminar profiles for H_2-20% mixture condition decrease substantially with the increase of a_t, whereas the profiles are relatively similar for H_2-50% mixture condition. The $\langle Y^*_{H_2}|c_Y\rangle$ profile for H_2-50% shows relatively similar behaviors to both unstrained and strained laminar profiles in an average sense. For H_2-20%, $\langle Y^*_{H_2}|c_Y\rangle$ deviates from the laminar flames in the unburnt gas side except for $a_t = 2.0 \times 10^5$ s^{-1}. Thus, $\langle Y^*_{H_2}|c_Y\rangle$ values as high as unity in the unburnt sides as observed in Fig. 3.4d seem to be due to decreased reaction rates (extinction) and/or convection by the swirling jets.

To show the responses of Y^*_i to a_t in detail, the fuel species reaction rates ω^+_i are evaluated by the same manners in Figs. 3.22 and 3.23. For both mixture conditions, the $\omega^+_{CH_4}$ profiles for strained laminar flames in which $a_t \leq 1.0 \times 10^5$ s^{-1} are relatively similar to the unstrained laminar flames. With further increase of a_t ($a_t \geq 2.0 \times 10^5$ s^{-1}), consumption rates increase gradually. This suggests the increased contributions by convection and diffusion, which are in balance with chemical reaction. The increase of relevant transports with the increase of a_t in the strained laminar flames is mainly due to higher jet velocities which result in narrower reaction zone width and large species mass fraction gradient. While for the turbulent swirling flames, the values of $\langle \omega^+_{CH_4}|c_Y\rangle$ are decreased substantially and deviate from the laminar profiles unlike the $\langle Y^*_{CH_4}|c_Y\rangle$ profiles in Fig. 3.20 due to increased volume fraction of the burnt gases.

As for $\omega^+_{H_2}$, the strained laminar flames show different responses to the a_t between the mixture conditions in Fig. 3.23. For H_2-50% mixture condition, the maximum consumption rates of the strained flames ($a_t \leq 2.0 \times 10^5$ s^{-1}) are decreased. In addition, consumption reaction begins to occur at a relatively higher value of c_Y. With further increase of the a_t ($a_t \geq 5.0 \times 10^5$ s^{-1}), the $\omega^+_{H_2}$ profiles deviate from the unstrained and strained laminar flames with the lower values of a_t ($a_t \leq 2.0 \times 10^5$ s^{-1}). For H_2-20% mixture condition, the maximum production rate increases with the increase of a_t within $a_t \leq 5.0 \times 10^5$ s^{-1}. On the other hand, the peaks of consumption reaction rate appear at similar c_Y and the values are relatively similar except for $a_t = 1.0 \times 10^4$ s^{-1}. In the swirling flames, $\langle \omega^+_{H_2} | c_Y \rangle$ profile for H_2-50% deviates from the laminar profiles. For H_2-20%, $\langle \omega^+_{H_2} | c_Y \rangle$ deviates from the laminar profiles in the unburnt side, while it is relatively similar to the laminar profiles in the burnt gas side. This is also due to increased volume volume fraction of burnt gases as considered for $\langle \omega^+_{CH_4} | c_Y \rangle$.

The comparison of DNS results with the unstrained and strained laminar flames shows that the H_2 mass fraction for H_2-20% and all of the species reaction rates for both cases deviate from the unstrained and strained laminar profiles substantially unlike in high Karlovitz number turbulent planar CH_4/air flames [84, 85]. These results suggest that it is not sufficient to clarify the reaction zone characteristics of the turbulent swirling flames properly simply considering the effects of local tangential strain rates.

3.4 Effects of hydrogen ratios on balance between convection, diffusion and chemical reaction

To investigate the balance between convection, diffusion and chemical reaction in the reaction zone, the contributions in an instantaneous species conservation equation are evaluated [86]. An instantaneous conservation equation for species

mass fraction Y_i is expressed as

$$\rho\frac{\partial Y_i}{\partial t} = \underbrace{-\rho u_k\frac{\partial Y_i}{\partial x_k}}_{C_i} + \underbrace{\frac{\partial}{\partial x_k}(\rho D_i\frac{\partial Y_i}{\partial x_k})}_{\mathcal{D}_i} + \underbrace{\rho\omega_i}_{\mathcal{R}_i} . \tag{3.4}$$

C_i, $\mathcal{D}_i$ and $\mathcal{R}_i$ denote the contributions by convection, diffusion and chemical reaction respectively. Here, ρ [kg/m^3] is density, u_k [m/s] is the velocity in direction k, D_i [m^2/s] is molecular diffusivity and ω_i [1/s] is reaction rate.

Figures **??** and **??** show the conditionally averaged distributions of convection, diffusion and chemical reaction for Y_{CH_4} and Y_{H_2}. The superscript "+" denotes that the values are normalized by the maximum of $|\rho\omega_i|$ in the corresponding unstrained laminar flame to quantify the influences between convection, diffusion and chemical reaction. For both cases, the conditional means of contributions by convection $\langle C_i^+|c_Y\rangle$ and diffusion $\langle \mathcal{D}_i^+|c_Y\rangle$ for Y_{CH_4} and Y_{H_2} are greater than the corresponding laminar values on average in the unburnt side. The peaks appear at relatively lower c_Y and the standard deviations of convection terms are substantially large mainly due to large velocity and its fluctuations. In the burnt side ($c_Y > 0.6$) the magnitudes of $\langle C_i^+|c_Y\rangle$ and $\langle \mathcal{D}_i^+|c_Y\rangle$ become negligibly small. This is attributed to reduced magnitudes of species mass fraction gradients $\partial Y_i/\partial x_k$ as it can be referred from Fig. 3.4, because the convective and diffusive transports are driven by $\partial Y_i/\partial x_k$. The contributions by chemical reaction $\langle \mathcal{R}_i^+|c_Y\rangle$ are smaller than the unstrained laminar flame values, which correspond to the decreased reaction rates observed in Figs. 3.6, 3.22 and 3.23. The peaks appear at relatively higher values c_Y, which is attributed to reactions with the burnt gases recirculated. These results suggest that the contributions by convection and diffusion are more influential on the local and global flame structures of the present DNS. The influences appear strongly in the unburnt side and the profiles deviate from the laminar profiles mainly due to turbulent swirling jets. Comparison between the cases suggests that the contributions by each term for Y_{CH_4} are relatively similar as Fig. 3.24 shows. This indicates that the effects of mixture conditions do not seem to be substantial on the contributions of species conservation equation terms for Y_{CH_4}. Therefore,

the relatively similar behaviors of $\langle Y^*_{CH_4}|c_Y\rangle$ and higher values than the unstrained laminar values in Fig. 3.20 are due to the decreased contribution by reaction and increased contributions by convection and diffusion in the unburnt gas side by the swirling jets.

However, the contributions by each term for Y_{H_2} are different between the mixture conditions as observed in Fig. 3.25. For H_2-50%, conditionally averaged contributions by convection $\langle C^+_{H_2}|c_Y\rangle$ and diffusion $\langle \mathcal{D}^+_{H_2}|c_Y\rangle$ show relatively similar tendencies to those of CH_4, because the fuel species are consumed rapidly in the upstream region. The values of $\langle C^+_{H_2}|c_Y\rangle$ and $\langle C^+_{CH_4}|c_Y\rangle$ are relatively similar in an average sense. Due to larger diffusivity of H_2 than the one of CH_4, the values of $\langle \mathcal{D}^+_{H_2}|c_Y\rangle$ are relatively larger than $\langle \mathcal{D}^+_{CH_4}|c_Y\rangle$. For H_2-20%, the magnitudes of $\langle C^+_{H_2}|c_Y\rangle$ and $\langle \mathcal{D}^+_{H_2}|c_Y\rangle$ are smaller than those of CH_4. This is mainly attributed to smaller magnitudes of $\partial Y_{H_2}/\partial x_k$ than $\partial Y_{CH_4}/\partial x_k$ in the unburnt side as it can be referred from Figs. 3.4b and d, which yield smaller contributions by convection and diffusion of H_2 than those of CH_4. In addition, it is also of interest that $\langle C^+_{H_2}|c_Y\rangle$ and $\langle \mathcal{D}^+_{H_2}|c_Y\rangle$ for H_2-20% contribute in opposite sign to those of the corresponding laminar conditions in the unburnt sides. Therefore, the deviation of $\langle Y^*_{H_2}|c_Y\rangle$ from the laminar flame profiles for H_2-20% is attributed to convective transport by the swirling jets resulted from the decreased reaction rates in the near field of OSL and ORZ in addition to active production of H_2 in the down stream region.

3.5 Conclusions of this chapter

In this chapter, effects of hydrogen ratios on the global flame features and reaction zone characteristics of hydrogen-enriched CH_4/air turbulent swirling premixed flames are investigated. The investigation is conducted by visual examinations of global flame features, comparison of of DNS data with unstrained and strained laminar flames and balance between convection, diffusion and chemical reaction terms. The following conclusions are obtained.

1. For both cases, reaction rates are decreased compared to the corresponding laminar value. However, the global flame features and reaction zone characteristics between the cases are qualitatively different. For H_2-50%, the flame is stabilized in both shear layers, whereas for H_2-20%, extinction occurs in the outer shear layers and H_2 remain almost unreacted in the outer shear layer and recirculation zones.

2. Comparison of reaction zone characteristics in phase space showed deviation from the laminar profiles in H_2 mass fraction for H_2-20% case and all of the fuel species reaction rates. These suggest that considering the effect of local tangential strain rate is insufficient to clarify the reaction zone characteristics of the present DNS.

3. In the analysis of fuel species conservation equation, convection and diffusion of H_2 for H_2-20% are smaller than those of H_2-50% due to smaller H_2 mass fraction gradients resulted from the decreased consumption rates in the region from the outer shear layers to the downstream.

4. The qualitatively different global flame features and reaction zone characteristics between the cases are due to different role of H_2 in each mixture condition and differently decreased fuel species reaction rates in the outer shear layers.

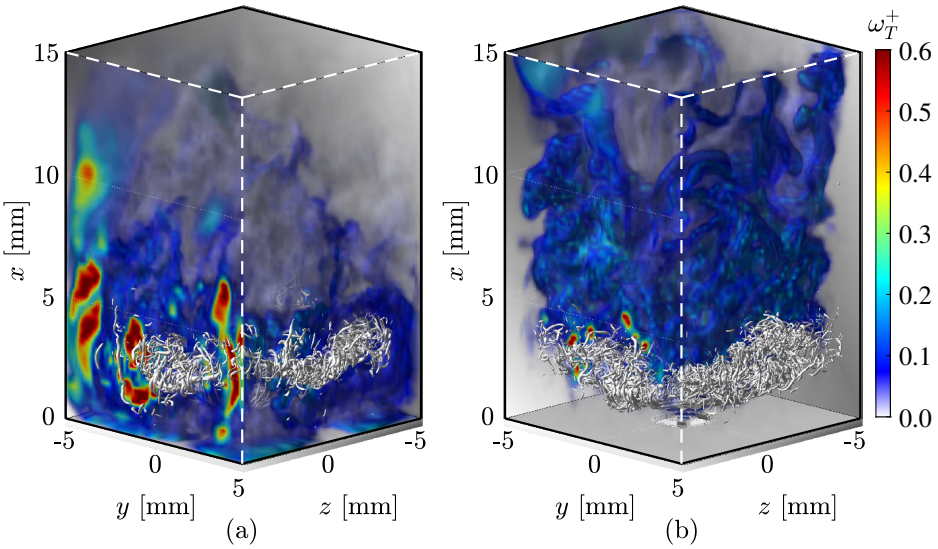


Figure 3.1: Volume rendered normalized heat release rate ω_T^+ and iso-surface of the second invariant of velocity gradient tensor $Q^* = 0.01Q_{\max}$ (white) at an instance for H_2-50% (a) and H_2-20% (b).

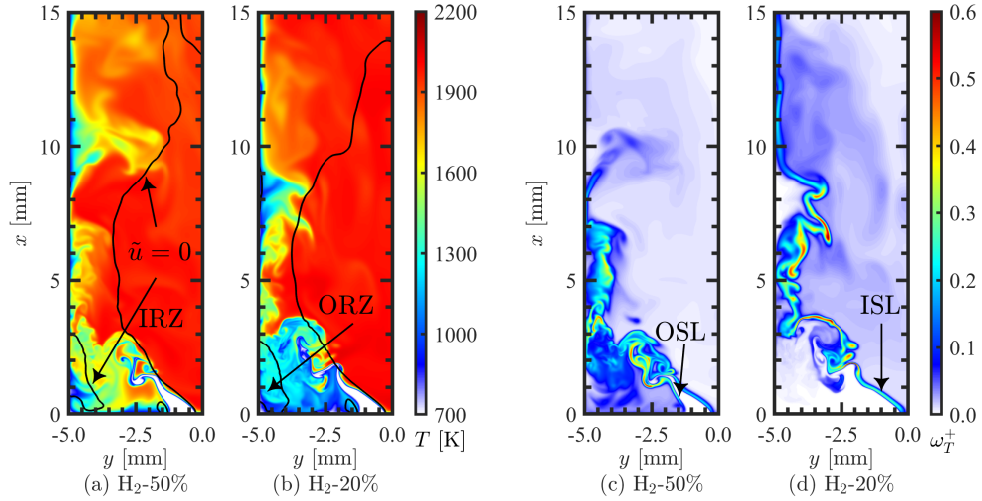


Figure 3.2: Distributions of temperature T (a, b) and heat release rate ω_T^+ (c, d) on the representative $x - y$ plane ($y \leq 0$, $z = 0$).

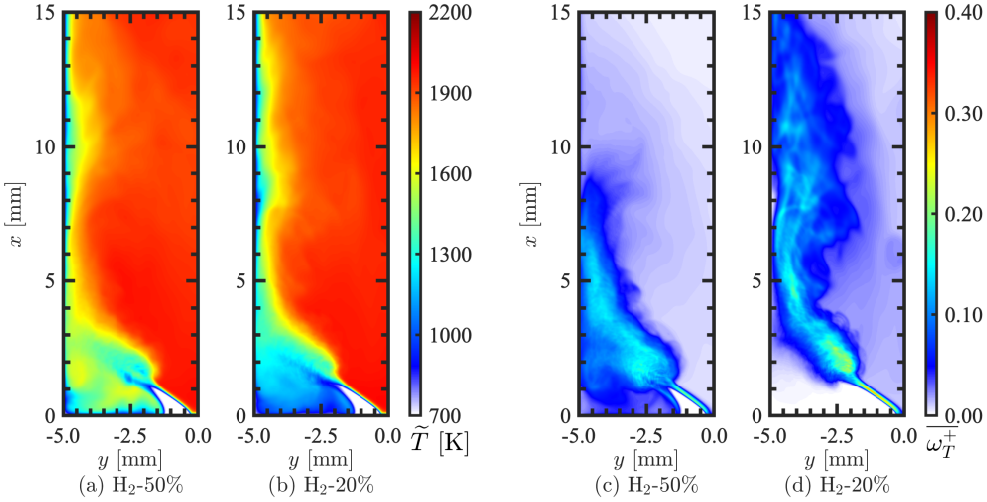


Figure 3.3: Distributions of Favre averaged temperature $\widetilde{T}$ (a, b) and time averaged heat release rate $\overline{\omega_T^+}$ (c, d) on the representative $x - y$ plane ($y \leq 0$, $z = 0$).

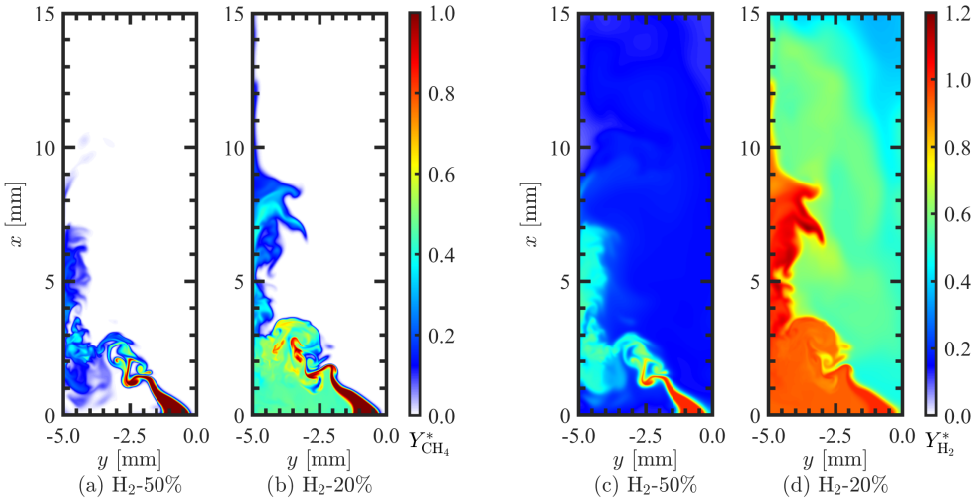


Figure 3.4: Distributions of $Y^*_{CH_4}$ (a, b) and $Y^*_{H_2}$ (c, d) on the representative $x-y$ plane ($y \leq 0$, $z = 0$).

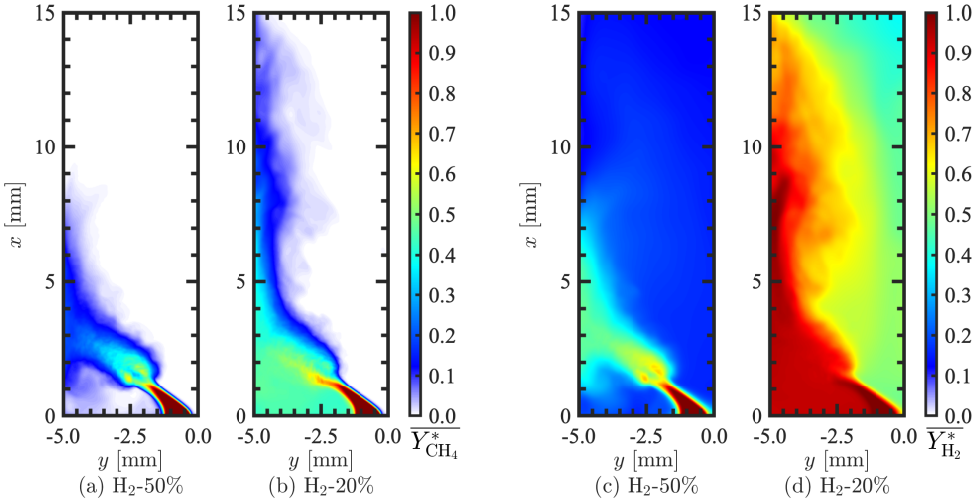


Figure 3.5: Distributions of time averaged CH_4 mass fraction, $\overline{Y^*_{CH_4}}$ (a, b) and H_2 mass fraction, $\overline{Y^*_{H_2}}$ (c, d) on the representative $x-y$ plane ($y \leq 0$, $z = 0$).

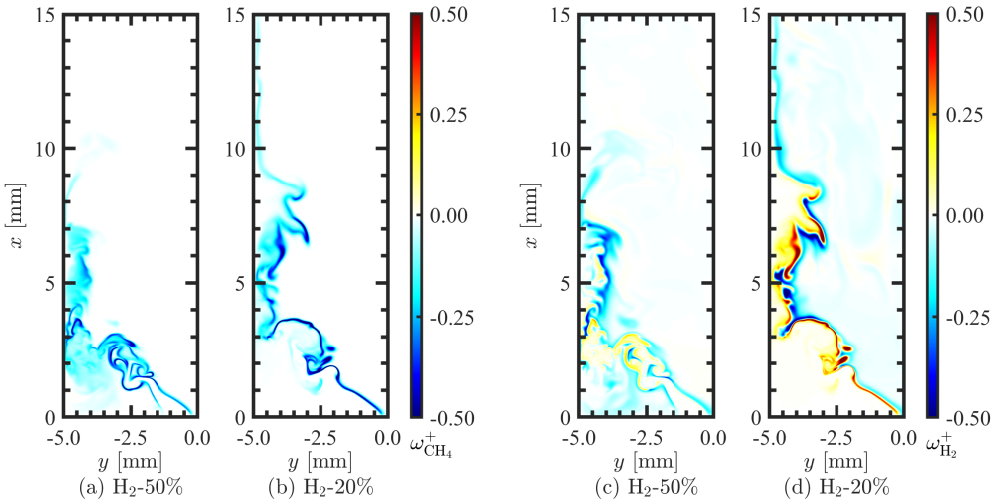


Figure 3.6: Distributions of $\omega^+_{CH_4}$ (a, b) and $\omega^+_{H_2}$ (c, d) on the representative $x-y$ plane ($y \leq 0$, $z = 0$).

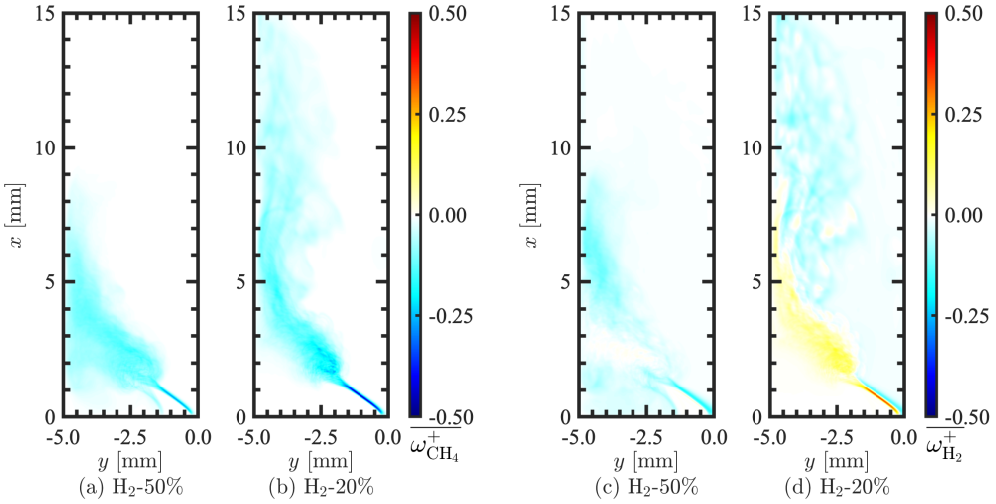


Figure 3.7: Distributions of time averaged reaction rate of CH_4, $\overline{\omega^+_{CH_4}}$ (a, b) and time averaged reaction rate of H_2, $\overline{\omega^+_{H_2}}$ (c, d) on the representative $x-y$ plane ($y \leq 0$, $z = 0$).

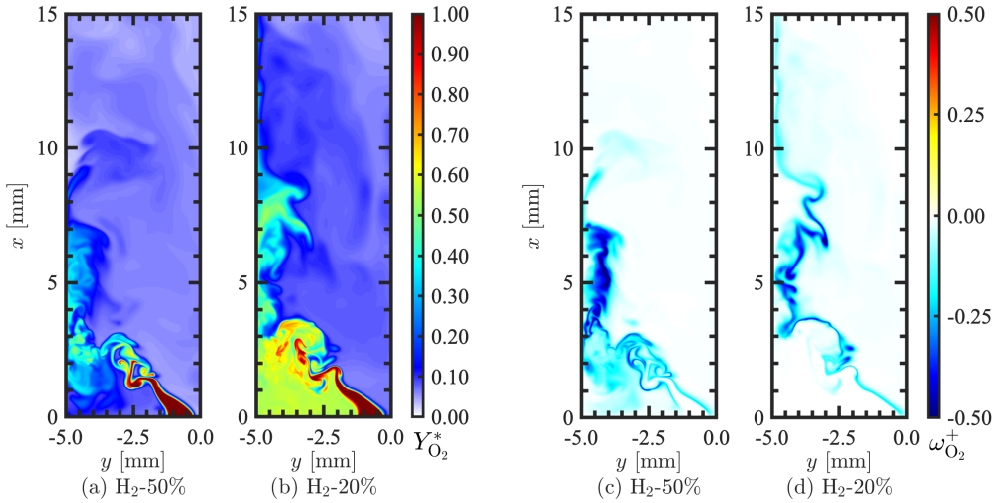


Figure 3.8: Distributions of $Y^*_{O_2}$ (a, b) and $\omega^+_{O_2}$ (c, d) on the representative $x-y$ plane ($y \leq 0$, $z = 0$).

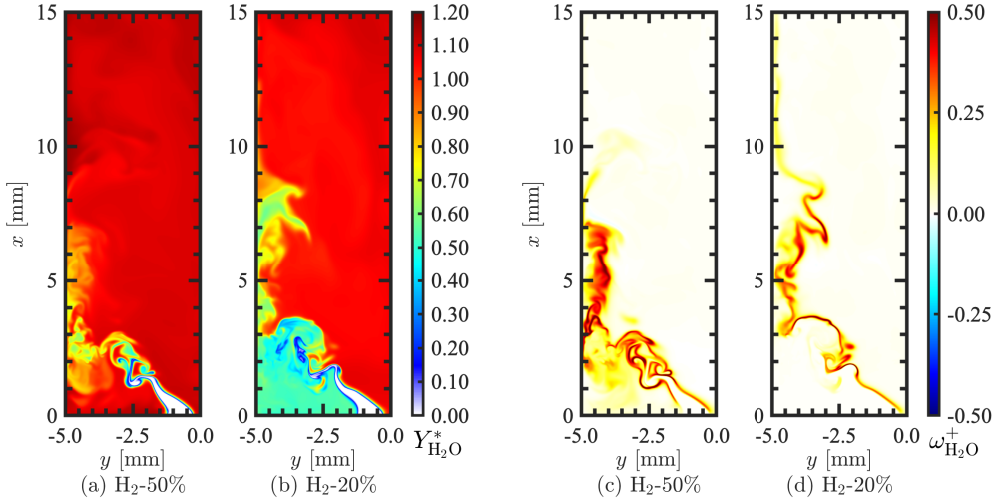


Figure 3.9: Distributions of $Y^*_{H_2O}$ (a, b) and $\omega^+_{H_2O}$ (c, d) on the representative $x-y$ plane ($y \leq 0$, $z = 0$).

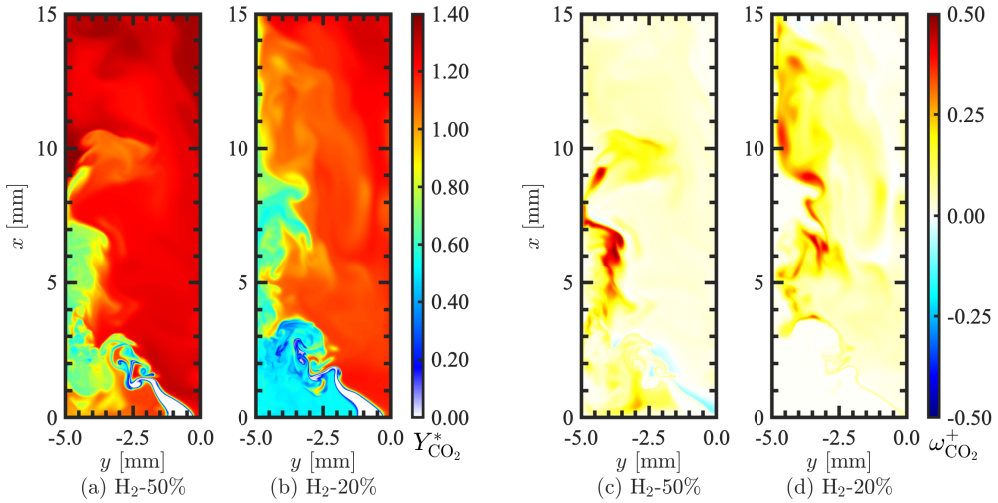


Figure 3.10: Distributions of $Y^*_{CO_2}$ (a, b) and $\omega^+_{CO_2}$ (c, d) on the representative $x-y$ plane ($y \leq 0$, $z = 0$).

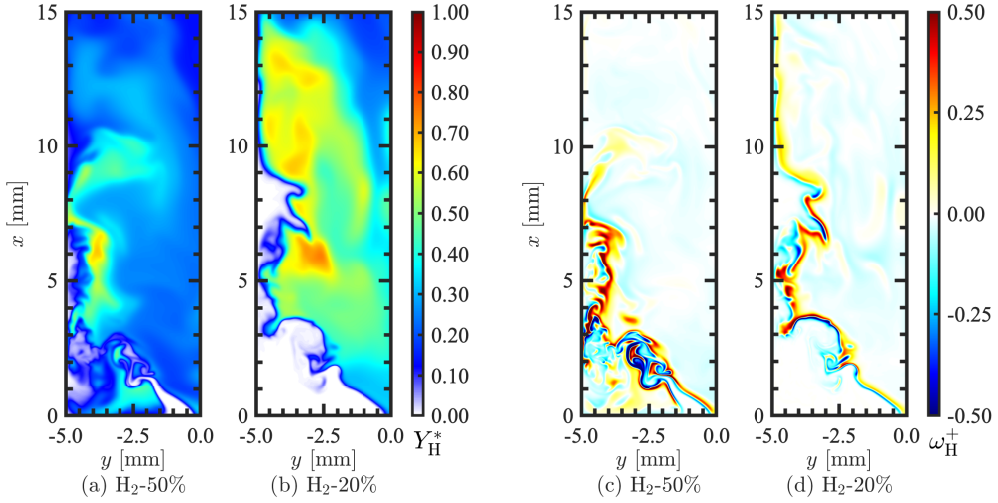


Figure 3.11: Distributions of Y^*_H (a, b) and ω^+_H (c, d) on the representative $x-y$ plane ($y \leq 0$, $z = 0$).

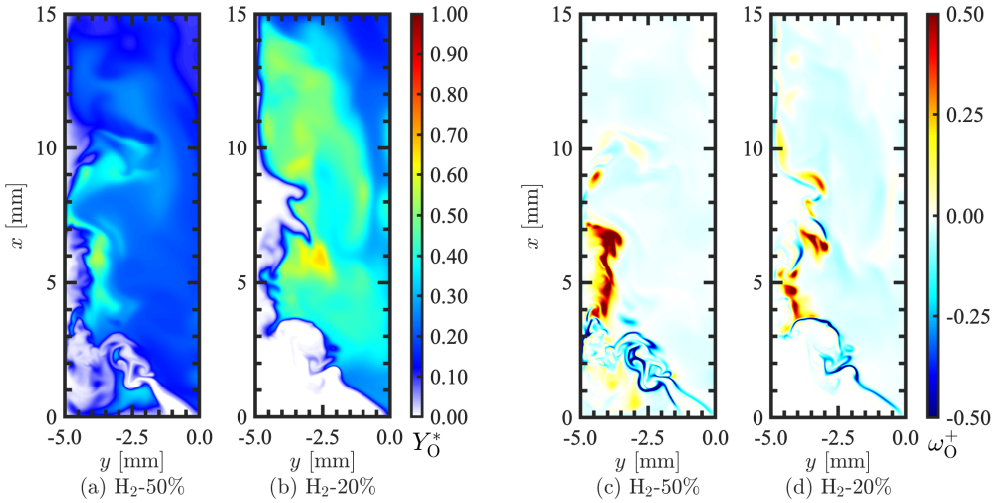


Figure 3.12: Distributions of Y_O^* (a, b) and ω_O^+ (c, d) on the representative $x-y$ plane ($y \leq 0$, $z = 0$).

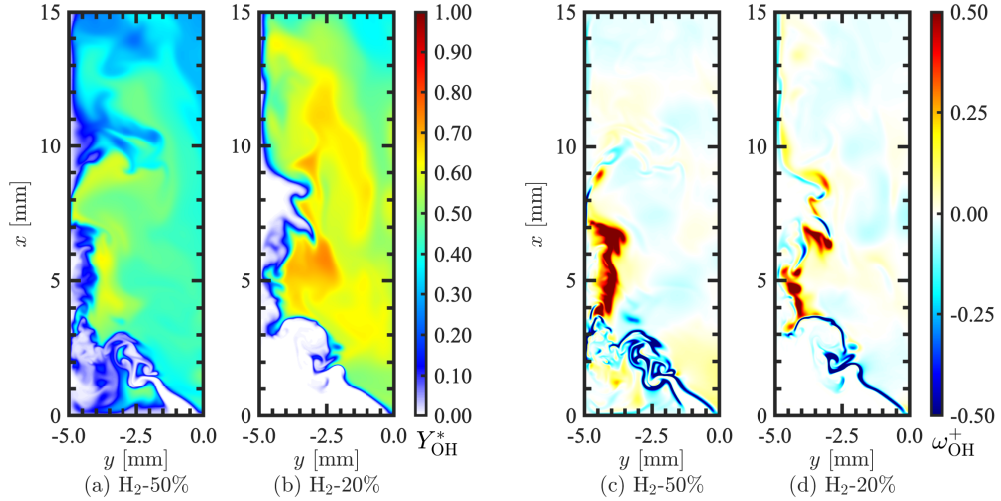


Figure 3.13: Distributions of Y_{OH}^* (a, b) and ω_{OH}^+ (c, d) on the representative $x-y$ plane ($y \leq 0$, $z = 0$).

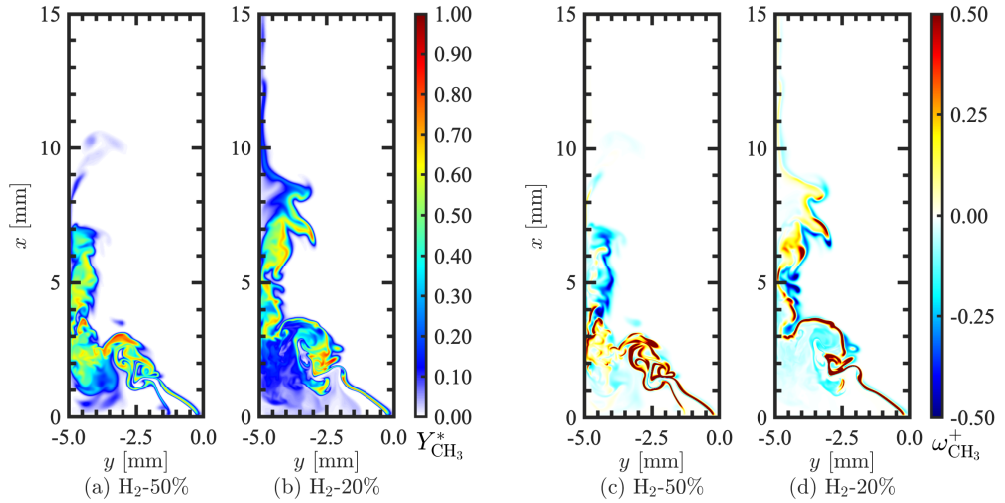


Figure 3.14: Distributions of $Y^*_{CH_3}$ (a, b) and $\omega^+_{CH_3}$ (c, d) on the representative $x-y$ plane ($y \leq 0$, $z = 0$).

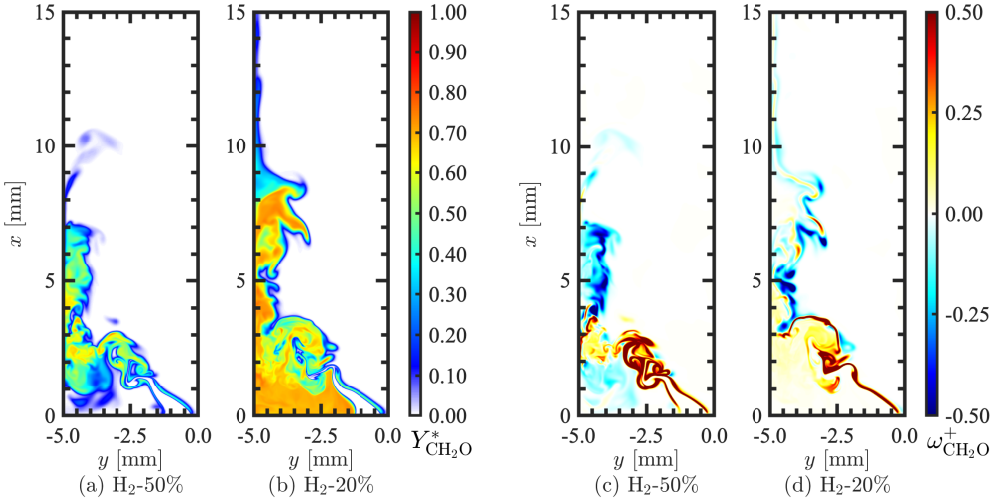


Figure 3.15: Distributions of $Y^*_{CH_2O}$ (a, b) and $\omega^+_{CH_2O}$ (c, d) on the representative $x-y$ plane ($y \leq 0$, $z = 0$).

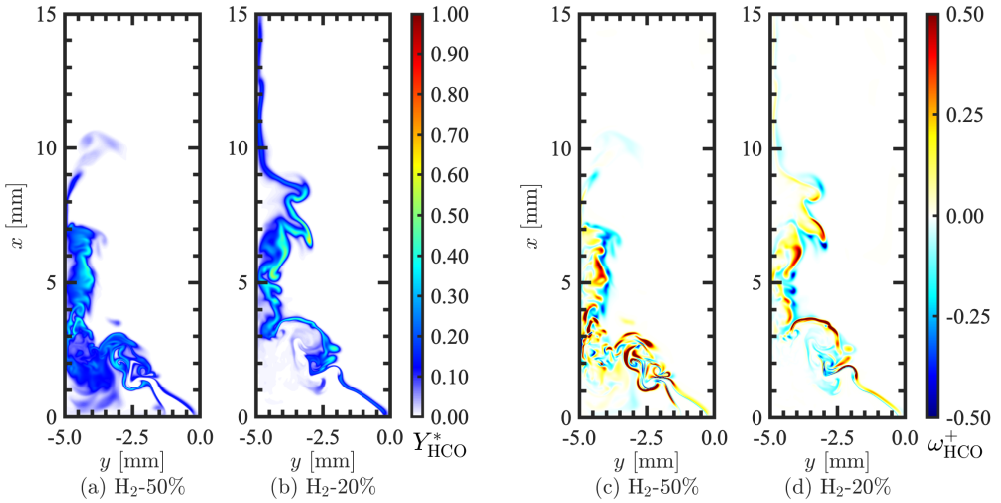


Figure 3.16: Distributions of Y^*_{HCO} (a, b) and ω^+_{HCO} (c, d) on the representative $x-y$ plane ($y \leq 0$, $z = 0$).

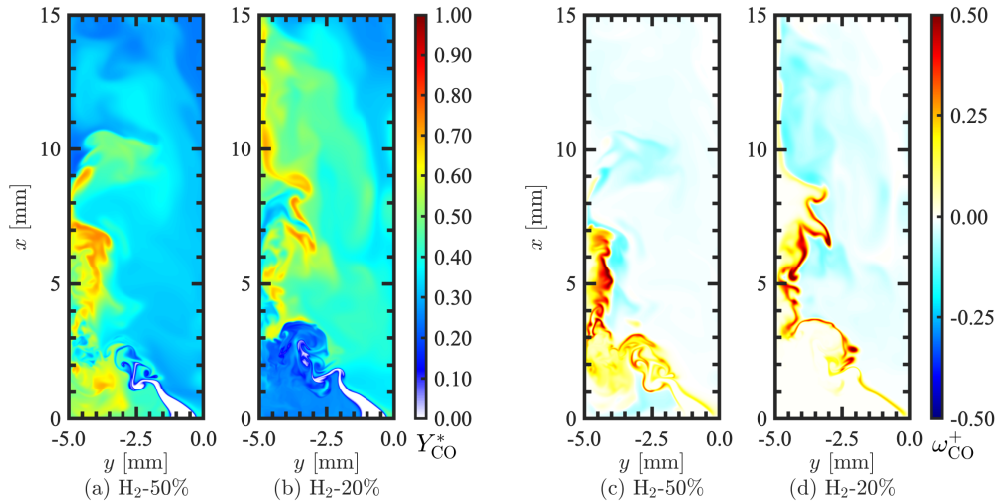


Figure 3.17: Distributions of Y^*_{CO} (a, b) and ω^+_{CO} (c, d) on the representative $x-y$ plane ($y \leq 0$, $z = 0$).

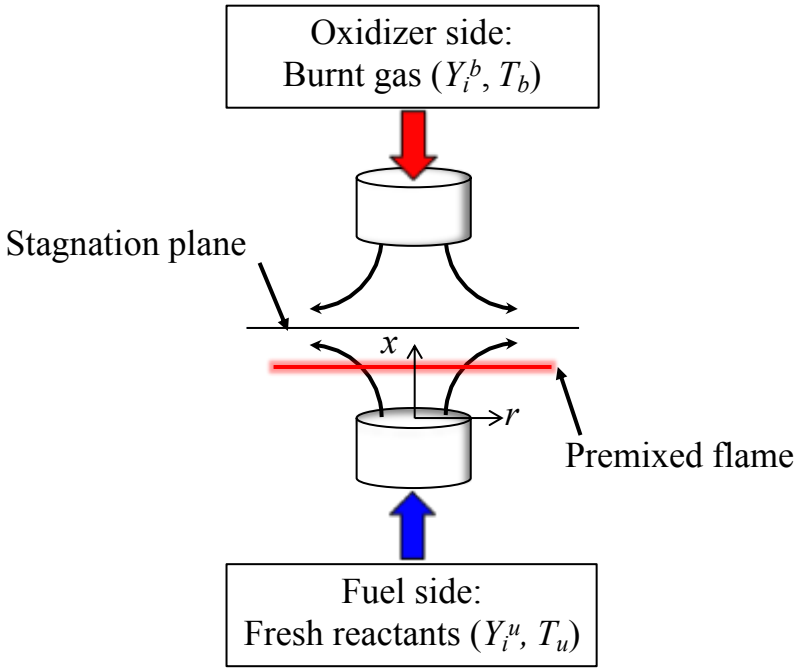


Figure 3.18: Schematic of counter flow single flame configuration.

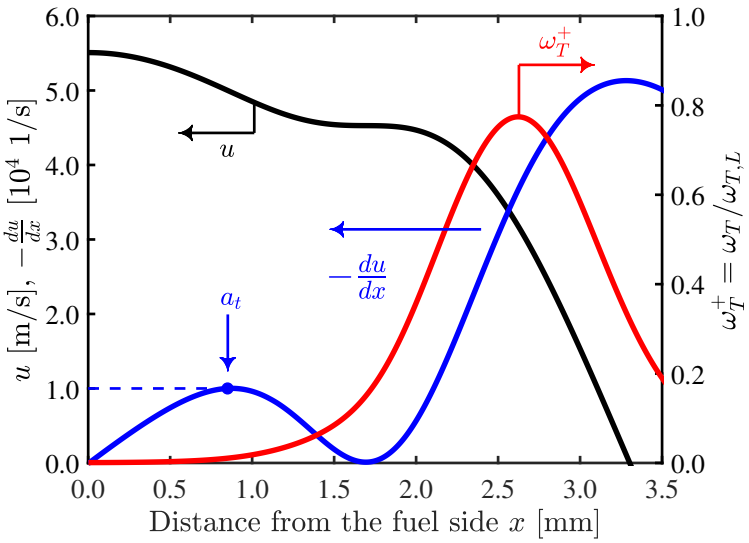


Figure 3.19: Velocity and heat release rate profiles and definition of tangential strain rate a_t in a canonical counter flow single flame configuration.

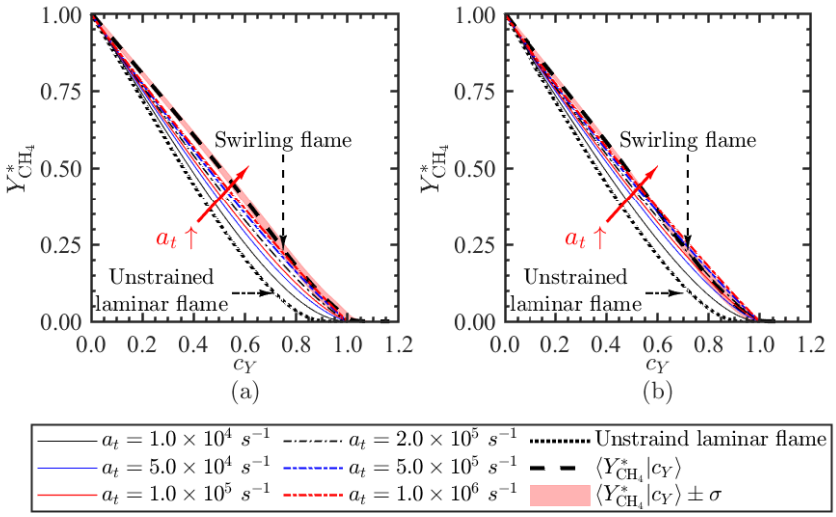


Figure 3.20: Comparison of conditionally averaged $Y^*_{CH_4}$ with unstrained and strained laminar flames for H_2-50% (a) and H_2-20% (b).

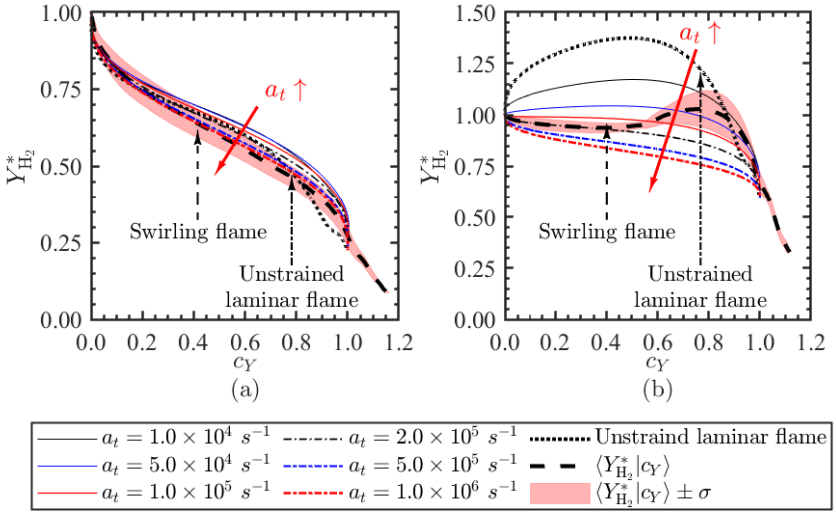


Figure 3.21: Comparison of conditionally averaged $Y^*_{H_2}$ with unstrained and strained laminar flames for H_2-50% (a) and H_2-20% (b).

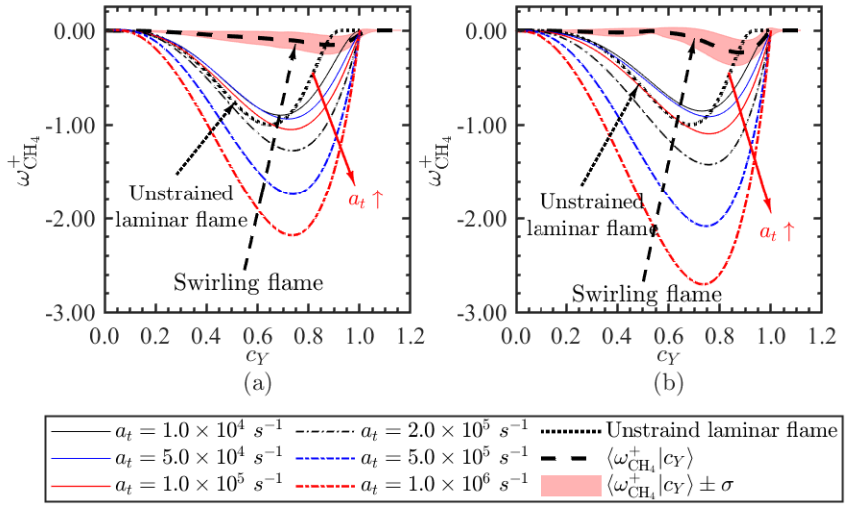


Figure 3.22: Comparison of conditionally averaged $\omega^+_{CH_4}$ with unstrained and strained laminar flames for H_2-50% (a) and H_2-20% (b).

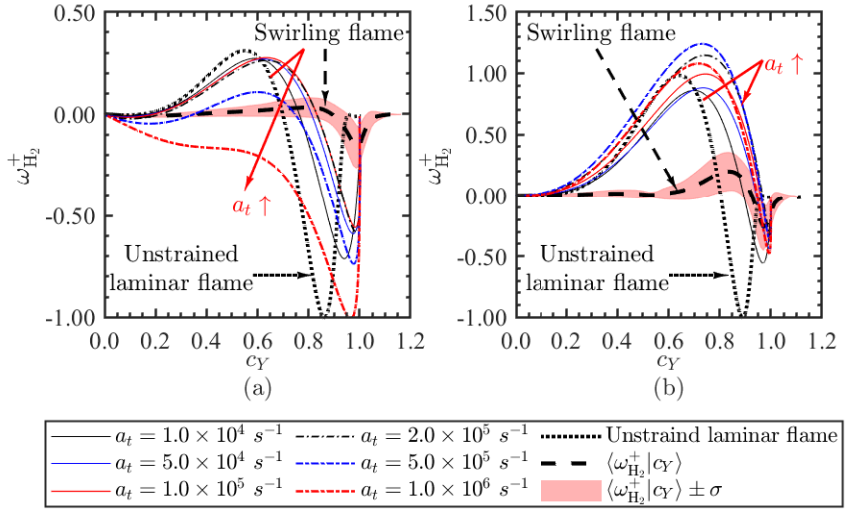


Figure 3.23: Comparison of conditionally averaged $\omega^+_{H_2}$ with unstrained and strained laminar flames for H_2-50% (a) and H_2-20% (b).

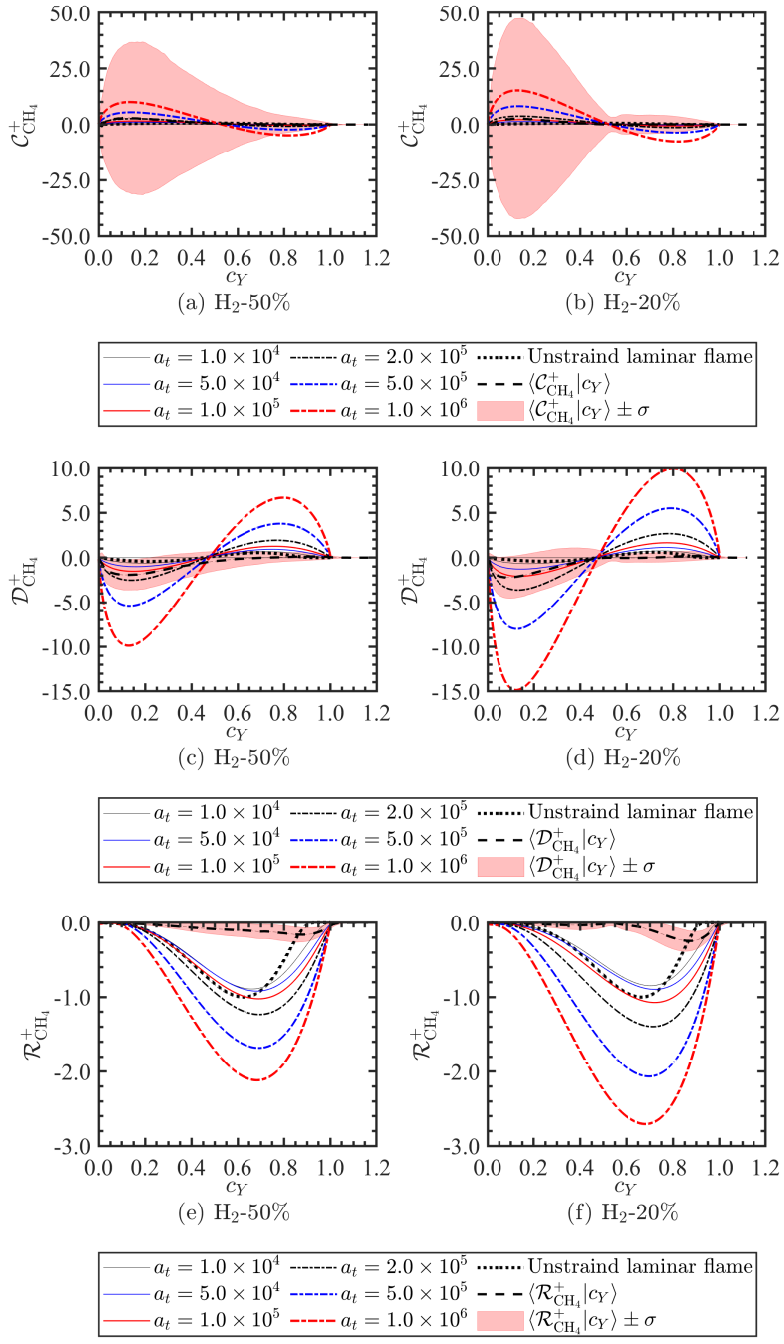


Figure 3.24: Conditionally averaged contributions of convection $\mathcal{C}^+$, diffusion $\mathcal{D}^+$ and chemical reaction $\mathcal{D}^+$ of CH_4 for H_2-50% (a,c and e) and H_2-20% (b,d and f).

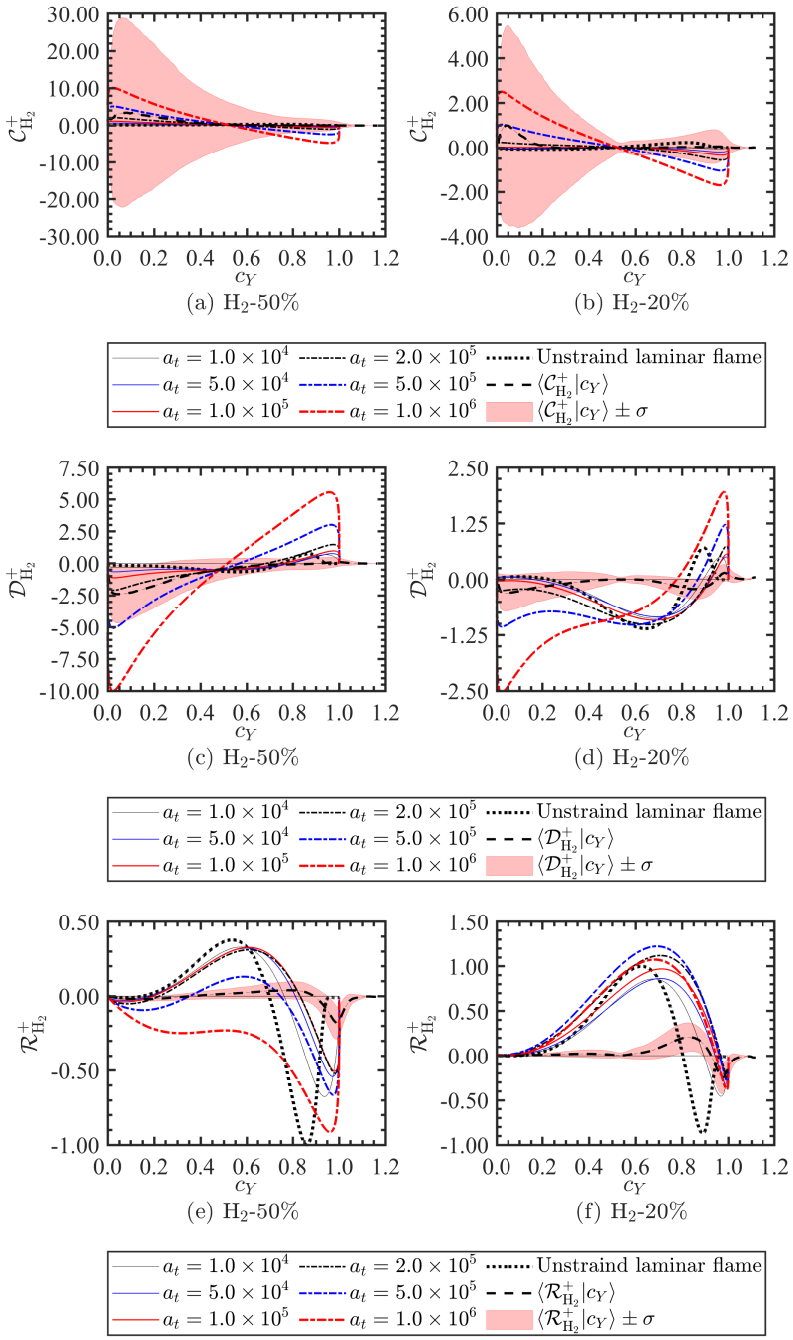


Figure 3.25: Conditionally averaged contributions of convection C^+, diffusion $\mathcal{D}^+$ and chemical reaction $\mathcal{R}^+$ of H_2 for H_2-50% (a, c and e) and H_2-20% (b, d and f).

Chapter 4

Local flame structures and extinction mechanism

4.1 Preface

As shown in chapter 2, the turbulent combustion conditions of the present study are categorized into the thin reaction zones regime and the Karlovitz numbers are relatively higher than the previously reported H_2/air cases [24, 59–61]. For the turbulent flames categorized into the thin reaction zones regime, it is assumed that the preheat zones are disturbed by turbulent motions and heat and mass diffusion are enhanced. Hence, local reaction and heat release rates would be different from those of the laminar flames. In addition, flame surface modification by turbulent motions yields changes in local flame structures through reaction pathway alternation and heat and mass diffusion. Therefore, the local flame structures of the present DNS are considered to be different form the laminar flames.

In chapter 3, it is revealed that the flame is stabilized in both inner and outer shear layers for H_2-50%, whereas extinction occurs in the outer shear layers for the lower H_2-20%. In gas turbine engines, it is important to elucidate flame stabilization and extinction mechanism of swirling premixed flames in a combustor to prevent limit phenomena, such as extinction, blowoff and flash back. Growth of local extinction with time may cause blowoff, which result in decreased cobmustion efficiency and increased emissions of of unburnt hydro carbons.

Mechanisms and dynamics of extinction and blowoff on the bluff body stabilized flames are tentatively studied and reviewed [87]. In turbulent premixed flames, mechanisms of extinctintion have been discussed as 1) balance between the rate of entrainment of reactants into the recirculation zones [88], 2) energy balance between burnt gas, fresh reactants and heat release rate, 3) competition of contact time between combustible mixture and hot gases in the shear shear layer and chemical ignition time, 4) excessive strain rate on the flame surface [89]. In addition, decrease of dominant elemental reactions [90, 91] in 2-dimensional turbulent planar flames and heat losses and flame straining [92–94] are also considered to be reasons for the local extinction. There are also experiment studies which have investigated effects of fuel type, equivalence ratios and turbulence intensity on the local extinction and blow out [13, 15, 95, 96].

In this chapter, effects of turbulent motions on the local flame structures and local extinction mechanisms in the shear layers are investigated. First, statistical characteristics of local flames structures and elemental reaction rates which mainly contribute to production and consumption of fuel species are clarified. Next, local extinction and flame stabilization mechanism in the shear layers are considered in the aspects of thermochemical conditions and flow strain rates of the flow field. Finally, effects of turbulent motions on the species distributions are investigated. It should be noted that, flash back is not considered in the present DNS.

4.2 Statistical characteristics of local flame structures

To investigate the local flame structures statistically, heat release rate and fuel species reaction rates on the defined flame surface are considered. Here, the flame surface is defined by iso-surface of c_Y^* which corresponds to the maximum heat release rate in the corresponding one-dimensional laminar flame as shown in Fig. 4.1. The value of c_Y^* is 0.65 for H_2-50% and 0.70 for H_2-20% respectively. Figure 4.2 shows schematics of definition of the flame surface and a variable sampled on

the defined flame surface. The local maximum value along the direction normal to the defined flame surface is sampled for statistics.

Figure 4.3 shows probability density functions (PDF) of normalized heat release rate on the defined flame surface. The average and standard deviation of heat release rate on the defined flame surface $\langle \omega_T^+ \rangle$ and $\sigma_{\omega_T^+}$ are shown in Table 4.1. As the figure shows, the peaks values of ω_T^+ appear at lower ω_T^+ for both cases. The peak of PDF appears at $\omega_T^+ = 0.0622$ and the maximum of ω_T^+ is 0.829 for H_2-50%. For H_2-20%, two peak values appear at $\omega_T^+ = 0.010$, 0.049 and the maximum of ω_T^+ is 0.987. These PDFs suggest that, large portion of the defined flame surfaces are locally extincted, on the other hand, there exist locally high heat release rates, though the numbers are small.

Figure 4.4 shows probability density functions (PDF) of normalized fuel species reaction rate on the defined flame surface. The average and standard deviation of fuel species reaction rates on the defined flame surface $\langle \omega_i^+ \rangle$ and $\sigma_{\omega_i^+}$ are shown in Table 4.2. As it is anticipated, the peaks of fuel species reaction rate $\omega_{CH_4}^+$ and $\omega_{H_2}^+$ appear nearly at 0 for both cases. The the minimum of $\omega_{CH_4}^+$ in the PDF appear at -1.08 for H_2-50% and -1.66 for H_2-20% which corresponds to a locally to intense consumption. In the PDF of $\omega_{H_2}^+$ for H_2-50%, the minimum and maximum value of $\omega_{H_2}^+$ is -0.286 and 0.424 respectively. The existence of consumption reaction on the defined flame surface may suggest that effects of turbulent motions on the local flame structures, because production of H_2 occurs in the corresponding one-dimensional laminar flame as shown in Fig. 4.1a. For H_2-20%, the maximum value of $\omega_{H_2}^+$ is 1.26, which indicates the existence of active production of H_2 compared to the corresponding laminar flame. These statistical characteristics suggest effects of turbulent motions on the local flame structure. To clarify these trends in detail, contributions of elemental reactions which are related to production and consumption of the fuel species and effects of tangential strain rates on the elemental reaction rates are investigated.

4.3 Contributions of elemental reactions

4.3.1 Distributions of elemental reaction rates

Figures 4.5 and 4.6 show reaction rate profiles of elemental reactions which mainly contribute to production and consumption of CH_4 in the corresponding one-dimensional unstrained laminar flame for both mixture conditions in physical and phase space respectively.

$$R_{41} : CH_4 + H \rightleftharpoons H_2 + CH_3 \tag{4.1}$$

$$R_{42} : CH_4 + OH \rightleftharpoons H_2O + CH_3 \tag{4.2}$$

$$R_{43} : CH_4 + O \rightleftharpoons CH_3 + OH \tag{4.3}$$

$$R_{56} : H + CH_3(+M) \rightleftharpoons CH_4(+M) \tag{4.4}$$

Here, “Others" denotes the sum of the reactions other than the dominant reactions.

$$\omega^+_{CH_4,\mathrm{Others}} = \omega^+_{CH_4} - (\omega^+_{CH_4,R_{41}} + \omega^+_{CH_4,R_{42}} + \omega^+_{CH_4,R_{43}} + \omega^+_{CH_4,R_{56}}). \tag{4.5}$$

The superscript “+" denotes that the elemental reaction rates are normalized by the maximum of $|\omega_i|$, the absolute value of reaction rate for the i-th species as defined in the previous chapter. As the figures show, the contributions by the elemental reactions to $\omega^+_{CH_4}$ do not change significantly with the increase of H_2 ratios. Furthermore, the contributions by the other reactions are negligibly small.

2-dimensional distributions of elemental reactions mainly contribute to reaction rate of $\omega^+_{CH_4}$ on the representative plane are shown in Figs. 4.7 and 4.8. To compare the contributions of elemental reaction in more detail, temperature and elemental reaction rates along the y-axis at x = 0.625, 1.25 and 2.50 mm are also shown in Fig. 4.9. For both cases, the contributions of elemental reaction are decreased substantially compared to the maximum of $|\omega_{CH_4}|$ in the corresponding laminar flame, while the chemical pathway of CH_4 for each mixture condition seems to be remain unchanged. As shown in the previous chapter, the contribu-

tions by elemental reactions can be observed in the OSL and ORZ for H_2-50%. In addition, the contributions by each elemental reaction in the ISL and OSL are relatively similar. For H_2-20%, elemental reaction rates in the OSL and ORZ are decreased substantially compared to the values in the ISL and IRZ, as shown in Fig. 3.6b. Moreover, the elemental reactions do not proceed any more even with high temperature, fuels and oxygen mass fraction in the region aforementioned (Fig. 4.10b). Hence, the decreased reaction rates for H_2-50% and extinction for H_2-20% in the OSL are considered to be caused by decreased contributions. Furthermore, since elemental reactions occur with reactants and thermal energy, decreased elemental reaction rates are considered to be decreased amount of radicals for H_2-50% and lack of radicals in the OSL and ORZ (Fig. 4.11).

Reaction rate profiles of elemental reactions which mainly contribute to production and consumption of H_2 in the corresponding one-dimensional unstrained laminar flame for both mixture conditions are shown by the same manners in Figs 4.12 and 4.13.

$$R_2 : H_2 + O \rightleftharpoons OH + H \tag{4.6}$$

$$R_3 : H_2 + OH \rightleftharpoons H_2O + H \tag{4.7}$$

$$R_{36} : CH_2O + H \rightleftharpoons HCO + H_2 \tag{4.8}$$

$$R_{41} : CH_4 + H \rightleftharpoons H_2 + CH_3 \tag{4.9}$$

$$\omega^+_{H_2,\mathrm{Others}} = \omega^+_{H_2} - (\omega^+_{H_2,R_2} + \omega^+_{H_2,R_3} + \omega^+_{H_2,R_{36}} + \omega^+_{H_2,R_{41}}) \tag{4.10}$$

Different from the profiles for $\omega^+_{CH_4}$, the contributions by elemental reactions change between the mixture conditions and contributions by the other reactions are not negligible. Contributions by R_{36}, R_{41} and others to the production of H_2 become smaller with the increase of H_2-ratios in the mixture conditions.

Figures 4.14 and 4.15 show 2-dimensional distributions of elemental reactions related to production and consumption of H_2. One-dimensional distributions of the elemental reaction rates along the y-axis are also shown in Fig. 4.16. Similar to the distributions of $\omega^+_{CH_4,k}$, the contributions by the elemental reactions are

decreased substantially compared with the maximum of $|\omega_{H_2}|$ in the unstrained laminar flame. Different from the distribution of $\omega^+_{CH_4,k}$, relatively high values of $\omega^+_{H_2,k}$ are observed in the downstream. For H_2-50%, the elemental reactions occur in the OSL and ORZ and the magnitudes of each elemental reaction in the ISL and OSL are relatively similar. For H_2-20%, production of H_2 by R_{36} and R_{41} occur actively, suggesting that the chemical pathway of H_2 for each mixture condition remains unchanged. As one-dimensional distributions of Y^*_{HCO}, $Y^*_{CH_2O}$ and $Y^*_{CH_3}$ in Fig. 4.17 show, it is of interest that the values of $Y^*_{CH_2O}$ remain high in the upstream for H_2-20%. This is also considered to be due to not only by the lowered temperature but also decreased amount of radicals in the ORZ.

4.3.2 Effects of tangential strain rate on elemental reaction rates

To further investigate the contributions of the elemental reaction rates in the reaction zones, comparison of conditional means of elemental reactions $\langle \omega^+_{CH_4,k} | c_Y \rangle$ with unstrained and strained laminar flames are shown in Figs. 4.18 to 4.21. In the strained laminar flames, the peak values of $\omega^+_{CH_4,R_{41}}$, $\omega^+_{CH_4,R_{42}}$ and $\omega^+_{CH_4,R_{43}}$ increase and the peaks shift towards the burnt gas side with the increase of tangential strain rate a_t. While, the peaks of $\omega^+_{CH_4,R_{56}}$ shift towards the reactants sides with the increase of a_t.

As considered before, the conditionally averaged elemental reaction rates are decreased substantially in the reactants side and deviate from the laminar flames. In the burnt gas side, the values increase gradually, due to reacting with radicals of the recirculated burnt gases. Therefore, it can be concluded that the decreased reaction rates for H_2-50% and extinction in the OSL for H_2-20% are due to decreased contributions by elemental reactions resulted from lower levels of H, O, and OH in the ORZ as shown in Figs. 3.11 to 3.13 and 4.11. Again, the comparison suggests that the decrease in the elemental reaction rates are not just simply by the effects of tangential strain rates.

Comparison of conditional means of elemental reactions $\langle \omega^+_{\mathrm{H_2},k} | c_Y \rangle$ with unstrained and strained laminar flames are shown in Figs. 4.22 to 4.25 by the same manners. Overall, the values of $\omega^+_{\mathrm{H_2},k}$ show more complicated responses to the a_t unlike the response of $\omega^+_{\mathrm{CH_4},k}$ to the a_t. With the increase of tangential strain rate a_t, the magnitudes of $\omega^+_{\mathrm{H_2,R_2}}$ decrease until $a_t = 10^5$ s^{-1}. With higher tangential strain rate, $a_t \geq 2.0 \times 10^5$ s^{-1}, the magnitudes increase again. The values of $|\omega^+_{\mathrm{H_2,R_3}}|$ decrease until $a_t = 10^5$ s^{-1} and are smaller than the unstrained laminar flame values. With further increase of a_t, the values increase gradually and becomes greater than the unstrained laminar flame values. The values of $\omega^+_{\mathrm{H_2,R_{36}}}$ decrease with the increase of a_t, while the magnitudes $\omega^+_{\mathrm{H_2,R_{41}}}$ increase and the peaks shift towards the burnt gas side.

Similarly, the magnitudes of conditionally averaged elemental reaction rate are decreased compared to the unstrained and strained laminar flames and deviate from the laminar flames in the reactants side. In the burnt gas side, the values increase gradually and show similar behaviors to the laminar flames. Therefore, the decreased reaction rates for H_2-50% and extinction in the OSL for H_2-20% are attributed to slow progress of elemental reactions which yield lower levels of H, O, and OH in the ORZ and affect the elemental reactions related to consumption and production of CH_4 again. Since the conditional means deviate from the unstrained and strained laminar flames, it can be said that only considering the effects of tangential strain rate a_t is not sufficient to predict the elemental reaction rates in the reaction zones. Further investigations considering the effects of three-dimensionality of the mean flow are shown next.

4.4 Investigation of extinction mechanism

4.4.1 Extinction strain rate in laminar flames

Before investigating the local extinction mechanism, extinction strain rates in laminar flames are considered here. The extinction strain rates are calculated by using CHEMKIN PRO. The calculations are conducted under twin flames

configuration in Fig. 4.26, of which mixture conditions and velocity (Y^u, T_u, u_{Fuel}) are identical at both sides. The Extinction strain rates are calculated iteratively by increasing the jet velocity gradually until the flame is to be extinguished. Figure 4.27 shows response curves of tangential strain rate and the maximum temperature T_{max} of the flame for mixture conditions of CH_4, CH_4:H_2=50:50 and CH_4:H_2=80:20. The equivalence ratio and preheat temperature are set to be same to the present DNS, $\phi = 1.0$ and $T_u = 700$ K. The tangential strain rate a_t is defined as the maximum of velocity gradient $-du/dx$ in the unburnt gas side. The extinction strain rate k_{ext} and extinction temperature T_{ext} are defined as the value of a_t and T_{max} where the slope of $a_t - T_{\mathrm{max}}$ is 0, hence $dT_{\mathrm{max}}/da_t = 0$.

With the increase of H_2 ratios, the extinction strain rate k_{ext} becomes greater and the flame can be sustained at relatively lower temperature under the same value of a_t. This is due to increase of reactivity and diffusivity with the increased amount of H_2 added to CH_4 in the mixture. In other word, it is expected that the flame with higher H_2-ratio mixture condition can be sustained with the same tangential strain rate and at relatively lower temperature. Furthermore, the values of k_{ext} obtained in this study are greater than the values reported by Shanbhogue et al. [37] which is obtained with initial temperature of 300 K, resulted from increased reactivity and diffusivity with elevated preheat temperature.

4.4.2 Extinction mechanism in shear layers

Figure 4.28 shows the 2-dimensional distributions of strain rate $\widetilde{s}$ in the representative plane. Here, the strain rate of the flow field $\widetilde{s}$ is calculated as:

$$\widetilde{s} = \widetilde{S_{ij}}\widetilde{S_{ij}}, \tag{4.11}$$

$$\widetilde{S_{ij}} = \frac{1}{2}\left(\frac{\partial \widetilde{u_i}}{\partial x_j} + \frac{\partial \widetilde{u_j}}{\partial x_i}\right). \tag{4.12}$$

where $\widetilde{u_i}$ denotes the Favre averaged velocity in the i-direction. The reason for using Favre averaged velocity $\widetilde{u_i}$ is to consider the effect of long term phenomena

and to compare with extinction strain rate in laminar flames. Since it is reported in previous studies [87, 97, 98], that the flames would not be extinguished or blown off immediately even with the strain rate exceeding its corresponding extinction strain rate k_{ext}.

As Figs. 4.28a and b show, the strain rates of the flow field $\widetilde{s}$ in the ISL and OSL are relatively similar for both cases, because almost the identical inflow boundary conditions are imposed. The values in the ISL are relatively higher than those in the OSL, due to thermal expansion by chemical reactions. To clarify the flame stabilization and extinction in the shear layers, distributions of strain rate normalized by the corresponding extinction strain rate k_{ext} are shown in Figs. 4.28c and d. For both cases, the normalized strain rates $\widetilde{s}/k_{\mathrm{ext}}$ in the shear layers of the upstream are much greater than the corresponding extinction strain rate k_{ext}. As expected, the values in ISL and OSL for H_2-20% are relatively higher than those of H_2-50%, because of smaller value of k_{ext}.

To investigate the flame stabilization and/or extinction mechanism in the shear layers in more detail, one-dimensional distributions of Favre averaged reaction progress variable, temperature $\widetilde{c_Y}, \widetilde{T}$ and time averaged reaction and heat release rates $\overline{\omega^+_{\mathrm{H_2}}}$, $\overline{\omega^+_{\mathrm{CH_4}}}$ and $\overline{\omega^+_T}$ are shown with $\widetilde{s}/k_{\mathrm{ext}}$ at x = 0.0, 0.625, 1.25 and 2.50 mm in Figs. 4.29 and 4.30.

As the distributions show, flames are stabilized in the ISL even with extremely higher values of $\widetilde{s}/k_{\mathrm{ext}}$ for both cases, which suggests that strain rates much higher than k_{ext} may decrease the reaction rates, but does not always lead to flame extinction. In addition, since the swirling flows convey high temperature burnt gases to reactants, it seems to be reasonable to consider that ISL is stabilized by recirculated high temperature burnt gas for both cases.

However, it is not accountable for the relatively similar magnitudes of reaction rates in the OSL for H_2-50% and extinction in the OSL for H_2-20% even with relatively lower values of $\widetilde{s}/k_{\mathrm{ext}}$ compared to those in the ISL. Furthermore, at x = 1.25 mm, the reaction and heat release rates are higher for H_2-20% even with higher $\widetilde{s}/k_{\mathrm{ext}}$ in Fig.4.30. This suggests that extremely high strain rate is not the only

reasons for extinction in the OSL and thermochemical conditions (temperature, species mass fraction and reaction rates) near the locally extincted region should be considered together.

In addition, it is concluded in [94] that extinction is considered to occur due to lower production rates of radicals in the low temperature region of the inner layer of the flame. Therefore, as shown in Fig. 4.31, flame stabilization in the ISL is achieved by recirculated high temperature burnt gases containing radicals. On the other hand, in the OSL, it is anticipated that the extinction for H_2-20% is due to not only excessively high strain rates but also lower temperature and lack of radicals in the ORZ.

Furthermore, it is reasonable to speculate that extinction in the OSL and ORZ for H_2-20% is not instantaneous phenomena. It is considered that re-ignition in the OSL failed for a long period of time and extincted area is extended to the ORZ with entrainment of cold reactants into the ORZ. This is also supported by studies in [99, 100], that the ignition temperature increases with the increase of strain rate, while it decreases with increase of H_2-ratio in CH_4/H_2 flames. Therefore, it is concluded that extinction in the OSL for H_2-20% is due to not only extremely high strain rates of the flow field but also lower temperature and production rates of radicals, which make re-ignition more difficult to occur.

4.5 Effects of turbulent motions on the chemical time scales

To investigate how the turbulent motions affect the distributions of reactive species, the ratios of turbulence time scale τ_η to chemical time scale τ_{c_i} [101] of each reactive species are shown in Fig. 4.32. Here, τ_η is defined by the Kolmogorov length scale η and the Kolmogorov velocity u_k averaged in the unburnt gas side of the flow field.

$$\tau_\eta = \frac{D}{1.2u_k} = \frac{8\eta}{1.2u_k}. \tag{4.13}$$

τ_{c_i} denotes the chemical time scale of the i-th species and defined as the ratio of the maximum molar concentration and the maximum reaction rate of the i-th species in the unstrained laminar flame.

$$\tau_{c_i} = \frac{[X_i]_{\max}}{|\omega_i|_{\max}}. \tag{4.14}$$

Hence, when the chemical time scale of the reactive species τ_{c_i} is longer than the turbulence time scale τ_η, $\tau_\eta/\tau_{c_i} < 1$, the mass fraction distributions of reactive species are strongly affected by the turbulence. Figure 4.32 shows that the chemical time scales of species except for H, t-CH_2 and s-CH_2 are shorter than the turbulence time scale. This suggests that most of the reactive species considered in this study are strongly affected by the turbulent motions. Therefore, the local flame structures are considered to be strongly affected by turbulent motions. Furthermore, since the τ_η/τ_{c_i} of fuels, oxygen, OH and O radicals are smaller than unity, it is speculated that the decreased reaction rates are also due to relatively shorter residential times of the species which may yield incomplete reaction.

4.6 Conclusions of this chapter

In this chapter, effects of turbulent motions on the local flame structures and extinction mechanisms in the shear layers are investigated. Statistical characteristics of local flames structures and elemental reaction rates mainly contribute to production and consumption of the fuel species are clarified. Next, conditions for extinction and flame stabilization in the shear layers are considered in the aspects of thermochemical and flow strain rates. Finally, effects of turbulent motions on the species distributions are investigated. The following conclusions are obtained.

1. Fuel species reaction rates and heat release rates are substantially decreased in large portion of the defined flame surface. However, locally high heat release and fuel species reaction rates also exists on the defined flame surface.

2. Contributions by elemental reaction rates are decreased substantially in the ORZ due to lack of radical species and lower temperature for H_2-20%. In addition, the conditionally averaged contributions by elemental reactions deviated from the unstrained and strained laminar flames.

3. The flame in the ISL is stabilized by high temperature burnt gas recirculated by swirling flows even with extremely high strain rates. On the other hand, to clarify the extinction in the OSL for H_2-20%, not only strain rate of the flow field but also thermochemical conditions in the near filed of the extincted region should be considered.

4. The decreased reaction rates are also speculated to be due to local chemical time scales affected by turbulent motions.

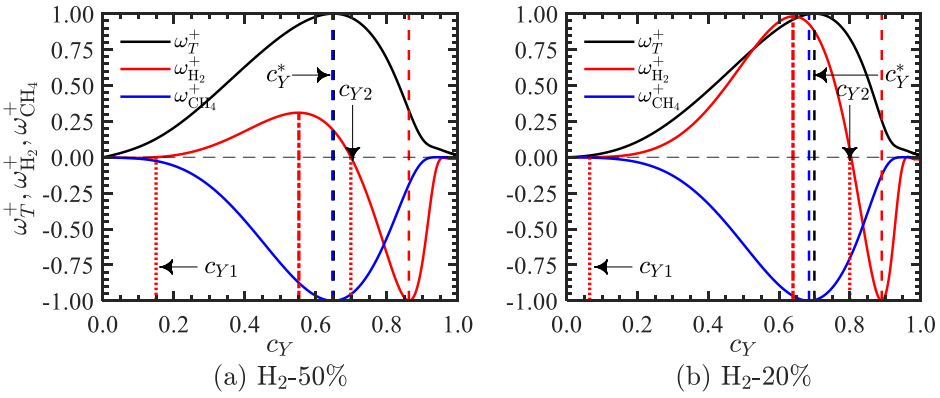


Figure 4.1: Fuel species reaction and heat release rate profiles of the corresponding laminar flame profile with respect to c_Y.

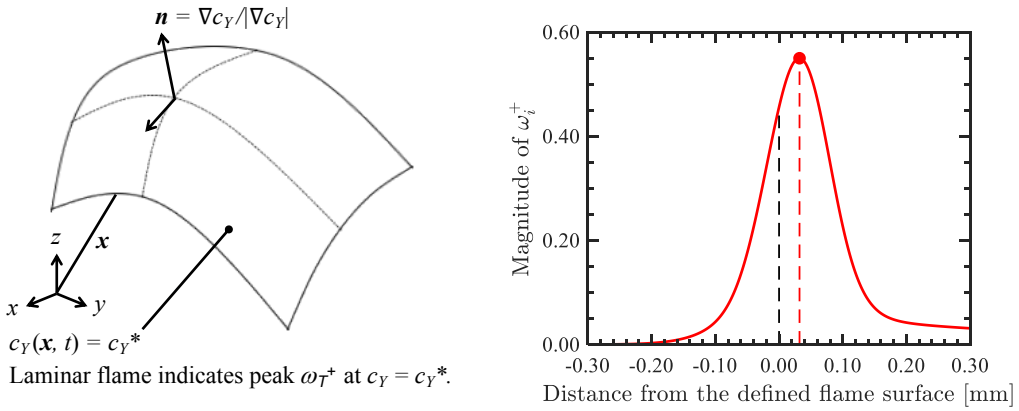


Figure 4.2: Schematics of defined flame surface (left) and a variable sampled on the defined flame surface (right).

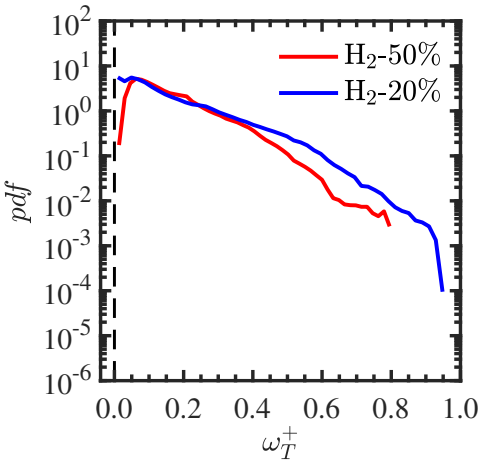


Figure 4.3: Probability density functions of ω_T^+on the defined flame surface.

Table 4.1: The average and standard deviation of normalized heat release rate on the defined flame surface.

Case	H_2-50%	H_2-20%
$\langle\omega_T^+\rangle$	0.154	0.146
$\sigma_{\omega_T^+}$	0.106	0.135

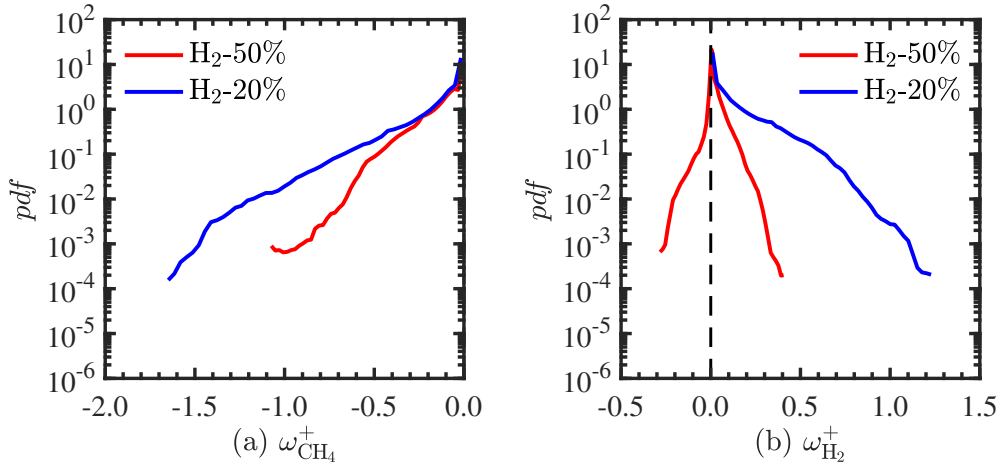


Figure 4.4: Probability density functions of $\omega^+_{CH_4}$ (a) and $\omega^+_{H_2}$ (b) on the defined flame surface.

Table 4.2: The average and standard deviation of normalized fuel species reaction rates ω_i^+ on the defined flame surface.

Case	H_2-50%	H_2-20%
$\langle\omega^+_{CH_4}\rangle$	-0.145	-0.165
$\sigma_{\omega^+_{CH_4}}$	0.121	0.193
$\langle\omega^+_{H_2}\rangle$	0.025	0.143
$\sigma_{\omega^+_{H_2}}$	0.045	0.160

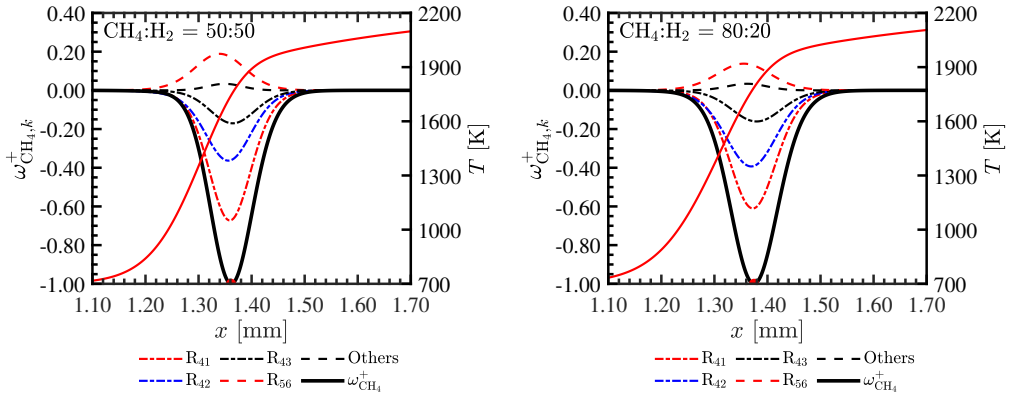


Figure 4.5: Elemental reaction rate profiles of ω_{CH_4} in the corresponding one-dimensional laminar flame for mixture conditions of CH_4:H_2 = 50:50 (left) and CH_4:H_2 = 80:20 (right) in physical space. The red line denotes temperature T.

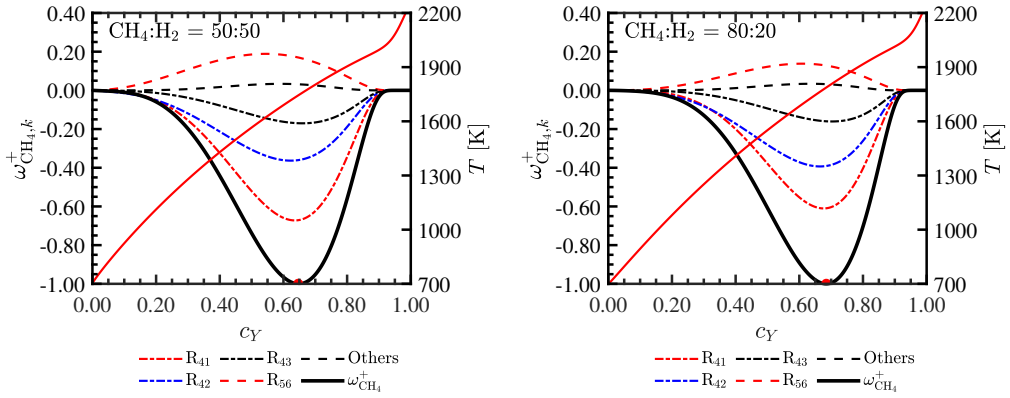


Figure 4.6: Elemental reaction rate profiles of ω_{CH_4} in the corresponding one-dimensional laminar flame for mixture conditions of CH_4:H_2 = 50:50 (left) and CH_4:H_2 = 80:20 (right) in phase space c_Y. The red line denotes temperature T.

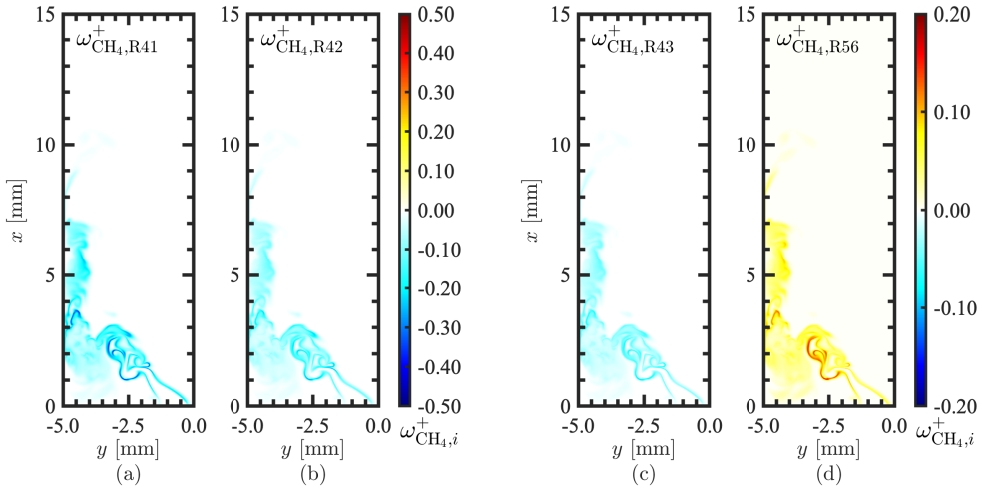


Figure 4.7: 2-dimensional distributions of elemental reaction rates by R_{41} (a), R_{42} (b), R_{43} (c) and R_{56} (d) on the representative $x-y$ plane ($y \leq 0$, $z = 0$) for H_2-50%.

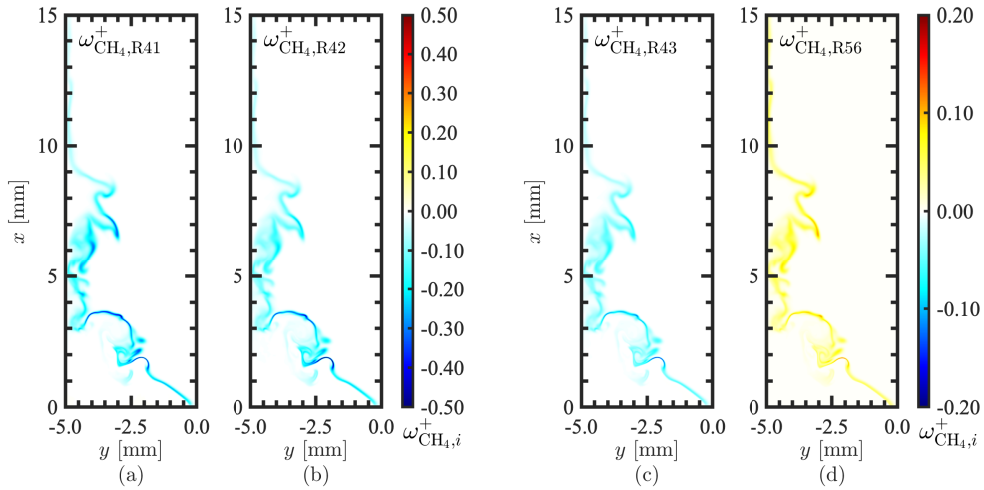


Figure 4.8: 2-dimensional distributions of elemental reaction rates by R_{41} (a), R_{42} (b), R_{43} (c) and R_{56} (d) on the representative $x-y$ plane ($y \leq 0$, $z = 0$) for H_2-20%.

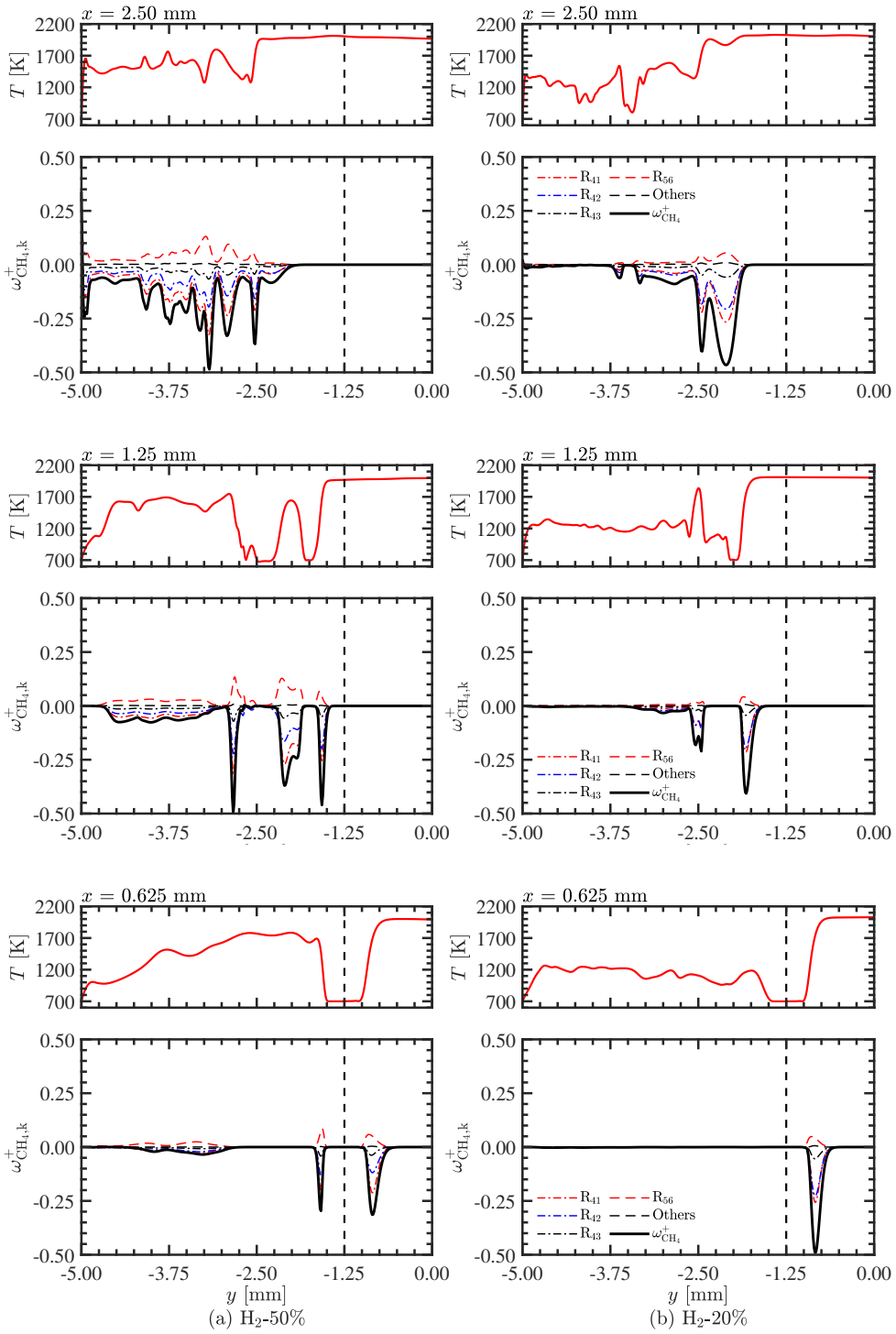


Figure 4.9: 1-dimensional distributions of temperature and elemental reaction rate by R_{41}, R_{42}, R_{43} and R_{56} at $x = 2.50$ (upper), 1.25 (middle) and 0.625 (lower) mm for H_2-50% (a) and H_2-20% (b).

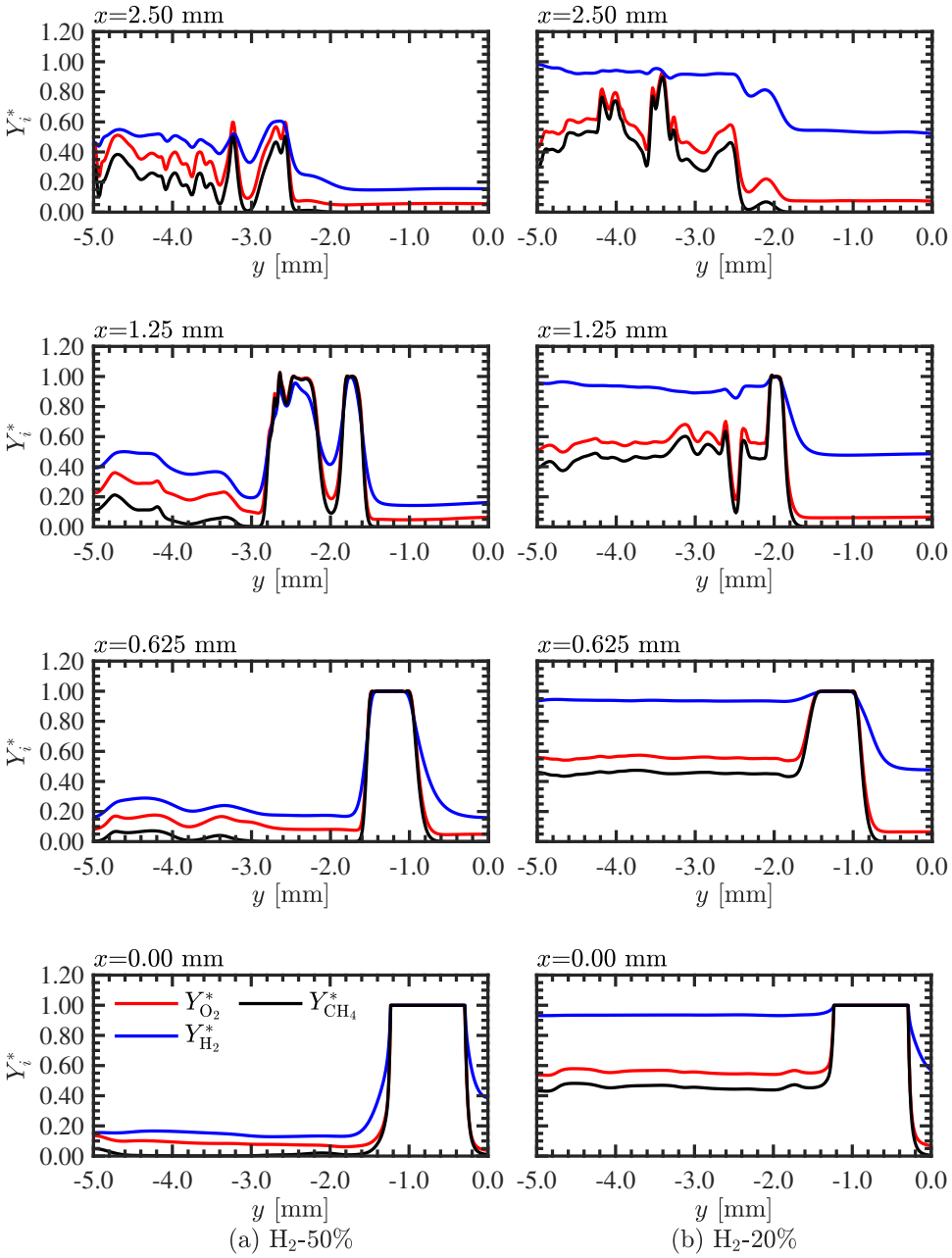


Figure 4.10: 1-dimensional distributions of normalized mass fraction, $Y^*_{CH_4}$, $Y^*_{H_2}$ and $Y^*_{O_2}$ at x = 0.0, 0.625, 1.25 and 2.50 mm for H_2-50% (a) and H_2-20% (b).

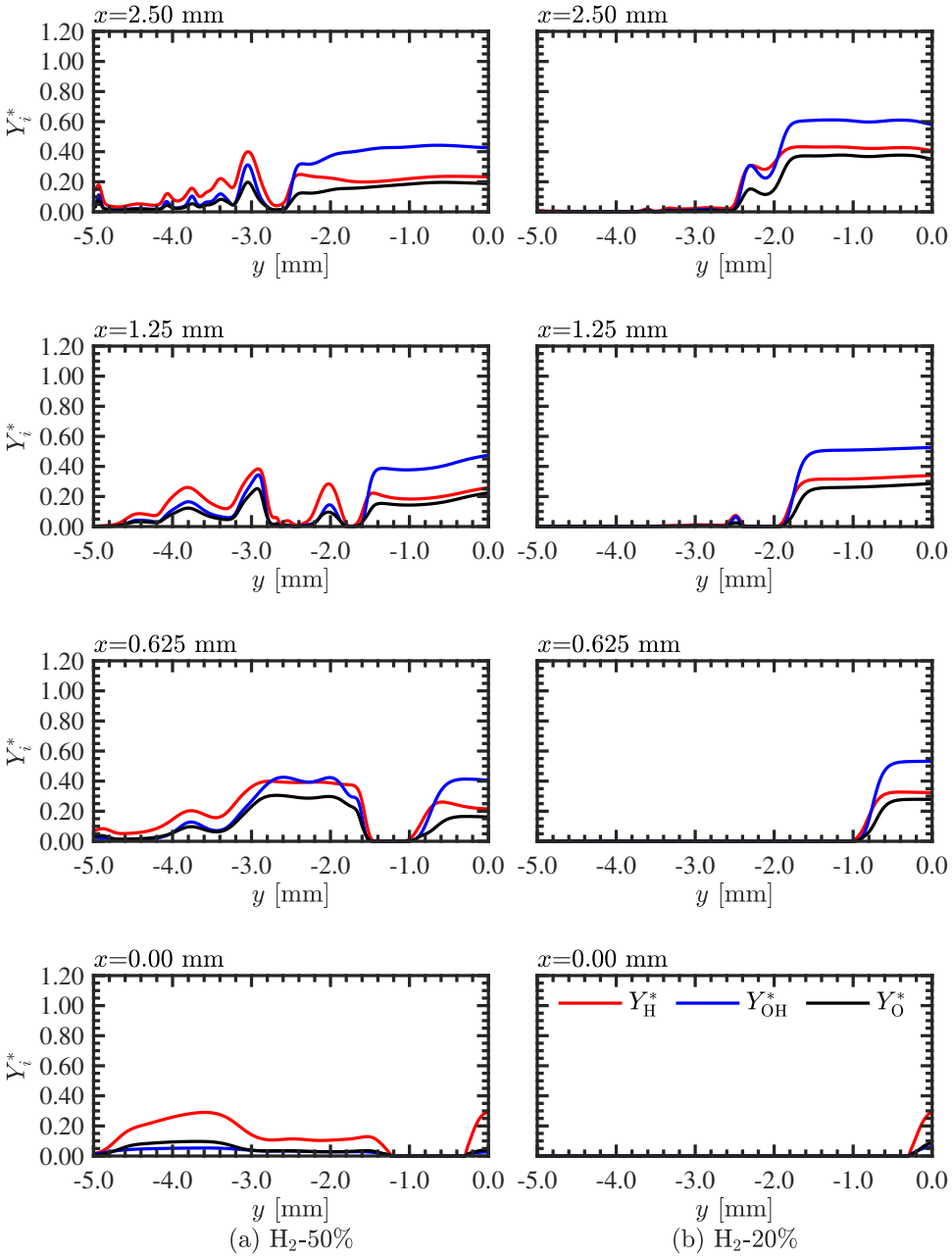


Figure 4.11: 1-dimensional distributions of radical species, Y_H^*, Y_{OH}^* and Y_O^* at x = 0.0, 0.625, 1.25 and 2.50 mm for H_2-50% (a) and H_2-20% (b).

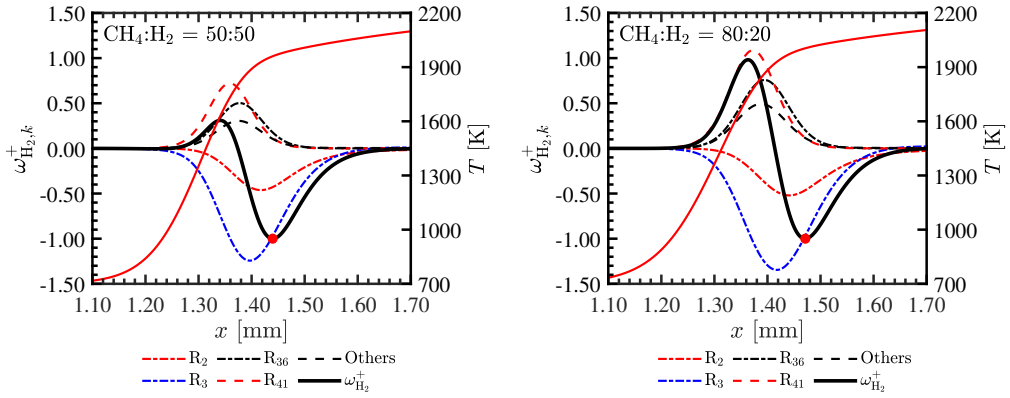


Figure 4.12: Elemental reaction rate profiles of ω_{H_2} in the corresponding one-dimensional laminar flame for mixture conditions of CH_4:H_2 = 50:50 (left) and CH_4:H_2 = 80:20 (right) in physical space. The red line denotes temperature T.

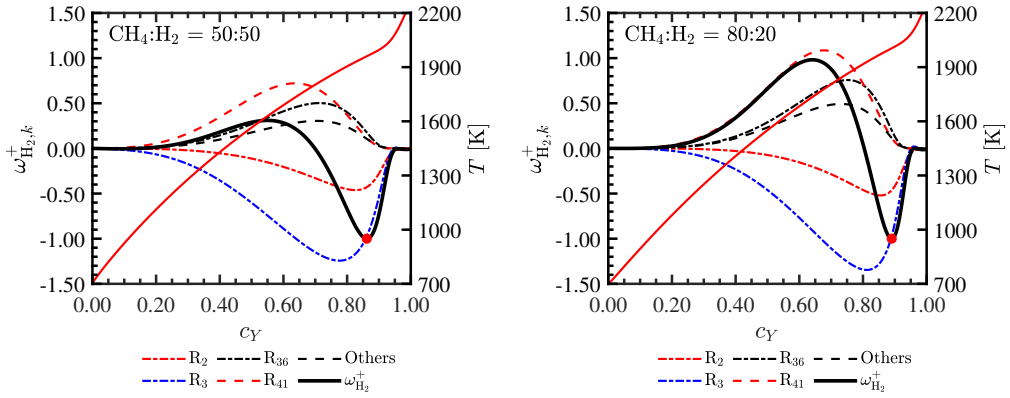


Figure 4.13: Elemental reaction rate profiles of ω_{H_2} in the corresponding one-dimensional laminar flame for mixture conditions of CH_4:H_2 = 50:50 (left) and CH_4:H_2 = 80:20 (right) in phase space c_Y. The red line denotes temperature T.

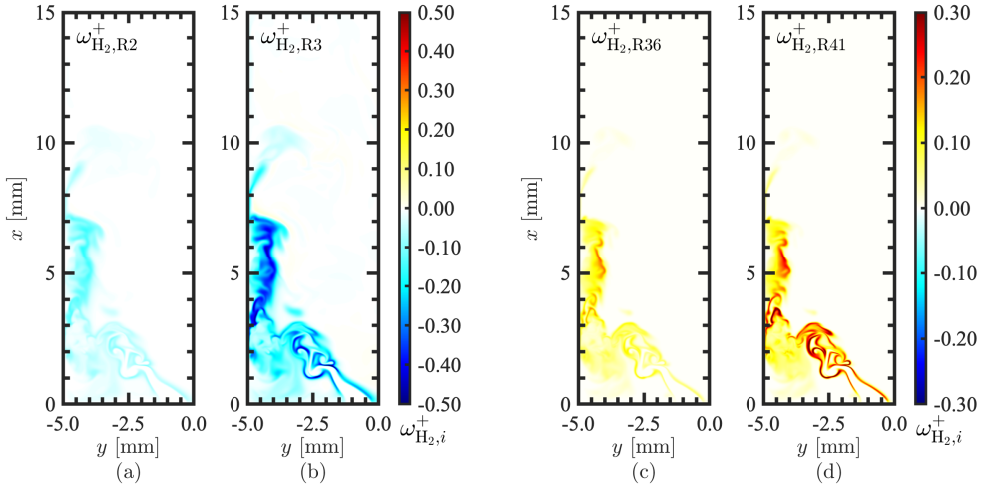


Figure 4.14: 2-dimensional distributions of elemental reaction rates by R_2 (a), R_3 (b), R_{36} (c) and R_{41} (d) on the representative $x-y$ plane ($y \leq 0$, $z = 0$) for H_2-50%.

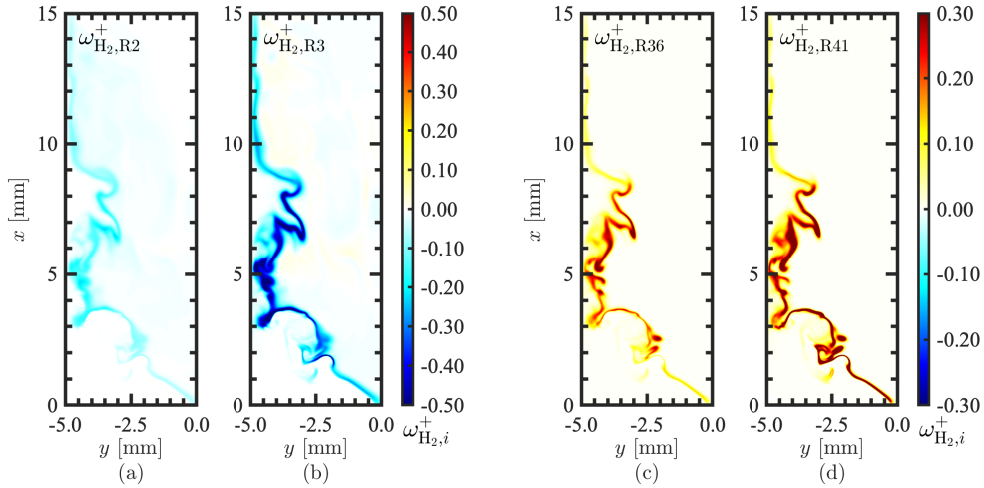


Figure 4.15: 2-dimensional distributions of elemental reaction rates by R_2 (a), R_3 (b), R_{36} (c) and R_{41} (d) on the representative $x-y$ plane ($y \leq 0$, $z = 0$) for H_2-20%.

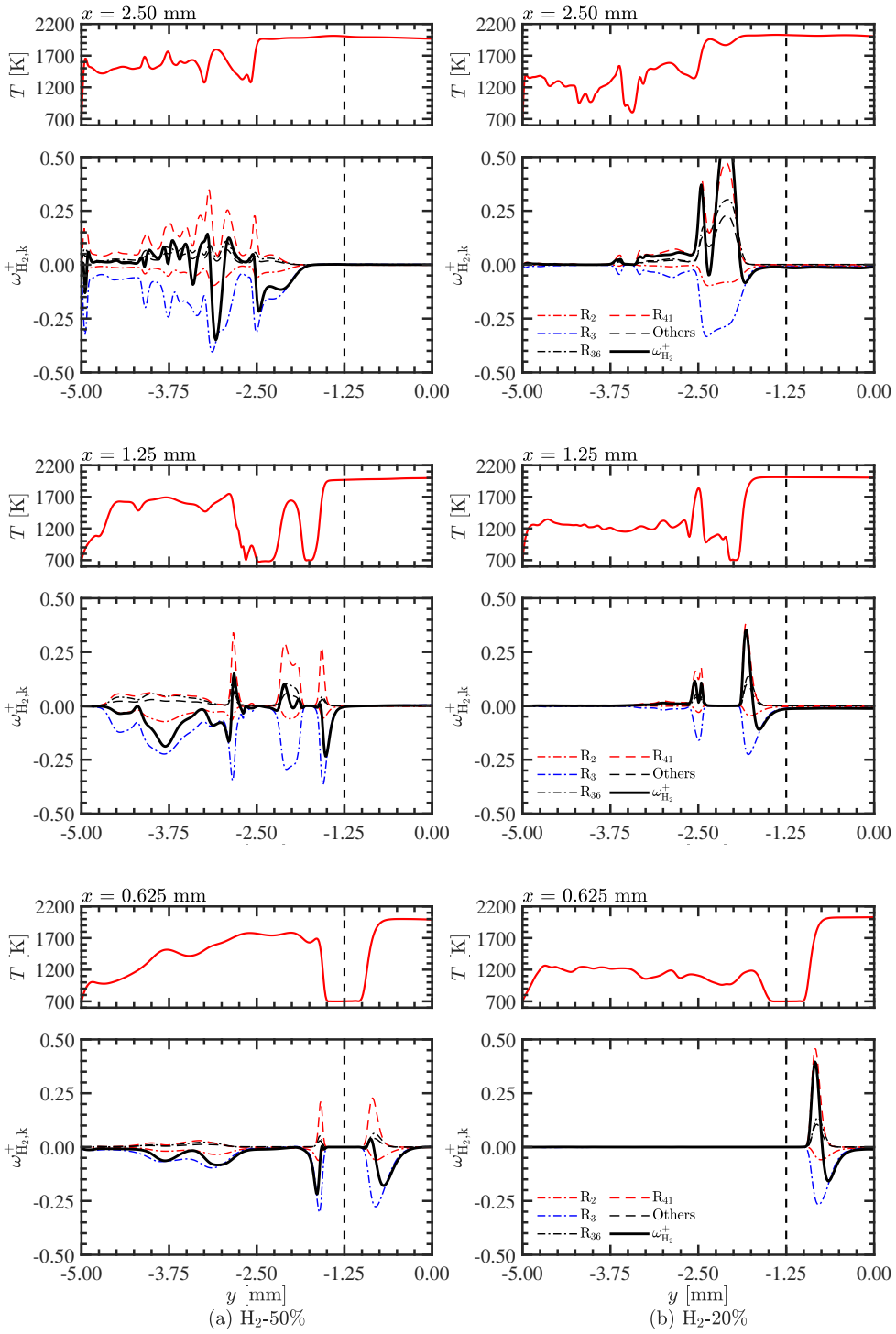


Figure 4.16: 1-dimensional distributions of elemental reaction rate by R_2, R_3, R_{36} and R_{41} at x = 2.50 (upper), 1.25 (middle) and 0.625 (lower) mm for H_2-50% (a) and H_2-20% (b).

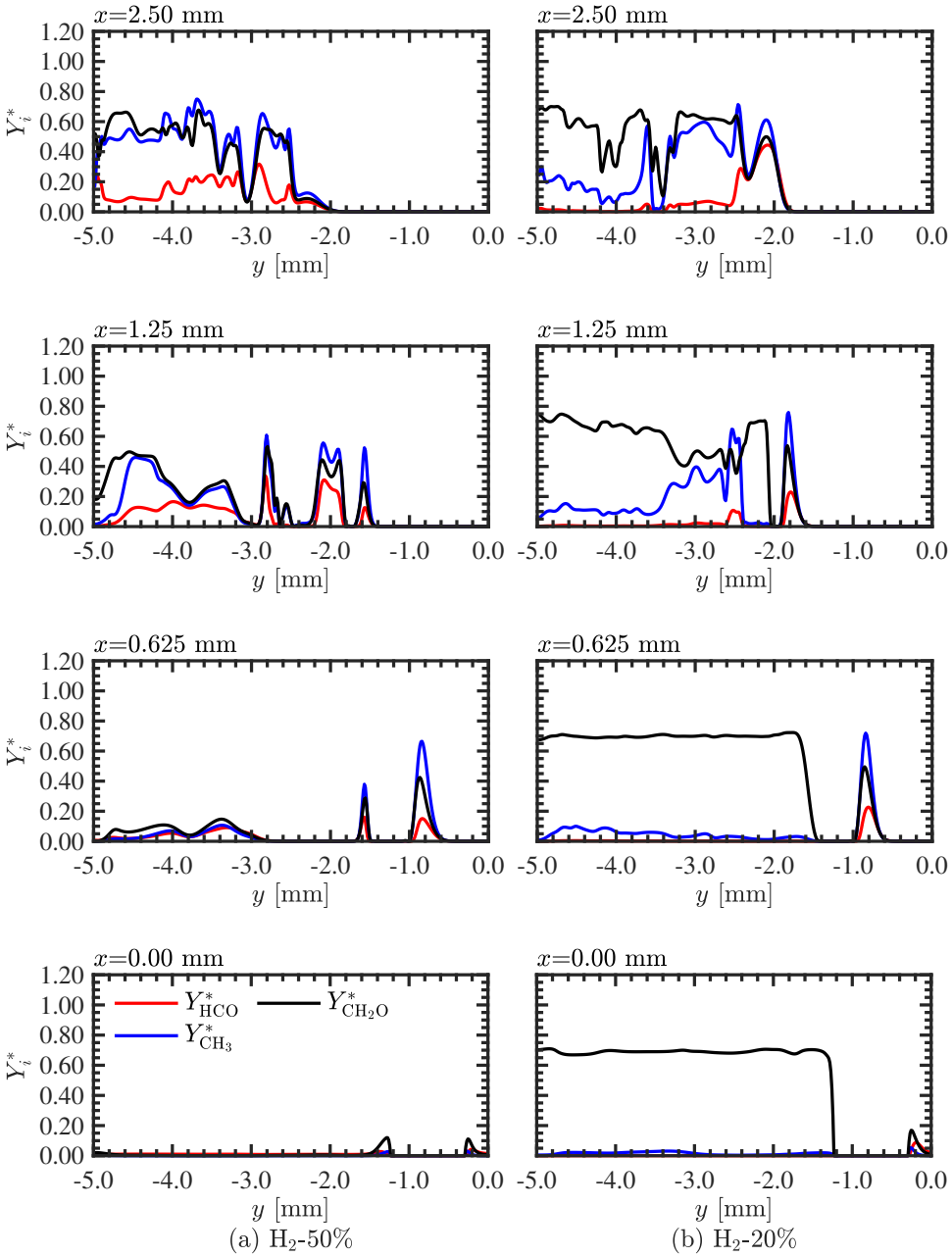


Figure 4.17: 1-dimensional distributions of radical species, Y^*_{HCO}, $Y^*_{CH_3}$ and $Y^*_{CH_2O}$ at x = 0.0, 0.625, 1.25 and 2.50 mm for H_2-50% (a) and H_2-20% (b).

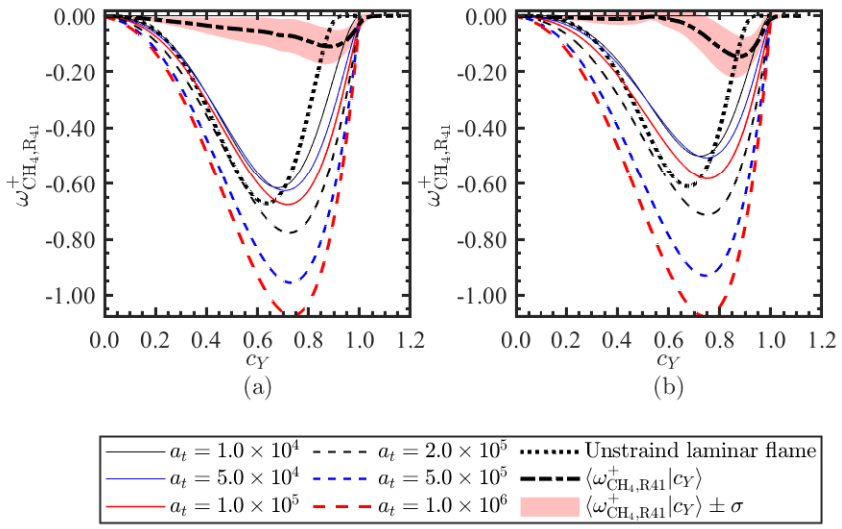


Figure 4.18: Comparison of conditionally averaged elemental reaction rate by R_{41} : CH_4 +H $\rightleftharpoons$ H_2+CH_3 with unstrained and strained laminar flames for H_2-50% (a) and H_2-20% (b).

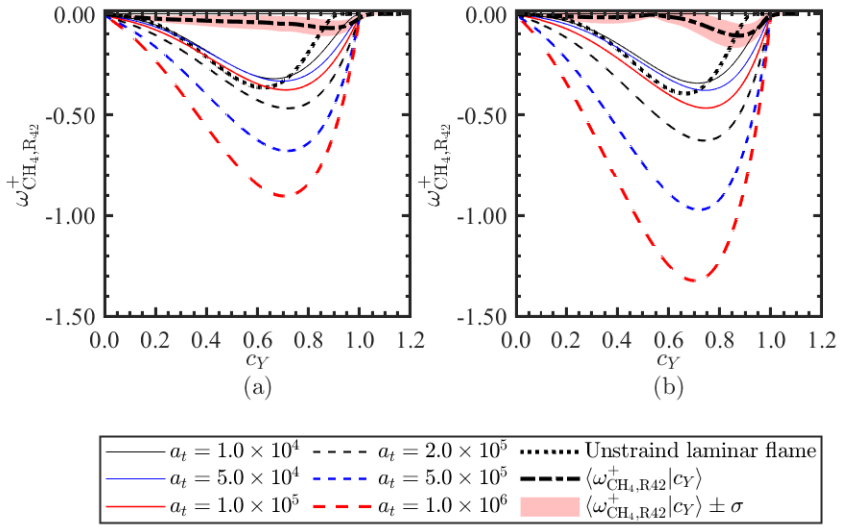


Figure 4.19: Comparison of conditionally averaged elemental reaction rate by R_{42} : CH_4 +OH $\rightleftharpoons$ H_2O+CH_3 with unstrained and strained laminar flames for H_2-50% (a) and H_2-20% (b).

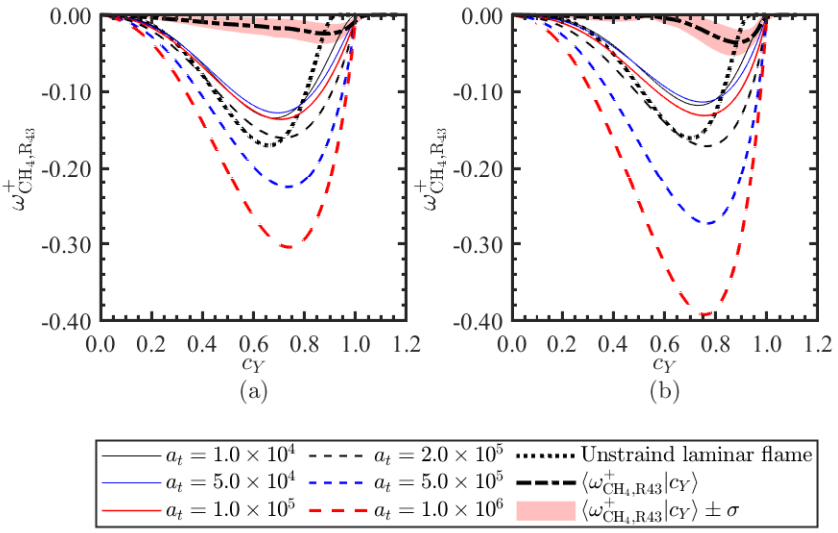


Figure 4.20: Comparison of conditionally averaged elemental reaction rate by R_{43} : CH_4 +O $\rightleftharpoons$ CH_3+OH with unstrained and strained laminar flames for H_2-50% (a) and H_2-20% (b).

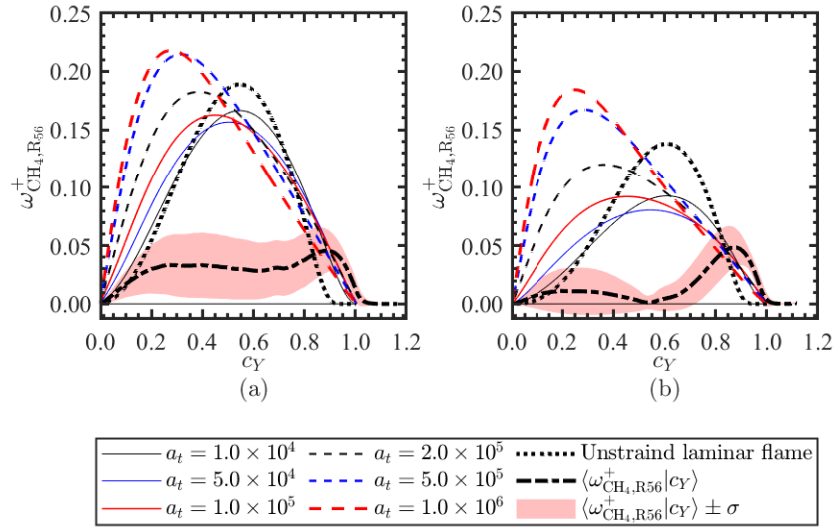


Figure 4.21: Comparison of conditionally averaged elemental reaction rate by R_{56} : H+CH_3 (+M) $\rightleftharpoons$ CH_4 (+M) with unstrained and strained laminar flames for H_2-50% (a) and H_2-20% (b).

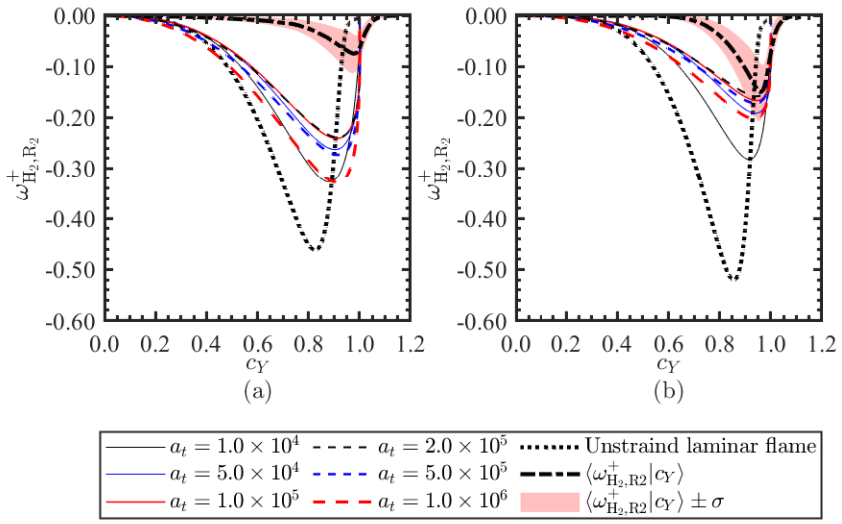


Figure 4.22: Comparison of conditionally averaged elemental reaction rate by R_2 : H_2+O ⇌ OH+H with unstrained and strained laminar flames for H_2-50% (a) and H_2-20% (b).

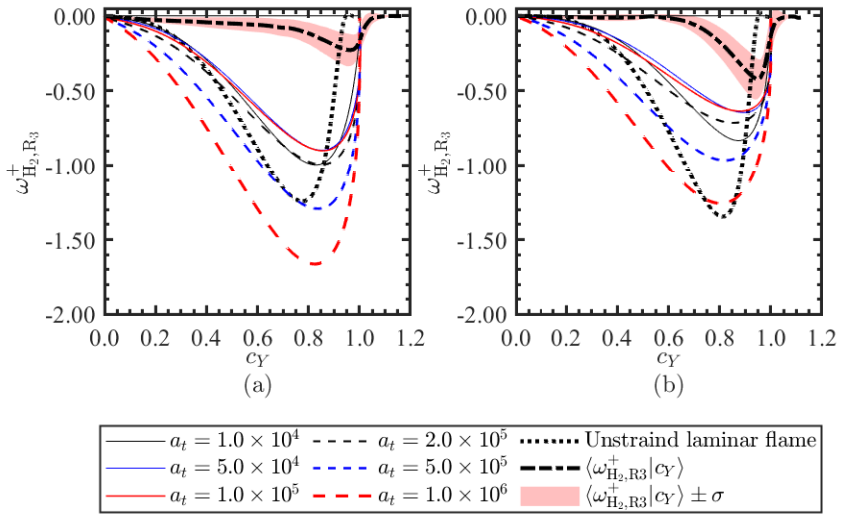


Figure 4.23: Comparison of conditionally averaged elemental reaction rate by R_3 : H_2+OH ⇌ H_2O+H with unstrained and strained laminar flames for H_2-50% (a) and H_2-20% (b).

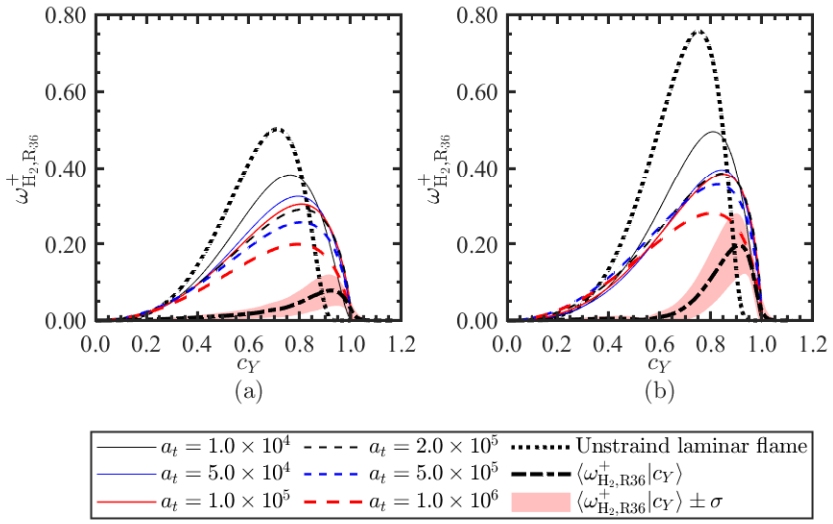


Figure 4.24: Comparison of conditionally averaged elemental reaction rate by R_{36} : $CH_2O+H \rightleftharpoons HCO+H_2$ with unstrained and strained laminar flames for H_2-50% (a) and H_2-20% (b).

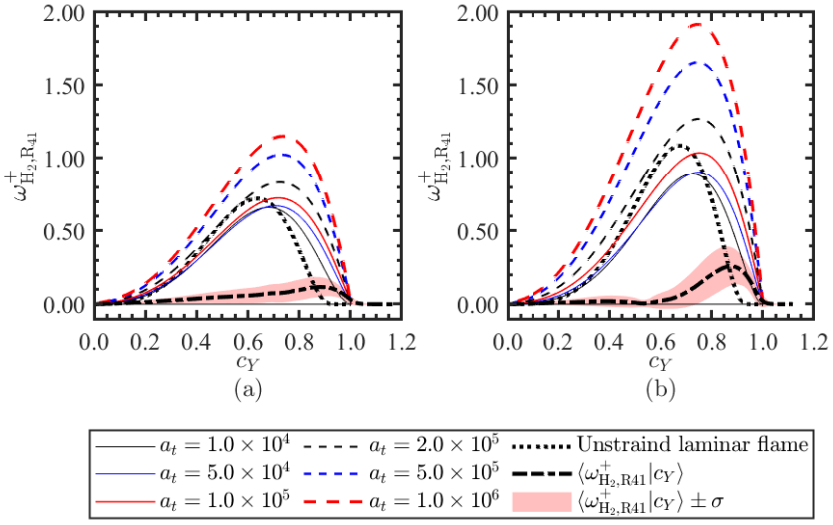


Figure 4.25: Comparison of conditionally averaged elemental reaction rate by R_{41} : $CH_4 + H \rightleftharpoons H_2 + CH_3$ with unstrained and strained laminar flames for H_2-50% (a) and H_2-20% (b).

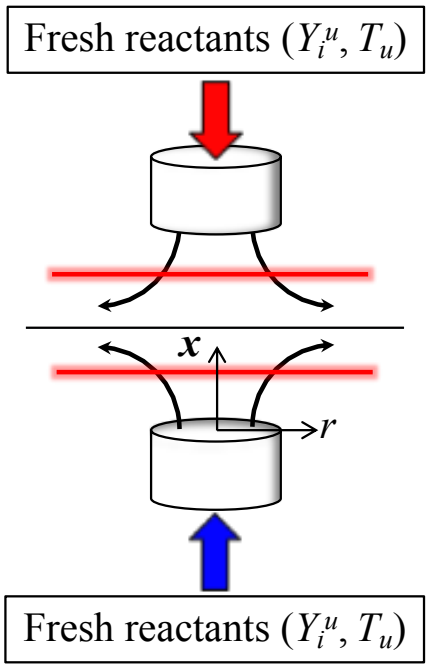


Figure 4.26: Schematic of counterflow twin flame configuration.

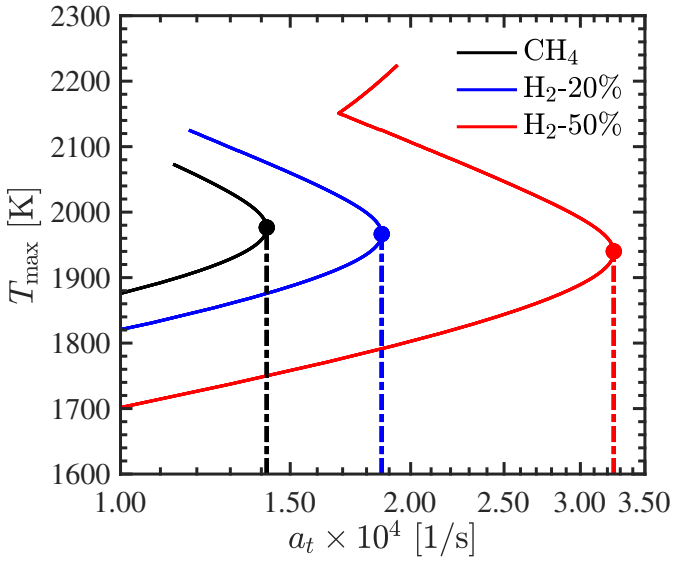


Figure 4.27: Response curves of T_{max} to a_t for mixture conditions of CH_4, CH_4:H_2 = 50:50 and CH_4:H_2 = 80:20.

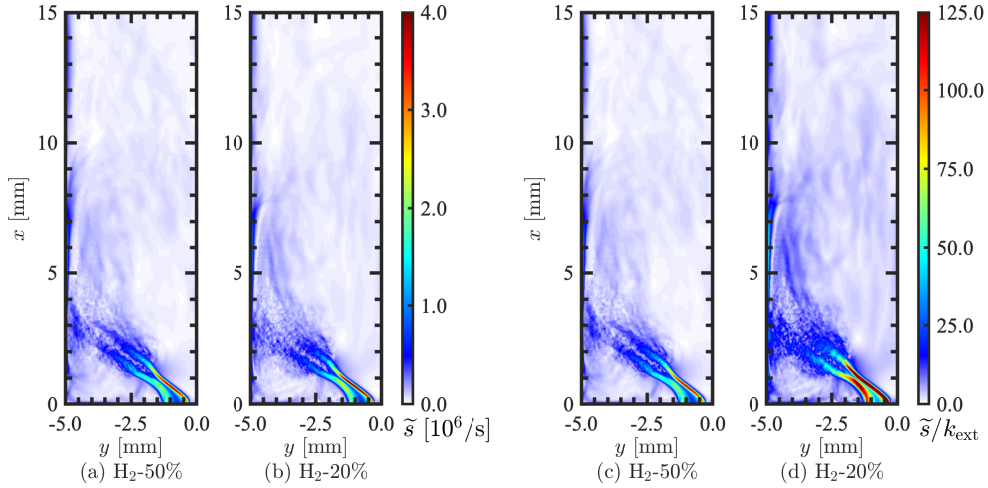


Figure 4.28: 2-dimensional distributions of strain rate $\widetilde{s} = \widetilde{S_{ij}}\widetilde{S_{ij}}$ (a,b) and strain rate normalized by extinction strain rate k_{ext} $\widetilde{s}/k_{\mathrm{ext}}$ (c,d) on the representative $x-y$ plane ($y \leq 0$, $z = 0$).

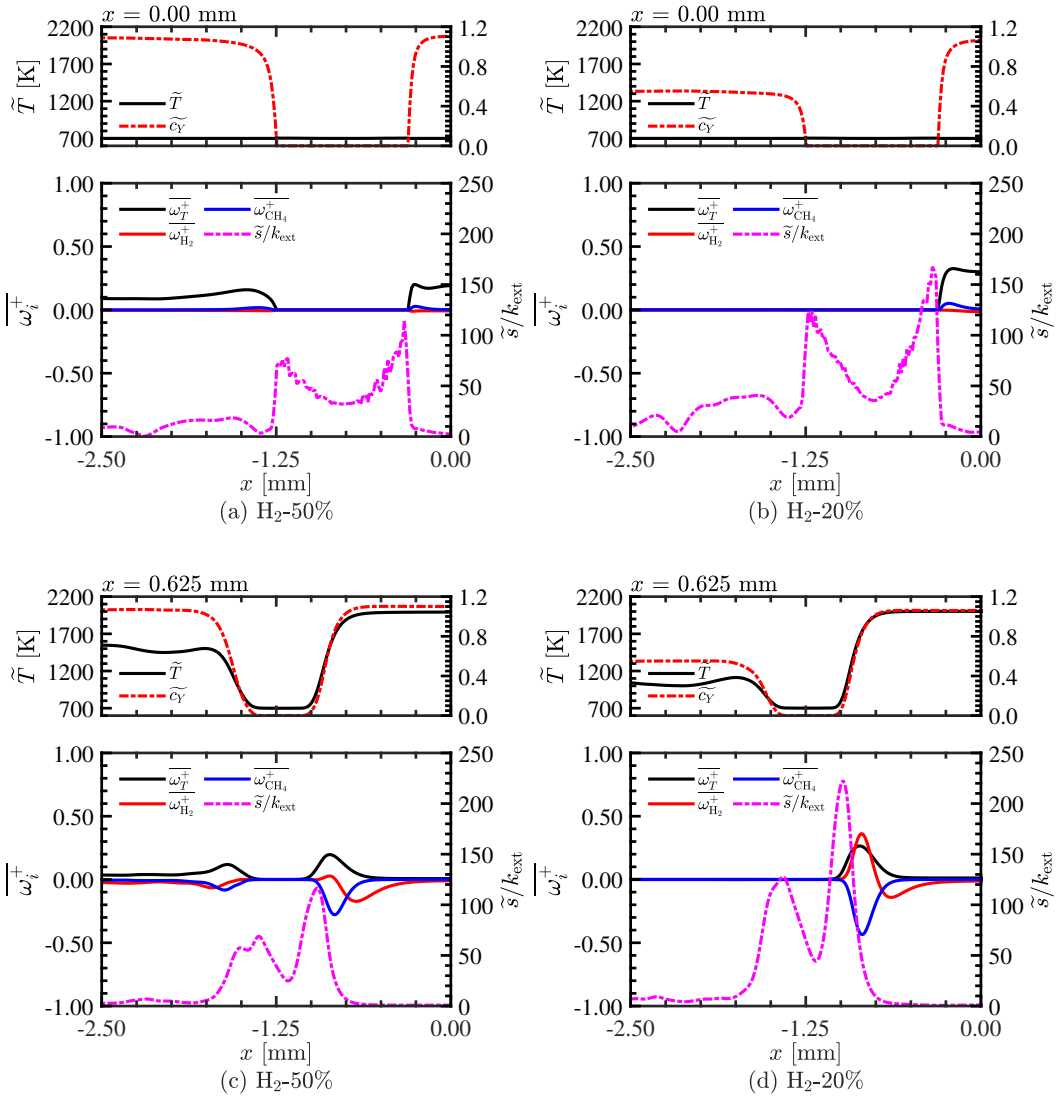


Figure 4.29: 1-dimensional distributions of $\widetilde{T}$ and $\widetilde{c_Y}$ (upper) and $\overline{\omega_T^+}$, $\overline{\omega_{\mathrm{H_2}}^+}$, $\overline{\omega_{\mathrm{CH_4}}^+}$ and $\widetilde{s}/k_{\mathrm{ext}}$ (lower) near the inflow boundary at x = 0.0 and 0.625 mm for H_2-50% (a,c) and H_2-20% (b,d).

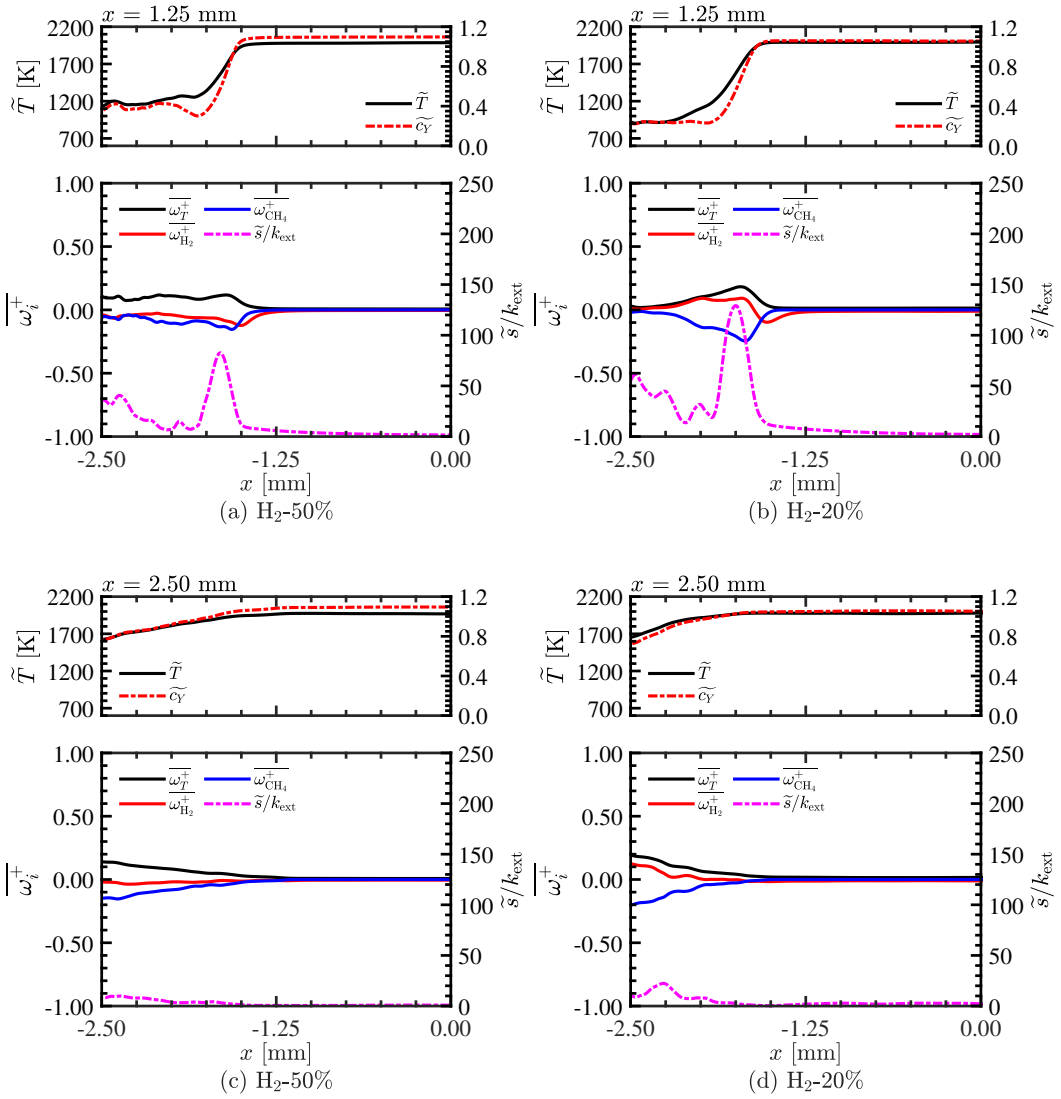


Figure 4.30: 1-dimensional distributions of $\widetilde{T}$ and $\widetilde{c_Y}$ (upper) and $\overline{\omega_T^+}$, $\overline{\omega_{H_2}^+}$, $\overline{\omega_{CH_4}^+}$ and $\widetilde{s}/k_{ext}$ (lower) near the inflow boundary at x = 1.25 and 2.50 mm for H_2-50% (a,c) and H_2-20% (b,d).

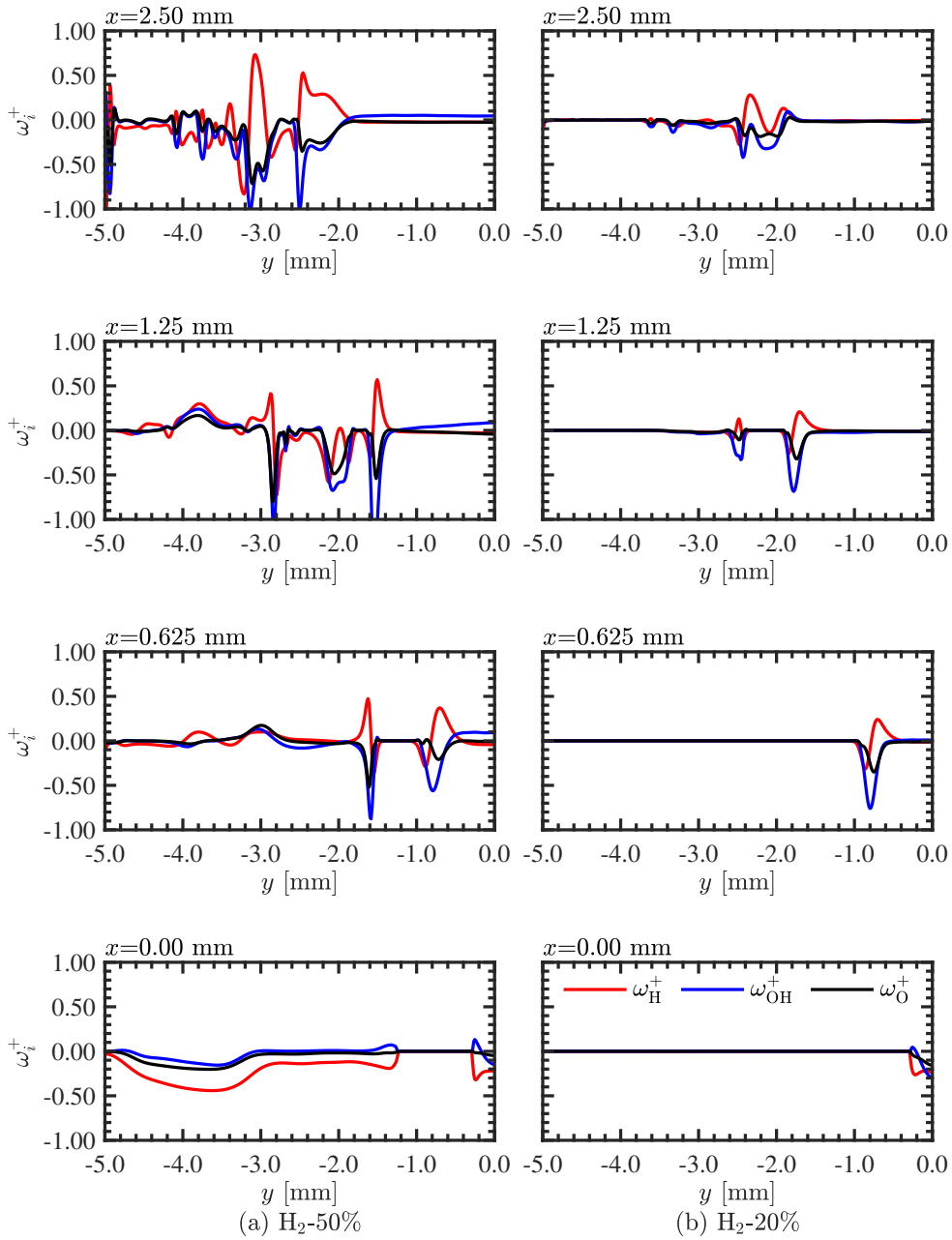


Figure 4.31: 1-dimensional distributions of radical species reaction rates, ω_H^+, ω_{OH}^+ and ω_O^+ at x = 0.0, 0.625, 1.25 and 2.50 mm for H_2-50% (a) and H_2-20% (b).

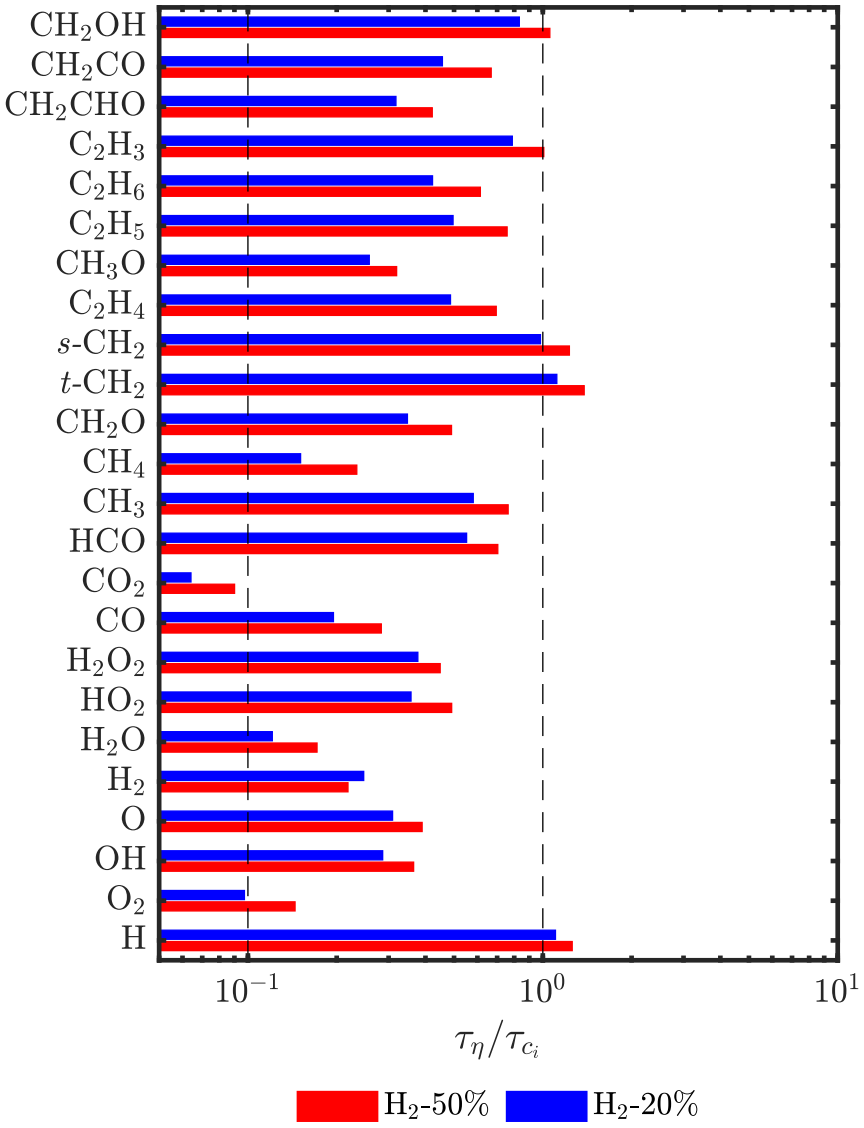


Figure 4.32: Ratios of turbulence time scale τ_η to chemical time scale τ_{c_i} ,τ_η/τ_{c_i}.

Chapter 5

Conclusions

In this thesis, effects of hydrogen enrichment on the global flame features and local flame structure and extinction mechanism of hydrogen-enriched CH_4/air turbulent swirling flames in a gas turbine model combustor are investigated by conducting direct numerical simulations. Conclusions in each chapter are summarized as follows.

In chapter 2, direct numerical simulations of hydrogen-enriched methane/air turbulent swirling premixed flames are conducted with reduced chemical mechanism. Two stoichiometric mixture conditions, of which volume ratio of CH_4:H_2 = 50:50 and 80:20 are considered. The following conclusions are obtained:

1. For both cases, total heat release rates in the combustor are lower than the calorific input E_{in} = 1.16 kW. The total heat release rates for the H_2-20% is lower than the values of H_2-50% even with almost the identical calorific input is provided.

2. The values reaction progress variable in the inner and outer recirculation zones are relatively similar for H_2-50%, whereas for H_2-20%, the values in the outer recirculation zones are lower compared with the values in the inner recirculation zones.

In chapter 3, effects of hydrogen ratios on the global flame features and reaction

zone characteristics of hydrogen-enriched CH_4/air turbulent swirling premixed flames are investigated. The investigation is conducted by visual examinations of global flame features, comparison of of DNS data with unstrained and strained laminar flames and balance between convection, diffusion and chemical reaction terms. The following conclusions are obtained.

1. For both cases, reaction rates are decreased compared to the corresponding laminar value. However, the global flame features and reaction zone characteristics between the cases are qualitatively different. For H_2-50%, the flame is stabilized in both shear layers, whereas for H_2-20%, extinction occurs in the outer shear layers and H_2 remain almost unreacted in the outer shear layer and recirculation zones.

2. Comparison of reaction zone characteristics in phase space showed deviation from the laminar profiles in H_2 mass fraction for H_2-20% case and all of the fuel species reaction rates. These suggest that considering the effect of local tangential strain rate is insufficient to clarify the reaction zone characteristics of the present DNS.

3. In the analysis of fuel species conservation equation, convection and diffusion of H_2 for H_2-20% are smaller than those of H_2-50% due to smaller H_2 mass fraction gradients resulted from the decreased consumption rates in the region from the outer shear layers to the downstream.

4. The qualitatively different global flame features and reaction zone characteristics between the cases are due to different role of H_2 in each mixture condition and differently decreased fuel species reaction rates in the outer shear layers.

In chapter 4, effects of turbulent motions on the local flame structures and extinction mechanisms in the shear layers are investigated. Statistical characteristics of local flames structures and elemental reaction rates mainly contribute to

production and consumption of the fuel species are clarified. Next, conditions for extinction and flame stabilization in the shear layers are considered in the aspects of thermochemical and flow strain rates. Finally, effects of turbulent motions on the species distributions are investigated. The following conclusions are obtained.

1. Fuel species reaction rates and heat release rates are substantially decreased in large portion of the defined flame surface. However, locally high heat release and fuel species reaction rates also exists on the defined flame surface.

2. Contributions by elemental reaction rates are decreased substantially in the ORZ due to lack of radical species and lower temperature for H_2-20%. In addition, the conditionally averaged contributions by elemental reactions deviated from the unstrained and strained laminar flames.

3. The flame in the ISL is stabilized by high temperature burnt gas recirculated by swirling flows even with extremely high strain rates. On the other hand, to clarify the extinction in the OSL for H_2-20%, not only strain rate of the flow field but also thermochemical conditions in the near filed of the extincted region should be considered.

4. The decreased reaction rates are also speculated to be due to local chemical time scales affected by turbulent motions.

References

[1] U.S. Energy Information Administration, International Energy Outlook 2019, 2019.

[2] B. Yenerdag, Y. Minamoto, K. Aoki, M. Shimura, Y. Nada, M. Tanahashi, Flame-wall interactions of lean premixed flames under elevated, rising pressure conditions, Fuel 189 (2017) 8–14.

[3] N. Saito, Y. Minamoto, B. Yenerdag, M. Shimura, M. Tanahashi, Effects of Turbulence on Ignition of Methane–Air and n-Heptane–Air Fully Premixed Mixtures, Combustion Science and Technology 190 (2018) 451–469.

[4] C. S. Yoo, T. Lu, J. H. Chen, C. K. Law, Direct numerical simulations of ignition of a lean n-heptane/air mixture with temperature inhomogeneities at constant volume: Parametric study, Combustion and Flame 158 (2011) 1727 – 1741.

[5] M. B. Luong, G. H. Yu, T. Lu, S. H. Chung, C. S. Yoo, Direct numerical simulations of ignition of a lean n-heptane/air mixture with temperature and composition inhomogeneities relevant to HCCI and SCCI combustion, Combustion and Flame 162 (2015) 4566 – 4585.

[6] Y. Tanaka, M. Nose, M. Nakao, K. Saitoh, E. Ito, K. Tsukagoshi, Development of the Low NOx Combustion System with EGR for 1700 ℃ class Gas Turbine, Mitsubishi Heavy Industries Technical Review 50 (2013) 2 – 7.

[7] R. W. Schefer, Hydrogen enrichment for improved lean flame stability, International Journal of Hydrogen Energy 28 (2003) 1131–1141.

[8] K. Inoue, K. Miyamoto, S. Domen, I. Tamura, T. Kawakami, S. Tanimura, Development of Hydrogen and Natural Gas Co-firing Gas Turbine, Mitsubishi Heavy Industries Technical Review 55 (2018) 1 – 6.

[9] A. Cappelletti, F. Martelli, Investigation of a pure hydrogen fueled gas turbine burner, International Journal of Hydrogen Energy 42 (2017) 10513 – 10523.

[10] D. M. Wicksall, A. K. Agrawal, R. W. Schefer, J. O. Keller, The interaction of flame and flow field in a lean premixed swirl-stabilized combustor operated on H_2/CH_4/air, Proceedings of the Combustion Institute 30 II (2005) 2875–2883.

[11] M. Shimura, T. Ueda, G.-M. Choi, M. Tanahashi, T. Miyauchi, Simultaneous dual-plane CH PLIF, single-plane OH PLIF and dual-plane stereoscopic PIV measurements in methane-air turbulent premixed flames, Proceedings of the Combustion Institute 33 (2011) 775 – 782.

[12] A. Johchi, Y. Naka, M. Shimura, M. Tanahashi, T. Miyauchi, Investigation on rapid consumption of fine scale unburned mixture islands in turbulent flame via 10kHz simultaneous CH–OH PLIF and SPIV, Proceedings of the Combustion Institute 35 (2015) 3663 – 3671.

[13] J. Kariuki, A. Dowlut, R. Yuan, R. Balachandran, E. Mastorakos, Heat release imaging in turbulent premixed methane-air flames close to blow-off, Proceedings of the Combustion Institute 35 (2015) 1443–1450.

[14] T. M. Wabel, P. Zhang, X. Zhao, H. Wang, E. Hawkes, A. M. Steinberg, Assessment of chemical scalars for heat release rate measurement in highly turbulent premixed combustion including experimental factors, Combustion and Flame 194 (2018) 485–506.

[15] W. Zhang, J. Wang, W. Lin, S. Guo, M. Zhang, G. Li, J. Ye, Z. Huang, Measurements on flame structure of bluff body and swirl stabilized premixed flames close to blow-off, Experimental Thermal and Fluid Science 104 (2019) 15–25.

[16] Y. Morii, H. Terashima, M. Koshi, T. Shimizu, E. Shima, ERENA : A fast and robust Jacobian-free integration method for ordinary differential equations of chemical kinetics, Journal of Computational Physics 322 (2016) 547–558.

[17] X. Gou, W. Sun, Z. Chen, Y. Ju, A dynamic multi-timescale method for combustion modeling with detailed and reduced chemical kinetic mechanisms, Combustion and Flame 157 (2010) 1111–1121.

[18] W. Sun, X. Gou, H. A. El-Asrag, Z. Chen, Y. Ju, Multi-timescale and correlated dynamic adaptive chemistry modeling of ignition and flame propagation using a real jet fuel surrogate model, Combustion and Flame 162 (2015) 1530–1539.

[19] W. Sun, Y. Ju, A multi-timescale and correlated dynamic adaptive chemistry and transport (CO-DACT) method for computationally efficient modeling of jet fuel combustion with detailed chemistry and transport, Combustion and Flame 184 (2017) 297–311.

[20] M. Tanahashi, M. Fujimura, T. Miyauchi, Coherent fine scale eddies in turbulent premixed flames, Proceedings of Combustion Institute 28 (2000) 529–535.

[21] Y. Shim, S. Tanaka, M. Tanahashi, T. Miyauchi, Local structure and fractal characteristics of H2-air turbulent premixed flame, Proceedings of the Combustion Institute 33 (2011) 1455–1462.

[22] Y. Minamoto, N. Fukushima, M. Tanahashi, T. Miyauchi, T. D. Dunstan,

N. Swaminathan, Effect of flow-geometry on turbulence-scalar interaction in premixed flames, Physics of Fluids 23 (2011) 125107.

[23] M. Shimura, K. Yamawaki, N. Fukushima, Y. S. Shim, Y. Nada, M. Tanahashi, T. Miyauchi, Flame and eddy structures in hydrogen-air turbulent jet premixed flame, Journal of Turbulence 13 (2012) N42.

[24] S. Tanaka, M. Shimura, N. Fukushima, M. Tanahashi, T. Miyauchi, DNS of turbulent swirling premixed flame in a micro gas turbine combustor, Proceedings of the Combustion Institute 33 (2011) 3293–3300.

[25] B. Yenerdag, N. Fukushima, M. Shimura, M. Tanahashi, T. Miyauchi, Turbulence-flame interaction and fractal characteristics of H_2-air premixed flame under pressure rising condition, Proceedings of the Combustion Institute 35 (2015) 1277–1285.

[26] D. H. France, Combustion characteristics of hydrogen, International Journal of Hydrogen Energy 5 (1980) 369–374.

[27] E. R. Hawkes, J. H. Chen, Direct numerical simulation of hydrogen-enriched lean premixed methane-air flames, Combustion and Flame 138 (2004) 242–258.

[28] F. H. V. Coppens, J. De Ruyck, A. A. Konnov, The effects of composition on burning velocity and nitric oxide formation in laminar premixed flames of $CH_4 + H_2 + O_2 + N_2$, Combustion and Flame 149 (2007) 409–417.

[29] P. Griebel, E. Boschek, P. Jansohn, Lean blowout limits and NO_x emissions of turbulent, lean premixed, hydrogen-enriched methane/air flames at high pressure, Journal of Engineering for Gas Turbines and Power 129 (2007) 404–410.

[30] R. Schefer, D. Wicksall, A. Agrawal, Combustion of hydrogen-enriched

methane in a lean premixed swirl-stabilized burner, Proceedings of the Combustion Institute 29 (2002) 843–851.

[31] P. Strakey, T. Sidwell, J. Ontko, Investigation of the effects of hydrogen addition on lean extinction in a swirl stabilized combustor, Proceedings of the Combustion Institute 31 II (2007) 3173–3180.

[32] P. Sayad, A. Schönborn, J. Klingmann, Experimental investigation of the stability limits of premixed syngas-air flames at two moderate swirl numbers, Combustion and Flame 164 (2016) 270–282.

[33] N. Syred, M. Abdulsada, A. Griffiths, T. O'Doherty, P. Bowen, The effect of hydrogen containing fuel blends upon flashback in swirl burners, Applied Energy 89 (2012) 106–110.

[34] T. F. Guiberti, D. Durox, L. Zimmer, T. Schuller, Analysis of topology transitions of swirl flames interacting with the combustor side wall, Combustion and Flame 162 (2014) 4342–4357.

[35] Z. Mansouri, M. Aouissi, T. Boushaki, Numerical computations of premixed propane flame in a swirl-stabilized burner: Effects of hydrogen enrichment, swirl number and equivalence ratio on flame characteristics, International Journal of Hydrogen Energy 41 (2016) 9664–9678.

[36] G. S. Jackson, R. Sai, J. M. Plaia, C. M. Boggs, K. T. Kiger, Influence of H_2 on the response of lean premixed CH_4 flames to high strained flows, Combustion and Flame 132 (2003) 503–511.

[37] S. J. Shanbhogue, Y. S. Sanusi, S. Taamallah, M. A. Habib, E. M. A. Mokheimer, A. F. Ghoniem, Flame macrostructures, combustion instability and extinction strain scaling in swirl-stabilized premixed CH_4/H_2 combustion, Combustion and Flame 163 (2016) 494–507.

[38] G. Karim, I. Wierzba, Y. Al-Alousi, Methane-hydrogen mixtures as fuels, International Journal of Hydrogen Energy 21 (1996) 625 – 631.

[39] S. Taamallah, K. Vogiatzaki, F. M. Alzahrani, E. M. Mokheimer, M. A. Habib, A. F. Ghoniem, Fuel flexibility, stability and emissions in premixed hydrogen-rich gas turbine combustion: Technology, fundamentals, and numerical simulations, Applied Energy 154 (2015) 1020–1047.

[40] T. Lieuwen, V. McDonell, E. Petersen, D. Santavicca, Fuel flexibility influences on premixed combustor blowout, flashback, autoignition, and stability, Journal of Engineering for Gas Turbines and Power 130 (2008) 011506.

[41] J. Wang, Z. Huang, C. Tang, H. Miao, X. Wang, Numerical study of the effect of hydrogen addition on methane-air mixtures combustion, International Journal of Hydrogen Energy 34 (2009) 1084–1096.

[42] M. S. Day, X. Gao, J. B. Bell, Properties of lean turbulent methane-air flames with significant hydrogen addition, Proceedings of the Combustion Institute 33 (2011) 1601–1608.

[43] R. K. Cheng, D. Littlejohn, P. A. Strakey, T. Sidwell, Laboratory investigations of a low-swirl injector with H_2 and CH_4 at gas turbine conditions, Proceedings of the Combustion Institute 32 II (2009) 3001–3009.

[44] H. S. Kim, V. K. Arghode, M. B. Linck, A. K. Gupta, Hydrogen addition effects in a confined swirl-stabilized methane-air flame, International Journal of Hydrogen Energy 34 (2009) 1054–1062.

[45] H. S. Kim, V. K. Arghode, A. K. Gupta, Flame characteristics of hydrogen-enriched methane-air premixed swirling flames, International Journal of Hydrogen Energy 34 (2009) 1063–1073.

[46] T. F. Guiberti, D. Durox, P. Scouflaire, T. Schuller, Impact of heat loss and hydrogen enrichment on the shape of confined swirling flames, Proceedings of the Combustion Institute 35 (2015) 1385–1392.

[47] J. R. Dawson, R. L. Gordon, J. Kariuki, E. Mastorakos, A. R. Masri, M. Juddoo, Visualization of blow-off events in bluff-body stabilized turbulent premixed flames, Proceedings of the Combustion Institute 33 (2011) 1559–1566.

[48] Y. Huang, V. Yang, Bifurcation of flame structure in a lean-premixed swirl-stabilized combustor: Transition from stable to unstable flame, Combustion and Flame 136 (2004) 383–389.

[49] Y. Huang, V. Yang, Effect of swirl on combustion dynamics in a lean-premixed swirl-stabilized combustor, Proceedings of the Combustion Institute 30 II (2005) 1775–1782.

[50] R. Mercier, T. F. Guiberti, A. Chatelier, D. Durox, O. Gicquel, N. Darabiha, T. Schuller, B. Fiorina, Experimental and numerical investigation of the influence of thermal boundary conditions on premixed swirling flame stabilization, Combustion and Flame 171 (2016) 42–58.

[51] N. W. Chakroun, S. J. Shanbhogue, Y. Dagan, A. F. Ghoniem, Flamelet structure in turbulent premixed swirling oxy-combustion of methane, Proceedings of the Combustion Institute 37 (2019) 4579–4586.

[52] N. Peters, Turbulent combustion, Cambridge University Press, Cambridge, U.K., 2000.

[53] A. J. Aspden, M. S. Day, J. B. Bell, Three-dimensional direct numerical simulation of turbulent lean premixed methane combustion with detailed kinetics, Combustion and Flame 166 (2016) 266–283.

[54] H. Carlsson, R. Yu, X. S. Bai, Flame structure analysis for categorization of lean premixed CH_4/air and H_2/air flames at high Karlovitz numbers: Direct numerical simulation studies, Proceedings of the Combustion Institute 35 (2015) 1425–1432.

[55] A. J. Aspden, M. S. Day, J. B. Bell, Lewis number effects in distributed flames, Proceedings of the Combustion Institute 33 (2011) 1473–1480.

[56] S. Lapointe, B. Savard, G. Blanquart, Differential diffusion effects, distributed burning, and local extinctions in high Karlovitz premixed flames, Combustion and Flame 162 (2015) 3341–3355.

[57] C. Xu, A. Y. Poludnenko, X. Zhao, H. Wang, T. Lu, Structure of strongly turbulent premixed n-dodecane–air flames: Direct numerical simulations and chemical explosive mode analysis, Combustion and Flame 209 (2019) 27–40.

[58] H. Wang, E. R. Hawkes, J. H. Chen, A direct numerical simulation study of flame structure and stabilization of an experimental high Ka CH4/air premixed jet flame, Combustion and Flame 180 (2017) 110–123.

[59] K. Aoki, M. Shimura, S. Ogawa, N. Fukushima, Y. Naka, Y. Nada, M. Tanahashi, T. Miyauchi, Short- and long-term dynamic modes of turbulent swirling premixed flame in a cuboid combustor, Proceedings of the Combustion Institute 35 (2015) 3209–3217.

[60] Y. Minamoto, K. Aoki, M. Tanahashi, N. Swaminathan, DNS of swirling hydrogen-air premixed flames, International Journal of Hydrogen Energy 40 (2015) 13604–13620.

[61] K. Aoki, M. Shimura, Y. Naka, M. Tanahashi, Disturbance energy budget of turbulent swirling premixed flame in a cuboid combustor, Proceedings of the Combustion Institute 36 (2017) 3809–3816.

[62] 店橋 護, DNS による反応性乱流の基礎的研究, 東京工業大学学位論文, 1996.

[63] R. J. Kee, G. Dixon-Lewis, J. Warnatz, M. E. Coltrin, J. A. Miller, A Fortran computer code package for the evaluation of gas-phase multicomponent transport properties, Report No. SAND86-8246, Sandia National Laboratories, 1986.

[64] R. J. Kee, F. M. Rupley, J. A. Miller, Chemkin-II: A Fortran chemical kinetics package for the analysis of gas phase chemical kinetics, Report No. SAND89-8009B, Sandia National Laboratories, 1989.

[65] S. K. Lele, Compact finite difference schemes with spectral-like resolution, Journal of Computational Physics 103 (1992) 16–42.

[66] K. W. Thompson, Time dependent boundary conditions for hyperbolic systems, Journal of Computational Physics 68 (1987) 1–24.

[67] T. J. Poinsot, S. K. Lele, Boundary conditions for direct simulations of compressible viscous flows, Journal of Computational Physics 101 (1992) 104–129.

[68] M. Baum, T. Poinsot, D. Thévenin, Accurate boundary conditions for multicomponent reactive flows, Journal of Computational Physics 116 (1994) 247–261.

[69] J. H. Williamson, Low-storage Runge-Kutta schemes, Journal of Computational Physics 35 (1980) 48–56.

[70] W. Sun, Z. Chen, X. Gou, Y. Ju, A path flux analysis method for the reduction of detailed chemical kinetic mechanisms, Combustion and Flame 157 (2010) 1298–1307.

[71] Y. Wang, M. Tanahashi, T. Miyauchi, Coherent fine scale eddies in turbulence transition of spatially-developing mixing layer, International Journal of Heat and Fluid Flow 28 (2007) 1280–1290.

[72] K. Aoki, M. Shimura, S. Ogawa, N. Fukushima, Y. Naka, Y. Nada, M. Tanahashi, T. Miyauchi, Short- and long-term dynamic modes of turbulent swirling premixed flame in a cuboid combustor, Proceedings of the Combustion Institute 35 (2015) 3209–3217.

[73] M. V. Petrova, F. A. Williams, A small detailed chemical-kinetic mechanism for hydrocarbon combustion, Combustion and Flame 144 (2006) 526–544.

[74] R. J. Kee, J. F. Grcar, M. Smooke, J. A.Miller, PREMIX: A Fortran program for modeling steady one-dimensional flames, Report No. SAND85-8240, Sandia National Laboratories, 1985.

[75] A. E. Lutz, R. J. Kee, J. Grcar, F. M. Rupley, OPPDIF: A Fortran program for computing opposed-flow diffusion flames, Report No. SAND96-8243, Sandia National Laboratories, 1997.

[76] A. Lutz, R. Kee, J. Miller, SENKIN: A Fortran program for predicting homogeneous gas phase chemical kinetics with sensitivity analysis, Report No. SAND87-8248, Sandia National Laboratories, 1987.

[77] M. Ihme, H. Pitsch, Prediction of extinction and reignition in nonpremixed turbulent flames using a flamelet/progress variable model. 1. A priori study and presumed PDF closure, Combustion and Flame 155 (2008) 70–89.

[78] M. Ihme, H. Pitsch, Prediction of extinction and reignition in nonpremixed turbulent flames using a flamelet/progress variable model. 2. Application in LES of Sandia flames D and E, Combustion and Flame 155 (2008) 90–107.

[79] S. Taamallah, S. J. Shanbhogue, A. F. Ghoniem, Turbulent flame stabilization modes in premixed swirl combustion: Physical mechanism and

Karlovitz number-based criterion, Combustion and Flame 166 (2016) 19–33.

[80] H. Wang, K. Luo, S. Lu, J. Fan, Direct numerical simulation and analysis of a hydrogen/air swirling premixed flame in a micro combustor, International Journal of Hydrogen Energy 36 (2011) 13838–13849.

[81] N. Darabiha, S. Candel, F. Marble, The effect of strain rate on a premixed laminar flame, Combustion and Flame 64 (1986) 203–217.

[82] E. R. Hawkes, J. H. Chen, Comparison of direct numerical simulation of lean premixed methane-air flames with strained laminar flame calculations, Combustion and Flame 144 (2006) 112–125.

[83] H. Wang, E. R. Hawkes, B. Savard, J. H. Chen, Direct numerical simulation of a high Ka CH_4/air stratified premixed jet flame, Combustion and Flame 193 (2018) 229–245.

[84] A. J. Aspden, M. S. Day, J. B. Bell, Towards the distributed burning regime in turbulent premixed flames, Journal of Fluid Mechanics 871 (2019) 1–21.

[85] T. Nilsson, H. Carlsson, R. Yu, X. S. Bai, Structures of turbulent premixed flames in the high Karlovitz number regime – DNS analysis, Fuel 216 (2018) 627–638.

[86] H. Carlsson, R. Yu, X.-S. Bai, Direct numerical simulation of lean premixed CH_4/air and H_2/air flames at high Karlovitz numbers, International Journal of Hydrogen Energy 39 (2014) 20216–20232.

[87] S. J. Shanbhogue, S. Husain, T. Lieuwen, Lean blowoff of bluff body stabilized flames: Scaling and dynamics, Progress in Energy and Combustion Science 35 (2009) 98–120.

[88] J. P. Longwell, E. E. Frost, M. A. Weiss, Flame Stability in Bluff Body Recirculation Zones, Industrial & Engineering Chemistry 45 (1953) 1629–1633.

[89] S. Yamaguchi, N. Ohiwa, T. Hasegawa, Structure and blow-off mechanism of rod-stabilized premixed flame, Combustion and Flame 62 (1985) 31–41.

[90] M. Tanahashi, T. Miyauchi, T. Saito, M. Shimamura, Local Extinction and NO_x Formation in Methane-Air Turbulent Premixed Flames, Proceedings of 2nd Asia-Pacific Conference on Combustion (1999) 500 – 503.

[91] T. Saito, M. Tanahashi, T. Miyauchi, Effects of Turbulence Intensities and Fuel Species in Turbulent Premixed Flames, Journal of the Combustion Society of Japan 44 (2002) 243 – 252.

[92] C. K. Law, C. J. Sung, Structure, aerodynamics, and geometry of premixed flamelets, Progress in Energy and Combustion Science 26 (2000) 459–505.

[93] T. Poinsot, D. Veynante, S. Candel, Quenching processes and premixed turbulent combustion diagrams, Journal of Fluid Mechanics Digital Archive 228 (1991) 561.

[94] E. Mastorakos, A. M. K. P. Taylor, J. H. Whitelaw, Extinction of turbulent counterflow flames with reactants diluted by hot products, Combustion and Flame 102 (1995) 101–114.

[95] S. Chaudhuri, S. Kostka, M. W. Renfro, B. M. Cetegen, Blowoff dynamics of bluff body stabilized turbulent premixed flames, Combustion and Flame 157 (2010) 790–802.

[96] S. Chaudhuri, S. Kostka, S. G. Tuttle, M. W. Renfro, B. M. Cetegen, Blowoff mechanism of two dimensional bluff-body stabilized turbulent premixed flames in a prototypical combustor, Combustion and Flame 158 (2011) 1358–1371.

[97] H. Watanabe, S. J. Shanbhogue, S. Taamallah, N. W. Chakroun, A. F. Ghoniem, The structure of swirl-stabilized turbulent premixed CH_4/air and $CH_4/O_2/CO_2$ flames and mechanisms of intense burning of oxy-flames, Combustion and Flame 174 (2016) 111–119.

[98] F. N. Egolfopoulos, Dynamics and structure of unsteady, strained, laminar premixed flames, Symposium (International) on Combustion 25 (1994) 1365–1373.

[99] C. G. Fotache, T. G. Kreutz, C. K. Law, Ignition of hydrogen-enriched methane by heated air, Combustion and Flame 110 (1997) 429–440.

[100] T. G. Kreutz, C. K. Law, Ignition in nonpremixed counterflowing hydrogen versus heated air: Computational study with skeletal and reduced chemistry, Combustion and Flame 114 (1998) 436–456.

[101] D. C. Haworth, R. J. Blint, B. Cuenot, T. J. Poinsot, Numerical simulation of turbulent propane-air combustion with nonhomogeneous reactants, Combustion and Flame 121 (2000) 395–417.

Appendix A

Chemical mechanism

Table. A1: List of species considered in the present study reduced from detailed UCSD mechanism by using PFA method

#	Species	#	Species	#	Species	#	Species	#	Species
1	H	6	H_2O	11	HCO	16	*s*-CH_2	21	C_2H_3
2	O_2	7	HO_2	12	CH_3	17	C_2H_4	22	CH_2CHO
3	OH	8	H_2O_2	13	CH_4	18	CH_3O	23	CH_2CO
4	O	9	CO	14	CH_2O	19	C_2H_5	24	CH_2OH
5	H_2	10	CO_2	15	*t*-CH_2	20	C_2H_6	25	N_2

Table. A2: Elemental reactions considered in the present study reduced from detailed UCSD mechanism by using PFA method

No.	Reaction	A	β	E_a
R_1	H+O_2 ⇌ OH+O	3.52E+16	-0.7	17069.8
R_2	H_2+O ⇌ OH+H	5.06E+04	2.7	6290.6
R_3	H_2+OH ⇌ H_2O+H	1.17E+09	1.3	3635.3
R_4	H_2O+O ⇌ 2OH	7.00E+05	2.3	14548.3
R_5	2H+M ⇌ H_2+M	1.30E+18	-1.0	0.0
	H_2/2.5/ H_2O/12.0/ CO/1.9/ CO_2/3.8			
R_6	H+OH+M ⇌ H_2O+M	4.00E+22	-2.0	0.0
	H_2/2.5/ H_2O/12.0/ CO/1.9/ CO_2/3.8			
R_7	2O+M ⇌ O_2+M	6.17E+15	-0.5	0.0
	H_2/2.5/ H_2O/12.0/ CO/1.9/ CO_2/3.8			
R_8	H+O+M ⇌ OH+M	4.71E+18	-1.0	0.0

	Reaction	A	β	E
	H_2/2.5/ H_2O/12.0/ CO/1.9/ CO_2/3.8			
R_9	$H+O_2(+M) \rightleftharpoons HO_2(+M)$	4.65E+12	0.4	0.0
	H_2/ 2.5/ H_2O/16.0/ CO/1.2/ CO_2/2.4/ C_2H_6 /1.5			
	Low pressure limit: 5.75E+19 -1.40 0.00			
	TROE centering: 0.50 1.00E-30 1.00E+30			
R_{10}	$HO_2+H \rightleftharpoons 2OH$	7.08E+13	0.0	294.9
R_{11}	$HO_2+H \rightleftharpoons H_2+O_2$	1.66E+13	0.0	822.9
R_{12}	$HO_2+H \rightleftharpoons H_2O+O$	3.10E+13	0.0	1720.8
R_{13}	$HO_2+O \rightleftharpoons OH+O_2$	2.00E+13	0.0	0.0
R_{14}	$HO_2+OH \rightleftharpoons H_2O+O_2$	7.00E+12	0.0	-1094.7
	Declared duplicate reaction			
R_{15}	$HO_2+OH \rightleftharpoons H_2O+O_2$	4.50E+14	0.0	10929.7
	Declared duplicate reaction			
R_{16}	$2OH(+M) \rightleftharpoons H_2O_2(+M)$	9.55E+13	-0.3	0.0
	H_2/2.5 H_2O/6.0/ H_2O_2/6.0/ CO/1.5/ CO_2/2.0			
	Low pressure limit: 2.76E+25 -3.20 0.00			
	TROE centering: 0.57 1.00E+30 1.00E-30			
R_{17}	$2HO_2 \rightleftharpoons H_2O_2+O_2$	1.03E+14	0.0	11042.1
	Declared duplicate reaction			
R_{18}	$2HO_2 \rightleftharpoons H_2O_2+O_2$	1.94E+11	0.0	-1408.9
	Declared duplicate reaction			
R_{19}	$H_2O_2+H \rightleftharpoons HO_2+H_2$	2.30E+13	0.0	7950.1
R_{20}	$H_2O_2+H \rightleftharpoons H_2O+OH$	1.00E+13	0.0	3585.1
R_{21}	$H_2O_2+OH \rightleftharpoons H_2O+HO_2$	1.74E+12	0.0	1434.0
	Declared duplicate reaction			
R_{22}	$H_2O_2+OH \rightleftharpoons H_2O+HO_2$	7.59E+13	0.0	7272.9
	Declared duplicate reaction			
R_{23}	$H_2O_2+O \rightleftharpoons HO_2+OH$	9.63E+06	2.0	3991.4
R_{24}	$CO+O(+M) \rightleftharpoons CO_2(+M)$	1.80E+11	0.0	2384.1
	H_2/2.5/ H_2O/12.0/ CO/2.0/ CO_2/4.0			
	Low pressure limit: 1.5500E+24 -2.79 4191			
	TROE centering: 1.00 1.00 1.00E+07 1.00E+07			
R_{25}	$CO+OH \rightleftharpoons CO_2+H$	4.40E+06	1.5	-740.9
R_{26}	$CO+HO_2 \rightleftharpoons CO_2+OH$	2.00E+13	0.0	22944.5
R_{27}	$CO+O_2 \rightleftharpoons CO_2+O$	1.00E+12	0.0	47700.1
R_{28}	$HCO+M \rightleftharpoons CO+H+M$	1.86E+17	-1.0	17000.5
	H_2/1.9/ H_2O/12.0/ CO/2.5/ CO_2/2.5/			
R_{29}	$HCO+H \rightleftharpoons CO+H_2$	5.00E+13	0.0	0.0
R_{30}	$HCO+O \rightleftharpoons CO+OH$	3.00E+13	0.0	0.0
R_{31}	$HCO+O \rightleftharpoons CO_2+H$	3.00E+13	0.0	0.0

	Reaction	A	β	E
R_{32}	HCO+OH $\rightleftharpoons$ CO+H_2O	3.00E+13	0.0	0.0
R_{33}	HCO+O_2 $\rightleftharpoons$ CO+HO_2	7.58E+12	0.0	409.9
R_{34}	HCO+CH_3 $\rightleftharpoons$ CO+ CH_4	5.00E+13	0.0	0.0
R_{35}	H+HCO(+M) $\rightleftharpoons$ CH_2O(+M)	1.09E+12	0.5	-260.0
	H_2/2.0/ H_2O/6.0/ CO/1.5/ CO_2/2.0/ CH_4/2.0/ C_2H_6/3.0			
	Low pressure limit: 1.35E+24 -2.57 424.95			
	TROE centering: 0.78240 271.0 2755 6570			
R_{36}	CH_2O+H $\rightleftharpoons$ HCO+H_2	5.74E+07	1.9	2748.6
R_{37}	CH_2O+O $\rightleftharpoons$ HCO+OH	3.50E+13	0.0	3513.4
R_{38}	CH_2O+OH $\rightleftharpoons$ HCO+H_2O	3.90E+10	0.9	406.3
R_{39}	CH_2O+O_2 $\rightleftharpoons$ HCO+HO_2	6.00E+13	0.0	40674.0
R_{40}	CH_2O+HO_2 $\rightleftharpoons$ HCO+H_2O_2	4.11E+04	2.5	10210.3
R_{41}	CH_4 +H $\rightleftharpoons$ H_2+CH_3	1.30E+04	3.0	8037.8
R_{42}	CH_4 +OH $\rightleftharpoons$ H_2O+CH_3	1.60E+07	1.8	2782.0
R_{43}	CH_4 +O $\rightleftharpoons$ CH_3+OH	1.90E+09	1.4	8675.9
R_{44}	CH_4 +O_2 $\rightleftharpoons$ CH_3+HO_2	3.98E+13	0.0	56890.5
R_{45}	CH_4 +HO_2 $\rightleftharpoons$ CH_3+H_2O_2	9.03E+12	0.0	24641.5
R_{46}	CH_3+H $\rightleftharpoons$ *t*-CH_2+H_2	1.80E+14	0.0	15105.2
R_{47}	CH_3+H $\rightleftharpoons$ *s*-CH_2+H_2	1.55E+14	0.0	13479.9
R_{48}	CH_3+OH $\rightleftharpoons$ *s*-CH_2+H_2O	4.00E+13	0.0	2502.4
R_{49}	CH_3+O $\rightleftharpoons$ CH_2O+H	8.43E+13	0.0	0.0
R_{50}	CH_3+*t*-CH_2 $\rightleftharpoons$ C_2H_4+H	4.22E+13	0.0	0.0
R_{51}	CH_3+HO_2 $\rightleftharpoons$ CH_3O+OH	5.00E+12	0.0	0.0
R_{52}	CH_3+O_2 $\rightleftharpoons$ CH_2O+OH	3.30E+11	0.0	8941.2
R_{53}	CH_3+O_2 $\rightleftharpoons$ CH_3O+O	1.10E+13	0.0	27820.0
R_{54}	2CH_3 $\rightleftharpoons$ C_2H_4+H_2	1.00E+14	0.0	32002.9
R_{55}	2CH_3 $\rightleftharpoons$ C_2H_5+H	3.16E+13	0.0	14698.9
R_{56}	H+CH_3(+M) $\rightleftharpoons$ CH_4 (+M)	1.27E+16	-0.6	382.9
	H_2/2.0/ H_2O/16.0 CO/1.5/ CO_2/2.0/ CH_4/2.0			
	Low pressure limit: 2.4700E+33 -4.76 2440			
	TROE centering: 0.783 74.0 2941 6964			
R_{57}	2CH_3(+M) $\rightleftharpoons$ C_2H_6 (+M)	1.81E+13	0.0	0.0
	H_2/2.0/ H_2O/6.0 CO/1.5/ CO_2/2.0/ CH_4/2.0/ C_2H_6/3.0			
	Low pressure limit: 1.27E+41 -7.00 2762.90			
	TROE centering: 0.620 73.0 1200.			
R_{58}	*s*-CH_2+OH $\rightleftharpoons$ CH_2O+H	3.00E+13	0.0	0.0
R_{59}	*s*-CH_2+O_2 $\rightleftharpoons$ CO+OH+H	3.13E+13	0.0	0.0
R_{60}	*s*-CH_2+CO_2 $\rightleftharpoons$ CO+CH_2O	3.00E+12	0.0	0.0
R_{61}	*s*-CH_2+M $\rightleftharpoons$ *t*-CH_2+M	6.00E+12	0.0	0.0
	H_2/2.4/ H_2O/15.4/ CO/1.8/ CO_2/3.6			

	Reaction	A	β	E
R_{62}	t-CH_2+OH $\rightleftharpoons$ CH_2O+H	2.50E+13	0.0	0.0
R_{63}	t-CH_2+O $\rightleftharpoons$ CO+2H	8.00E+13	0.0	0.0
R_{64}	t-CH_2+O $\rightleftharpoons$ CO+H_2	4.00E+13	0.0	0.0
R_{65}	t-CH_2+O_2 $\rightleftharpoons$ CO_2+H_2	2.63E+12	0.0	1491.4
R_{66}	t-CH_2+O_2 $\rightleftharpoons$ CO+OH+H	6.58E+12	0.0	1491.4
R_{67}	CH_3O+H $\rightleftharpoons$ CH_2O+H_2	2.00E+13	0.0	0.0
R_{68}	CH_3O+H $\rightleftharpoons$ s-CH_2+H_2O	1.60E+13	0.0	0.0
R_{69}	CH_3O+OH $\rightleftharpoons$ CH_2O+H_2O	5.00E+12	0.0	0.0
R_{70}	CH_3O+O $\rightleftharpoons$ OH+CH_2O	1.00E+13	0.0	0.0
R_{71}	CH_3O+O_2 $\rightleftharpoons$ CH_2O+HO_2	4.28E-13	7.6	-3537.3
R_{72}	CH_3O+M $\rightleftharpoons$ CH_2O+H+M	7.78E+13	0.0	13513.4
	H_2/2.0/ H_2O/6.0/ CO/1.5/ CO_2/2.0/ CH_4/2.0			
R_{73}	C_2H_6 +H $\rightleftharpoons$ C_2H_5+H_2	5.40E+02	3.5	5210.3
R_{74}	C_2H_6 +O $\rightleftharpoons$ C_2H_5+OH	1.40E+00	4.3	2772.5
R_{75}	C_2H_6 +OH $\rightleftharpoons$ C_2H_5+H_2O	2.20E+07	1.9	1123.3
R_{76}	C_2H_6 +CH_3 $\rightleftharpoons$ C_2H_5+ CH_4	5.50E-01	4.0	8293.5
R_{77}	C_2H_6 (+M) $\rightleftharpoons$ C_2H_5+H(+M)	8.85E+20	-1.2	102222.8
	H_2/2.0/ H_2O/6.0 CO/1.5/ CO_2/2.0/ CH_4/2.0/ C_2H_6/3.0			
	Low pressure limit: 4.90E+42 -6.43 107170			
	TROE centering: 0.84 125 2219 6882			
R_{78}	C_2H_6 +HO_2 $\rightleftharpoons$ C_2H_5+H_2O_2	1.32E+13	0.0	20469.9
R_{79}	C_2H_5+H $\rightleftharpoons$ C_2H_4+H_2	3.00E+13	0.0	0.0
R_{80}	C_2H_5+O $\rightleftharpoons$ C_2H_4+OH	3.06E+13	0.0	0.0
R_{81}	C_2H_5+O $\rightleftharpoons$ CH_3+CH_2O	4.24E+13	0.0	0.0
R_{82}	C_2H_5+O_2 $\rightleftharpoons$ C_2H_4+HO_2	7.50E+14	-1.0	4799.9
R_{83}	C_2H_5(+M) $\rightleftharpoons$ C_2H_4+H(+M)	1.11E+10	1.0	36768.6
	H_2/2.0/ H_2O/6.0/ CO/1.5/ CO_2/2.0/ CH_4/2.0			
	Low pressure limit: 3.99E+33 -4.99 40000			
	TROE centering: 0.168 1200 1.00E-28			
R_{84}	C_2H_4+H $\rightleftharpoons$ C_2H_3+H_2	4.49E+07	2.1	13360.4
R_{85}	C_2H_4+OH $\rightleftharpoons$ C_2H_3+H_2O	5.53E+05	2.3	2963.7
R_{86}	C_2H_4+O $\rightleftharpoons$ CH_3+HCO	2.25E+06	2.1	0.0
R_{87}	C_2H_4+O $\rightleftharpoons$ CH_2CHO+H	1.21E+06	2.1	0.0
R_{88}	2C_2H_4 $\rightleftharpoons$ C_2H_3+C_2H_5	5.01E+14	0.0	64700.1
R_{89}	C_2H_4+O_2 $\rightleftharpoons$ C_2H_3+HO_2	4.22E+13	0.0	57623.1
R_{90}	C_2H_4+M $\rightleftharpoons$ C_2H_3+H+M	2.60E+17	0.0	96568.1
	H_2/2.0/ H_2O/6.0/ CO/1.5/ CO_2/2.0 CH_4/2.0			
R_{91}	C_2H_3+O_2 $\rightleftharpoons$ CH_2O+HCO	1.70E+29	-5.3	6503.1
R_{92}	C_2H_3+O_2 $\rightleftharpoons$ CH_2CHO+O	7.00E+14	-0.6	5262.4
R_{93}	CH_2CO+H $\rightleftharpoons$ CH_3+CO	1.50E+09	1.4	2688.8

	Reaction	A	β	E
R_{94}	$CH_2CO+O \rightleftharpoons t\text{-}CH_2+CO_2$	2.00E+13	0.0	2294.5
R_{95}	$CH_2CO+CH_3 \rightleftharpoons C_2H_5+CO$	9.00E+10	0.0	0.0
R_{96}	$CH_2OH+H \rightleftharpoons CH_2O+H_2$	3.00E+13	0.0	0.0
R_{97}	$CH_2OH+H \rightleftharpoons CH_3+OH$	2.50E+17	-0.9	5126.9
R_{98}	$CH_2OH+OH \rightleftharpoons CH_2O+H_2O$	2.40E+13	0.0	0.0
R_{99}	$CH_2OH+O_2 \rightleftharpoons CH_2O+HO_2$	5.00E+12	0.0	0.0
R_{100}	$CH_2OH+M \rightleftharpoons CH_2O+H+M$	5.00E+13	0.0	25119.5
	H_2/2.0/ H_2O/6.0/ CO/1.5/ CO_2/2.0/ CH_4/2.0			
R_{101}	$CH_3O+M \rightleftharpoons CH_2OH+M$	1.00E+14	0.0	19120.5
	H_2/2.0/ H_2O/6.0/ CO/1.5/ CO_2/2.0/ CH_4/2.0			
R_{102}	$CH_2CO+OH \rightleftharpoons CH_2OH+CO$	1.02E+13	0.0	0.0
R_{103}	$CH_2CHO \rightleftharpoons CH_2CO+H$	1.05E+37	-7.2	44340.3
R_{104}	$CH_2CHO+H \rightleftharpoons CH_3+HCO$	5.00E+13	0.0	0.0
R_{105}	$CH_2CHO+H \rightleftharpoons CH_2CO+H_2$	2.00E+13	0.0	0.0
R_{106}	$CH_2CHO+O \rightleftharpoons CH_2O+HCO$	1.00E+14	0.0	0.0
R_{107}	$CH_2CHO+OH \rightleftharpoons CH_2CO+H_2O$	3.00E+13	0.0	0.0
R_{108}	$CH_2CHO+O_2 \rightleftharpoons CH_2O+CO+OH$	3.00E+10	0.0	0.0
R_{109}	$CH_2CHO+CH_3 \rightleftharpoons C_2H_5+CO+H$	4.90E+14	-0.5	0.0
R_{110}	$CH_2CHO+HO_2 \rightleftharpoons CH_2O+HCO+OH$	7.00E+12	0.0	0.0
R_{111}	$CH_2CHO \rightleftharpoons CH_3+CO$	1.17E+43	-9.8	43799.9

A: Frequency factor, β: pre-exponential temperature exponent ,E_a: Activation energy [cal/mol])

M denotes the third body and (+M) denotes fall-off reaction

Foll off reaction in the Troe from: $F_{\text{cent}} = (1-\alpha)\exp(-T/T^{***}) + \alpha\exp(-T/T^{*}) + \exp(-T^{**}/T)$

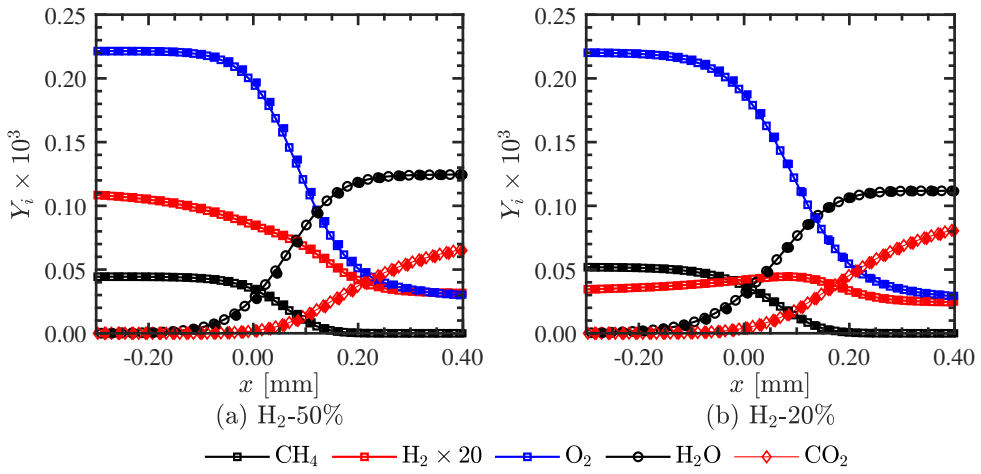


Fig. A1: One-dimensional unstrained laminar premixed flame profiles of major species in the reaction zone obtained by using detailed chemistry (open symbols) and reduced chemistry by using PFA method (filled symbols) for H_2-50% (a) and H_2-20% (b).

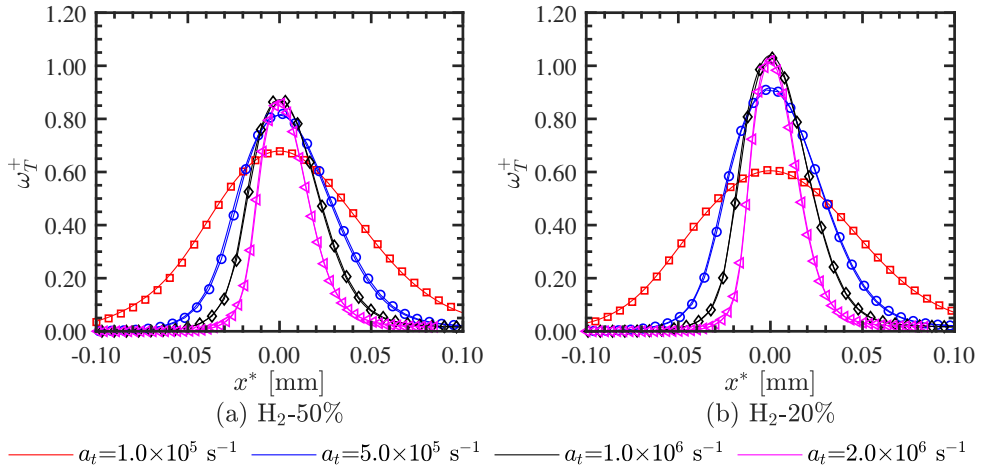


Fig. A2: Responses of heat release rate profiles in strained laminar flames (reactants to products configuration) at several tangential strain rates obtained by using detailed chemistry (lines) and reduced chemistry by using PFA method (open symbols) for H_2-50% (a) and H_2-20% (b).

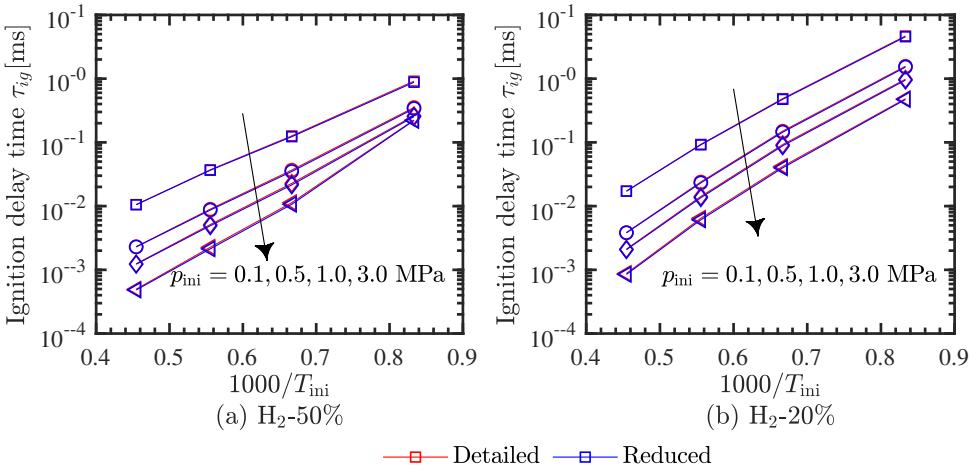


Fig. A3: Comparison of ignition delay time between detailed chemistry (red open squares) and reduced chemistry by using PFA method (blue open squares) for H_2-50% (a) and H_2-20% (b).

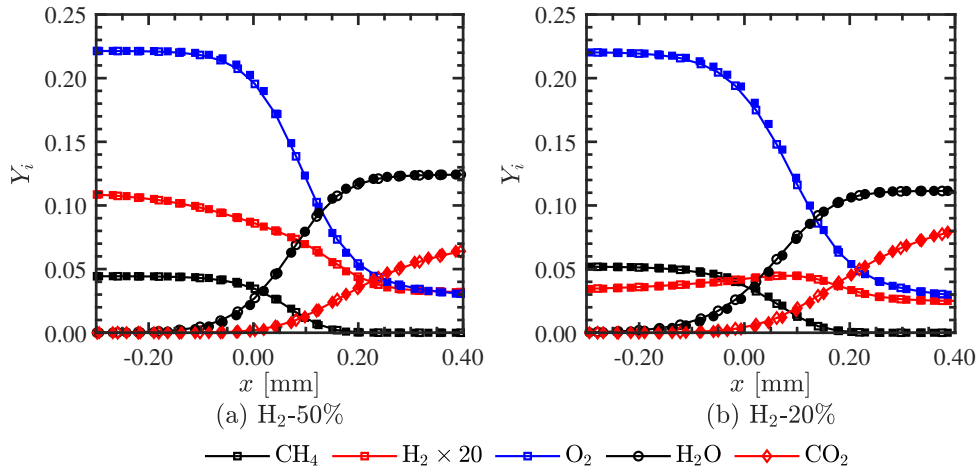


Fig. A4: Profiles of major species in one-dimensional laminar premixed flame calculated by PREMIX (open symbols) and MTS and CO-DACT (filled symbols) for H_2-50% (a) and H_2-20% (b).

Acknowledgements

First and foremost, I would like to express my deepest gratitude to my academic supervisor Professor Tanahashi for his continuous support and guidance throughout my time as his student. I also would like to thank Associate Professor Shimura and Assistant Professor Minamoto for their constant encouragement and invaluable guidance.

To my colleagues and friends in Reactive Gas Dynamics Laboratory including the past members; Yenerdag, Hiraoka, Aoki, Osawa, Kiran, Kishita, Yoshida, Saito, Kihara, Komatsu, Yabuta, Yamada, Maeda, Son, Kumar, Sujoy, Mohamed, Kondo, Tanaka, Kouya, Moronuki, Narukawa, Ando, Ito, Hirasawa, Fuse, Igarashi, Konagamitsu, Kanzaki, Hayakawa, Kawabata, Atagi, Sasaki, Nakagama, Nakazawa, Hisakado, Yokoyama, Nakagome, Sakai, Jigjid, Lu, Hattori, Tamai.

My acknowledgement would be incomplete without thanking the biggest source of my strength, my family in Korea. I deeply thank them for their support, encouragement and endless patience to follow my dream.